Study on Preparation and Characterization of Bismuth Substituted Gadolinium Iron Garnet Thin Films by Metal Organic Decomposition Method

東京農工大学大学院 工学府
電子情報工学専攻
Abdul Wahid Danish

DOCTORAL DISSERTATION

Study on Preparation and Characterization of Bismuth Substituted Gadolinium Iron Garnet Thin Films by Metal Organic Decomposition Method

A DISSERTATION SUBMITTED IN PARTIAL FULFILLMENT OF THE REQUIREMENTS FOR THE DEGREE OF DOCTOR OF ENGINEERING

17th January, 2017

Presented by Abdul Wahid Danish (Student ID 14834207)

Directed by Associate Professor Hiromasa SHIMIZU

Department of Electronic and Information Engineering,

Graduate School of Engineering,

Tokyo University of Agriculture and Technology

Acknowledgements

ABSTRACT

Bismuth substituted gadolinium iron garnet ($Bi_xGd_{3-x}Fe_5O_{12}$; Bi:GdIG) is a ferrimagnetic material, which is one of the most desirable materials for magneto optical devices. This thesis is devoted to preparation and characterization of Bi:GdIG thin films towards application to magneto optical devices. Purpose of my research and related researches are described in chapter 1. Fundamental physics and characterization method are described in chapter 2 and 3. I focused on the metal organic decomposition (MOD) method to prepare the Bi:GdIG film because of simple fabrication process.

The magnetic anisotropy and Faraday rotation (FR) of Bi:GdIG are influenced by the fabrication condition. I fabricated Bi:GdIG thin films on GGG, SGGG and glass substrates by MOD method and enhanced metal organic decomposition (EMOD) method in order to investigate the perpendicular magnetic anisotropy and to obtain large FR by changing the fabrication conditions. I characterized the samples by X-ray diffraction, FR, optical transmittance/reflectance and magnetization. The relationship among the magneto optical properties, crystalline quality, thickness, annealing temperature/gas, and Bi substitution (x) are discussed.

The $Bi_1Gd_2Fe_5O_{12}$ thin films were fabricated on GGG substrates by MOD method, in order to investigate the magnetic anisotropy and FR by fabrication conditions. We showed that Bi:GdIG thin films with FR (13.7 deg./μm at λ = 510 nm) and high crystalline quality were successfully fabricated, and larger perpendicular magnetic anisotropy is obtained for the samples annealed at 620 – 700°C without O_2 and for the samples annealed at 750 ~ 800°C with and without O_2. I found that the magnetic anisotropy influenced by the annealing gas during the annealing process and summarized in chapter 4.

However GGG and SGGG single crystal substrates are more expensive than glass substrates. I prepared $Bi_xGd_{3-x}Fe_5O_{12}$ thin film on glass substrate by EMOD method in order

to investigate the influence of annealing temperature and amount of Bi substitution on FR. I used the $Gd_3Fe_5O_{12}$ buffer layer instead of direct fabrication of $Bi_xGd_{3-x}Fe_5O_{12}$ thin film on glass substrate to increase the FR. When $Bi_{2.5}Gd_{0.5}Fe_5O_{12}$ thin film was prepared with annealing temperature of 620°C with the $Gd_3Fe_5O_{12}$ buffer layer on glass substrates, the films showed larger FR (27.9 deg./μm at λ = 533 nm), which is 85% of single crystal $Bi_{2.5}Gd_{0.5}Fe_5O_{12}$ on SGGG substrate. I found that larger FR can be obtained by using $Gd_3Fe_5O_{12}$ buffer layer. However with increasing the Bi content the surface of the samples became slightly hazy. These results are summarized in chapter 5.

In order to determine the optimum fabrication condition for the $Gd_3F_5O_{12}$ buffer layer, I fabricated the $Gd_3Fe_5O_{12}$ layers whose thicknesses were changed by spin-coating times under various annealing temperatures with MOD solution. I fabricated 115 nm-thick $Bi_2Gd_1Fe_5O_{12}$ thin films with fixed annealing temperature of 620° C on the $Gd_3Fe_5O_{12}$ buffer layers. The $Bi_2Gd_1Fe_5O_{12}$ thin films with 286 nm-thick $Gd_3Fe_5O_{12}$ buffer layer annealed at 750° C

showed maximum FR of 36.3 deg./μm at the wavelength λ = 500 nm, which is 23 times larger than sample without the $Gd_3Fe_5O_{12}$ buffer layer, and as high as 90.1 % of the single crystalline $Bi_2Gd_1Fe_5O_{12}$ thin film on an SGGG substrate (40.3 deg./μm). I found the influence of the $Gd_3Fe_5O_{12}$ buffer layer thickness and annealing temperature on FR of the $Bi_xGd_{3-x}Fe_5O_{12}$ main layer and summarized in chapter 6.

These results are promising for application to optical waveguide devices such as optical isolators and circulators, and MOSLMs on glass substrates. I summarized as a conclusion in chapter 7.

CONTENTS

CHAPTER 1

Introduction

1.1 Background

Spatial light Modulator (SLM) are devices that are used to modulate amplitude, phase or polarization of light waves in space and time. SLMs are key components in image projection system such as displays and projectors. They convert electrical signal to optical images. Several types of SLMs with pixel arrays, such as a liquid crystal SLM, liquid crystal on silicon (LCOS-SLM) and ferroelectric liquid crystal on silicon, have been developed. Recently, SLMs are becoming increasingly important as a light modulator in holographic data storage which requires high speed SLMs for ensuring the high data transfer rate [1]. Magneto-Optic SLMs (MOSLMs) are highly expected, because MOSLMs have fast pixel switching speed, high rate of data transfer and non-volatile property. The MOSLM provides magnetic visual images based on Faraday rotation and magnetization reversal, own the non-volatile property so that the system requires no power consumption for still images. The single crystal garnets with perpendicular magnetic anisotropy and two polarizers have been used as pixel elements to switch the optical output of MOSLM, depending on the up and down magnetization of the magnetic garnet, as schematically shown in Fig. 1.1.
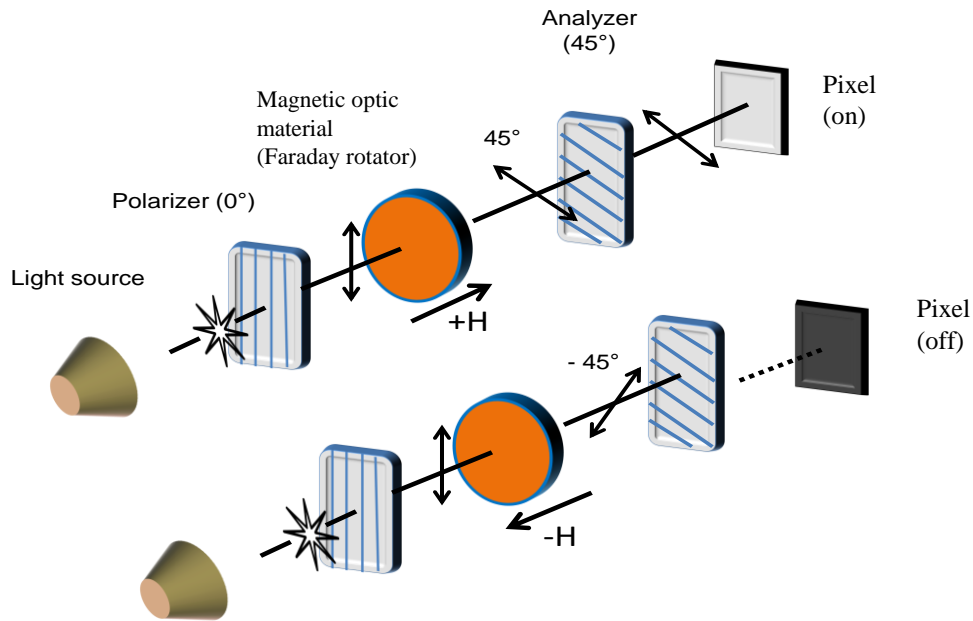
Fig. 1.1 Schematic image for basic principle of MOSLMs providing magnetic visual images based on Faraday rotation & magnetization reversal

Under the configuration of Fig. 1.1 the contrast of the image can be expressed as follow.

Contrast = I_+/I_-

Where I_+ and I_- is the intensity of transmitted light through magnetic material under ±applied magnetic field (H) and can be expressed by the following equation.

$$I_+ = \frac{1 + sin(2\theta_f)}{2}$$
$$I_- = \frac{1 - sin(2\theta_f)}{2}$$

If $\theta_f = 45°$, then the contrast is infinite. Fig. 1.2 shows the transmittance intensities dependent to Faraday rotation θ_f under ± magnetic field.
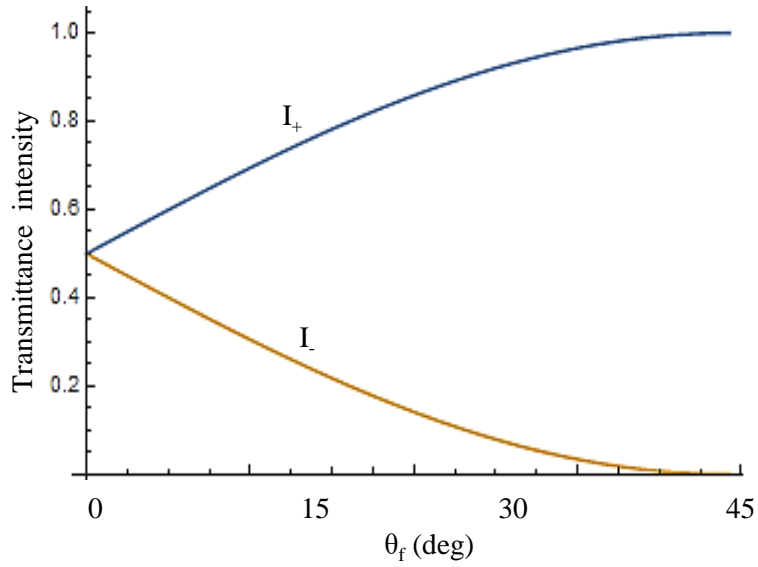
Fig. 1.2 Optical transmittance intensities as function of Faraday rotation through a magnetic material under applied magnetic field (±H).

Fig. 1.3 shows the transmittance intensity through commercial Faraday rotator for optical isolators at a wavelength λ = 1550 nm angle with fixed analyzer angle under ± magnetic field. The angle of the polarizer was changed manually by hand.
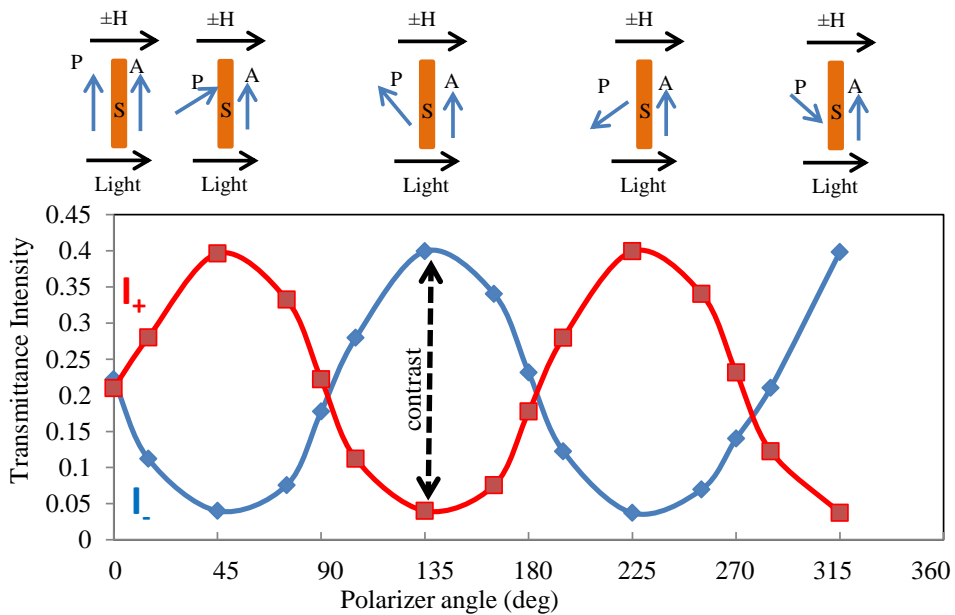
Fig. 1.3 Transmittance intensities through the commercial Faraday rotator where the angle of polarizer is changed under external magnetic field (±H). P is the polarizer, A is the analyzer, S is the sample, I_+ is intensity of light under +H and I_- is the intensity of light under –H.

3

Conventional current driven MOSLMs (iMOSLM) are working based on coil current to provide magnetic field to reverse the magnetization of magnetic garnet as shown in Fig. 1.4. Coil current leads to heat generation and inefficiency of the MOSLM systems.
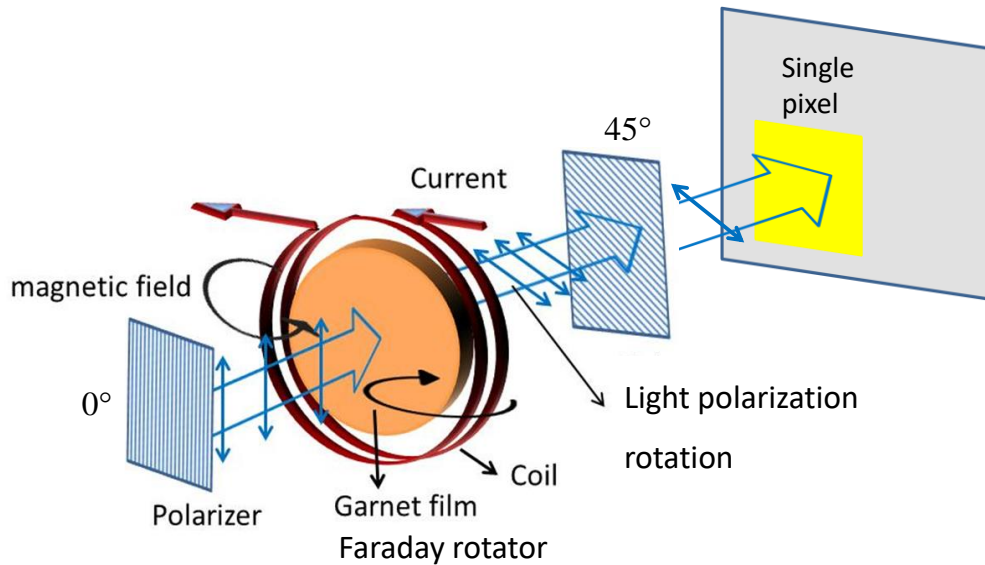
Fig. 1.4. A schematic image of iMOSLM system operated upon magnetization reversal by coil current.

The iMOSLMs have two major technical problems as follows [1].

1- It is necessary to increase the Faraday rotation angle of the magnetic material for higher contrast. Therefore it is necessary to obtain the magnetic garnet having 45° Faraday rotation within visible and near infrared region. Also it is desired that the magnetic garnet films have perpendicular magnetic anisotropy with remanent magnetization for non-volatile properties (no power supply for still image) on MOSLMs

Faraday rotation of 1.8°/μm in $Ce_1Y_2Fe_5O_{12}$ magnetic garnet thin film for application to magnetophotonic crystal (MPC) has been reported, as shown in Fig. 1.5 [2].
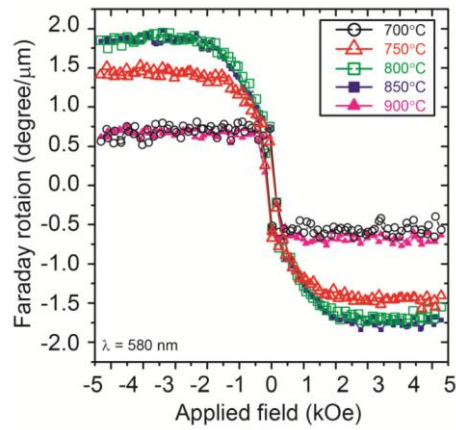
Fig. 1.5 Magnetic field dependence Faraday rotation of the CeYIG/(Ta$_2$O$_5$/SiO$_2$)^8/SiO$_2$/SGGG samples annealed at various temperature (700 -900°C) by ion beam evaporation method. The measurement wavelength was λ = 580 nm [2].

Fig. 1.6 shows a cross-sectional scanning microscope image of a complete MPC consist of the 423 nm thick Ce$_1$Y$_2$Fe$_5$O$_{12}$ magnetic garnet thin film for application to MOSLM [2].
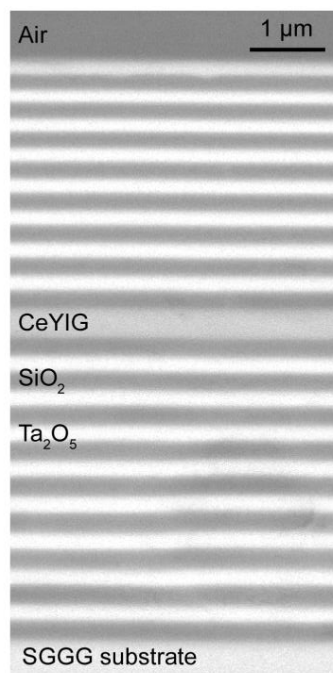
Fig. 1.6 Cross-sectional compositional image of a fabricated MPC consisting of SGGG substrate SiO2/(Ta$_2$O$_5$/SiO$_2$)^8/CeYIG/(SiO$_2$/Ta$_2$O$_5$)^8 [2].

There has been report that BiDyYFeAlG magnetic garnet bfilm is used in MPC for application to 3D holographic display media on 3D-MOSLM. The MPC consisted of BiDyYFeAlG film and Bragg mirrors layers (SiO_2 and Ta_2O_5). Fig. 1.7 shows the transmittance and the Faraday rotation angle of the BiDyYFeAlG mono layer films with different thickness, and a MPC with a 1μm thick BiDyTFeAlG magnetic garnet layer at the wavelength of 532 nm. The Faraday rotation angle and transparency of the MPC were 3.2°/μm and 38% respectively at the wave length of 532 nm [3].
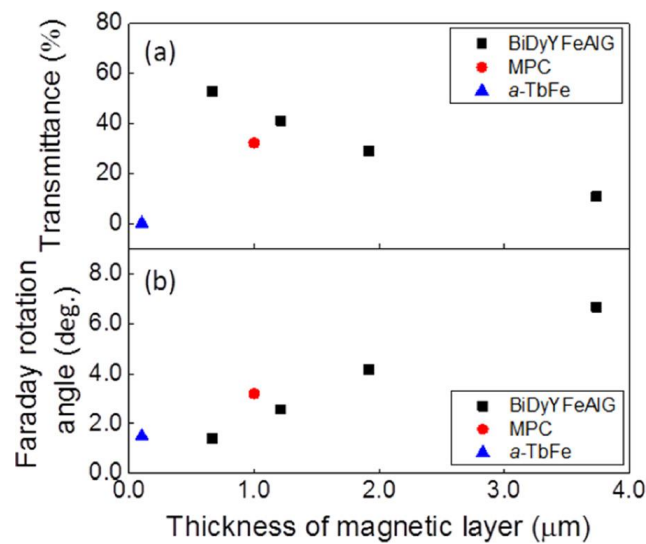
Fig. 1.7 (a) the transmittance of the BiDyYFeAlG, MPC and a-TbFe fabricated magnetic films. (b) The Faraday rotation angle of the BiDyYFeAlG, MPC and a-TbFe fabricated magnetic films. Triangles are a-TbFe, squares are BiDyYFeAlG mono layers, and circles are MPC [3].

Fig. 1.8 (b)–(d) shows the reconstructed 3D holographic image from the MPC with a 1μm thick BiDyTFeAlG magnetic garnet layer. The hologram was represented

on the MPC by an optical addressing system with an SLM, using recording light with λ = 532 nm wavelength [3].
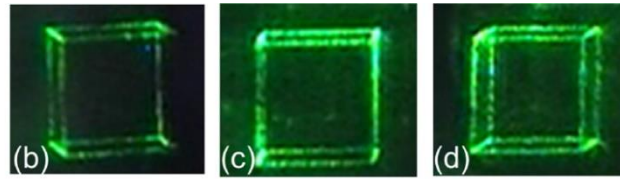
Fig. 1.8 Reconstructed 3D holographic image from MPC with a 1μm thick BiDyTFeAlG magnetic garnet layer [3].

2-   The coil current for providing magnetic field causes power consumption and heat generation that makes them inefficient. Therefore it is necessary to control the magnetic anisotropy and magnetization reversal by novel method, light irradiation or voltage under low DC external magnetic field. Voltage driven MOSLMs are called as vMOSLM.

Fig. 1.9 shows a schematic structure of a single pixel of voltage driven MOSLM.

vMOSLM

Single pixel

Electrode to apply voltage

45°

0°

Bi:GdIG/glass Faraday rotator

Constant magnetic field by a permanent magnet (H)

FR Magnetization

Controlling the magnetic anisotropy

+M   "1"   Ms
Mr
0
Hc   Magnetic field (H)
-M   "0"
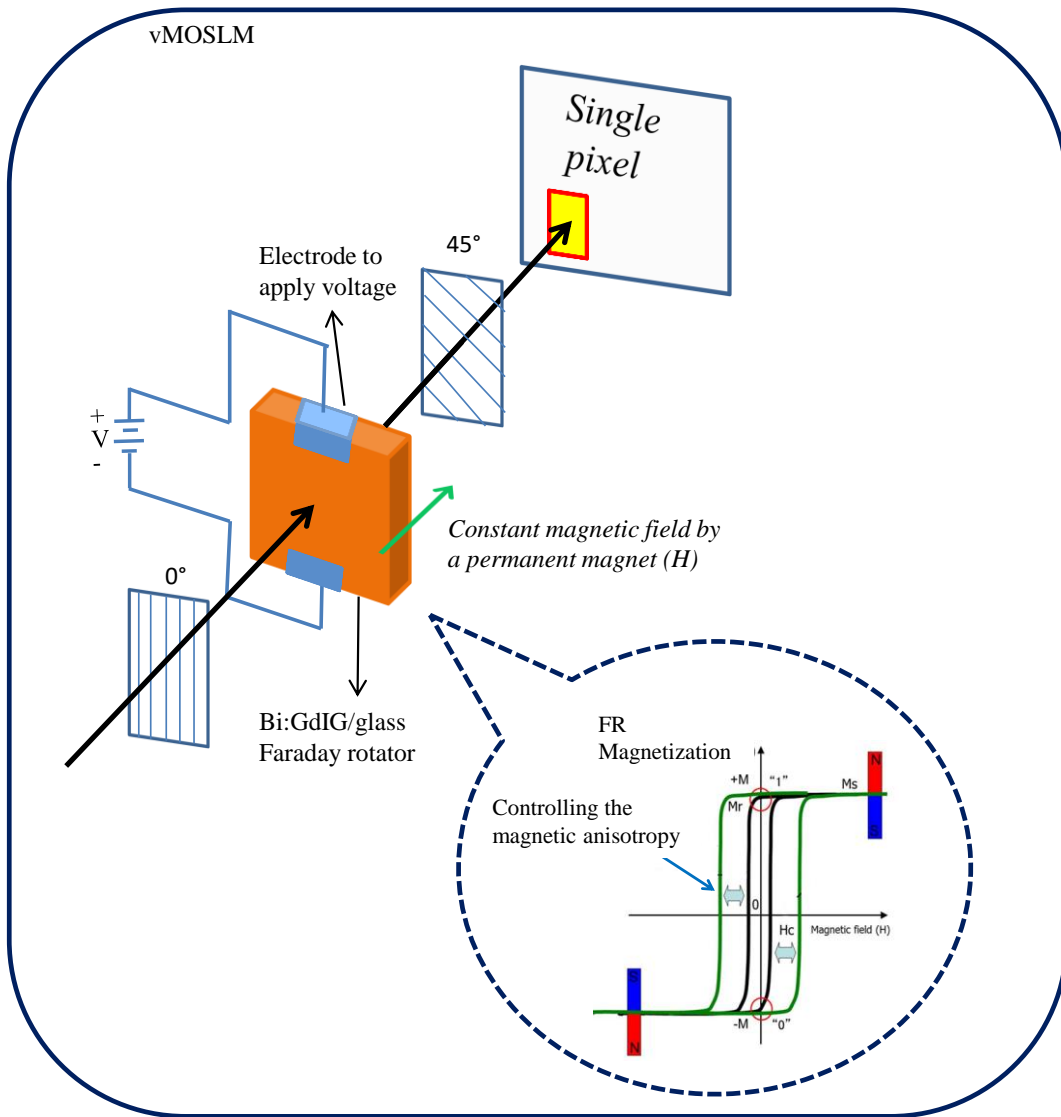
Fig. 1.9 A schematic image of a single pixel of voltage driven MOSLM.

Fig. 1.10 shows the switching mechanism for magnetization in the Bi:YIG magnetic garnet pixel in v-MOSLM by inverse magneto-restriction effect [1].
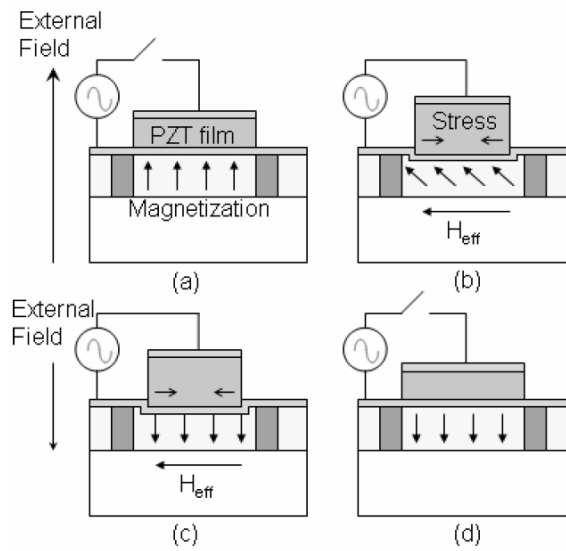
Fig. 1.10 Mechanism of switching magnetization in the magneto-optical Bi:YIG layer in vMOSLM [1].

1.2 Related research

Bismuth substituted gadolinium iron garnet ($Bi_xGd_{3-x}Fe_5O_{12}$) is an important ferrimagnetic material, and exhibits a large Faraday rotation in the visible to near infrared region, which shows perpendicular magnetic anisotropy [4-6]. There are many reported researches on Bi-substituted rare-earth iron garnets such as Bi:GdIG, Bi:YIG and Bi:YGaIG on GGG substrate and glass substrate [7- 10]. Bi-substituted rare-earth iron garnets are the most desirable ferrimagnetic materials and very attractive among all semi-transparent dielectrics for various applications and fundamental investigations for magneto-optical device elements such as magnetoplasmonic structures [11], optical isolators [12], circulators [13-14], and magneto-photonic crystals (MPCs) which are used in magneto-optic spatial light modulators (MOSLM) [1-3,15-17].

In order to apply Bi:GdIG or Bi:YIG thin films to optical waveguide devices such as optical isolators and circulators, and MOSLMs, it is require to prepare the Bi:GdIG thin films having large Faraday rotation and perpendicular magnetic anisotropy. Since the MOD solutions have high stability and long shelf storage life, and the metal organic decomposition (MOD) method is an easy method which enables it to prepare Bi:GdIG / Bi:YIG thin films by spin-coating and annealing process on crystal substrate (GGG) and non-crystal substrate such glass or silicon substrate. The fabrication of magnetic garnet thin film by the MOD method was reported by A. Azevedo, et al, for the first time [18]. Fig. 1.11 shows the M-H hysteresis loops of $Bi_1Gd_2Fe_5O_{12}$ thin film which was fabricated by MOD method [18].

However the influence of O_2 deficiency in the annealing process of MOD method on the magneto optical property and magnetic anisotropy of Bi:GdIG have not been reported yet. In this thesis I report the fabrication of $Bi_1Gd_2Fe_5O_{12}$ thin films on GGG

substrates by the MOD method. I optimized the influence of annealing gas (with and without O_2) and annealing temperature on magnetic anisotropy and magneto optical Faraday rotation of the $Bi_1Gd_2Fe_5O_{12}$ thin films on GGG substrates.

The fabrication of Bi:GdIG/ Bi:YIG thin films on glass substrates is difficult, because of the differences in crystal structure and thermal expansion coefficient between Bi:GdIG or Bi:YIG and glass substrate [19]. The fabrication of Bi:YIG thin films was reported by using $Nd_2Bi_1Fe_4Ga_1O_{12}$ buffer layers on glass substrates by the MOD method. The amount of FR (13.8 deg./μm at $\lambda = 520$ nm) was increased by using $Nd_2Bi_1Fe_4Ga_1O_{12}$ buffer layer [20]. Fig. 1.12 shows the magnetic field dependence of Faraday rotation of $Bi_{2.5}Y_{0.5}Fe_5O_{12}$ thin films at the wavelength of 520 nm, fabricated on glass substrate using bismuth substituted Nd- Gd- and Y iron garnet buffer layers [20].

In this thesis I report the fabrication of $Bi_xGd_{3-x}Fe_5O_{12}$ with different amount of x = 1, 2 and 2.5 annealed at various annealing temperature (620-700°C) on glass substrate. And I fabricated the $Bi_{2.5}Gd_{0.5}Fe_5O_{12}$ thin film on glass substrate using $Gd_3Fe_5O_{12}$ buffer layer by enhanced metal organic decomposition (EMOD) method. We are the first trial of EMOD method for fabrication of Bi:GdIG thin films. I reported the optimization of the thickness of the $Gd_3Fe_5O_{12}$ buffer layer and annealing temperature for crystallization in order to maximize the FR of the $Bi_2Gd_1Fe_5O_{12}$ thin films on glass substrates by MOD method. I will discuss the crystallization process and relationship between the crystalline quality and FR among various preparation conditions for the fabricated samples.
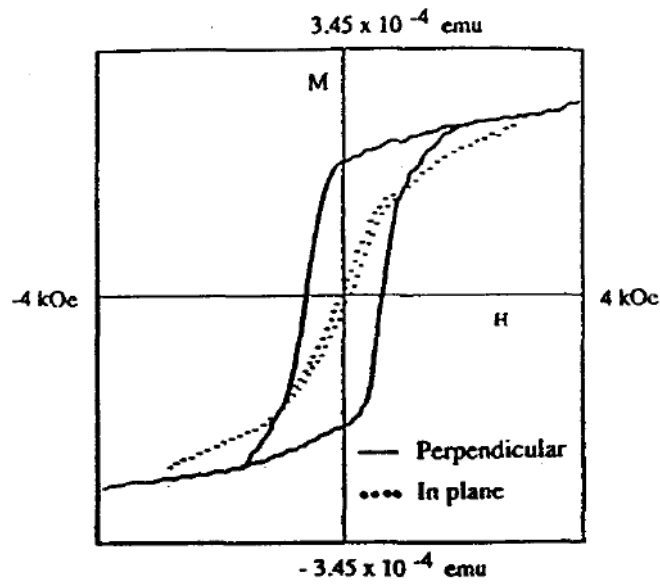
Fig. 1.11 M-H hysteresis loops for in-plane and perpendicular direction of $Bi_1 Gd_2Fe_5O_{12}$ thin film. Tins film is fabricated by MOD method on glass substrate [18].
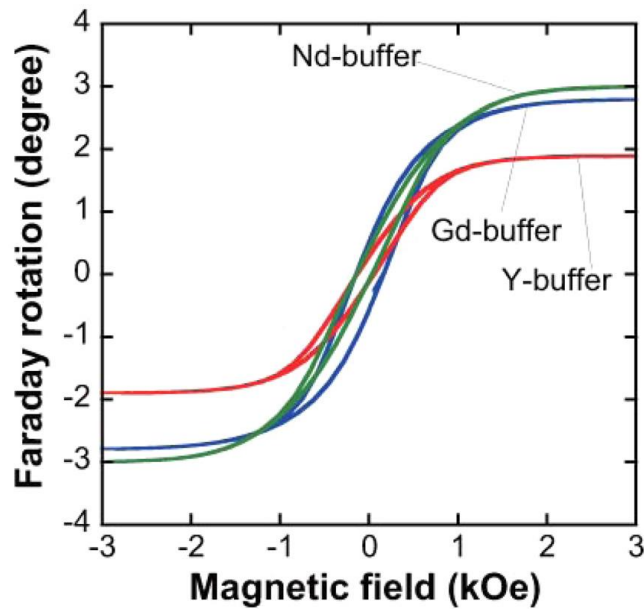
Fig. 1.12 Faraday hysteresis loops of $Bi_{2.5}Y_{0.5}Fe_5O_{12}$ thin films prepared on Y-, Gd-, and Nd-iron garnet buffer layers by MOD method [20].

1.3 Purpose of this research

The purpose of my research is to fabricate the magnetic garnet with larger Faraday rotation (ideal Faraday rotation is 45 deg.) and to control the magnetic anisotropy of magnetic garnet by controlling the carrier concentration or strain in the film and changing the fabrication conditions for application in MOSLM as schematically shown in Fig. 1.13. Research on the ferrimagnetic garnet and their application to MOSLM is an important in the field of spintronics.

Spintronics is a relatively new in the field of science and technology. In particular, the research on the ferromagnetic magnetic material and voltage control of the magnetization has drawn attention of scientists and researchers in the world. It is a subject that we need it for our country (Afghanistan) development, because it is new, practically interesting and theoretically advanced subject. On the other hand because Afghanistan is a war hit and developing country, it needs to be involved with new subject of science and technology in order to become sustainable and move forward toward development. However we do not have anything to get involved in research in this field, I tried to achieve this goal. It shall be included to the curriculum of the faculty of Engineering at Kabul University. Beside this I tried to achieve necessary knowledge to establish associated lab with it. Hence, it is my honor and I am highly proud and have highly interested in the research on ferrimagnetic garnet in the Tokyo University of Agriculture and Technology and I would like to transform my knowledge to my country Afghanistan.
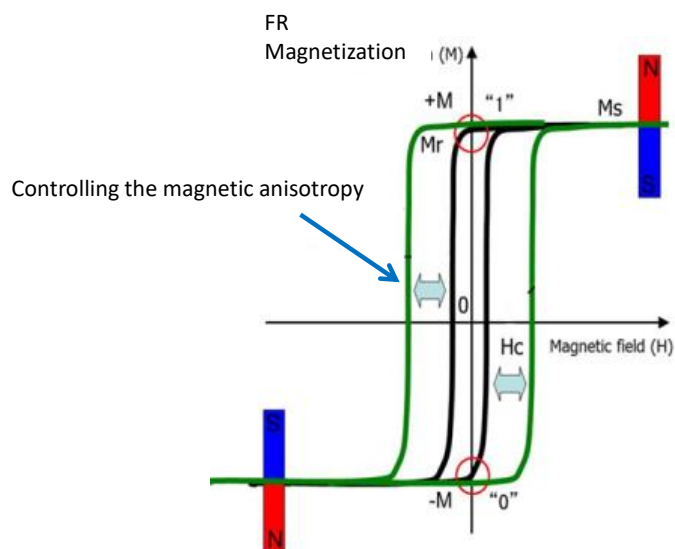
Fig. 1.13 A schematic image for controlling the magnetic anisotropy under DC external magnetic field. The magnetization becomes up and down (on and off) by controlling the magnetic anisotropy under constant magnetic field.

1.4 Content of this thesis

In chapter 2, I will discuss on atomic magnetic moments of rare earth elements, magnetic and magneto optical properties of rare-earth iron garnet, mechanism of magnetic anisotropy, and the physics and magneto optical properties of yttrium iron garnet, gadolinium iron garnet and bismuth substituted gadolinium iron garnet.

In chapter 3, I will explain the metal organic decomposition (MOD) method for preparation of thin films, discuss the advantage and disadvantage of MOD method and compare with several fabrication methods. Furthermore I will explain on the principle of characterizations of the magnetic garnet thin films. Those are X-ray diffraction (XRD), optical transmittance / reflectance, magneto optical Faraday rotation (FR) and magnetization measurements.

In chapter 4, I will discuss on preparation and characterization of $Bi_1Gd_2Fe_5O_{12}$

films by MOD method on (111) GGG and glass substrates in different annealing temperature of $620-800\ ^{\circ}$C and different annealing gases (80%N_2+20% O_2 and 100% N_2) in order to investigate the influence of the oxygen gas on the magnetic anisotropy of the magnetic garnet. I discuss on the characteristic and relationship among the Faraday effect, magnetic anisotropy, and fabrication conditions.

In the chapter 5, I will discuss on preparation and characterization of $Bi_xGd_{3-x}Fe_5O_{12}$ thin films with various amount of bismuth substitution (x) under various annealing temperature for crystallization in order to investigate the effect of changing the Bi content x and annealing temperature on FR of the $Bi_xGd_{3-x}Fe_5O_{12}$ thin films on glass substrates. I used the EMOD solutions containing a metal oxide carboxylate in xylene which can be mixed with other EMOD solutions containing other metal oxide [detail about EMOD is described in chapter 3]. Also, I will discuss on the fabrication and characterization of the $Bi_xGd_{3-x}Fe_5O_{12}$ thin films with higher Bi content $x = 2.5$ with $Gd_3Fe_5O_{12}$ buffer layer in order to prepare the sample with larger FR by the EMOD method on glass substrate.

In the chapter 6, I will discuss on the fabrication of the $Bi_2Gd_1Fe_5O_{12}$ thin films by using $Gd_3Fe_5O_{12}$ buffer layer on glass substrates by the MOD method in order to optimize the fabrication conditions such as the crystallization temperature and thickness for the $Gd_3Fe_5O_{12}$ buffer layer. I changed the thickness and crystallization temperature for the $Gd_3Fe_5O_{12}$ buffer layers in order to maximize the FR of the $Bi_2Gd_1Fe_5O_{12}$ thin films on glass substrates. I will discuss the relationship between the crystalline quality and FR by changing the $Gd_3Fe_5O_{12}$ buffer layer thickness and crystallization temperature.

In chapter 7 I will conclude this research.

The content of my experiments is summarized in Table 1.1.

Table 1.1. Content of my experiment, chapters 4, 5 and 6.

Chapter	Material	substrate	Method	Annealing gas	Purpose
4	$Bi_1Gd_2Fe_5O_{12}$	GGG	MOD	100%N_2 Or 80%N_2 + 20%O_2	Influence of the T_{FA} and annealing gas
5	$Bi_xGd_{3-x}Fe_5O_{12}$ (X=1, 2, 2.5)	Glass	EMOD	80%N_2 + 20%O_2	Influence of the amount of Bi substitution and T_{FA}
6	$Bi_2Gd_1Fe_5O_{12}$	Glass	MOD	80%N_2 + 20%O_2	Influence of buffer layer

CHAPTER 2

Magnetism of Rare-earth iron garnet and mechanism of magnetic anisotropy

2.1 Introduction

Magnetic garnet is a group of several closely related minerals that can be found in many different varieties and seen in many varieties of colors including red, orange, yellow, green, purple, brown, blue, black, pink and colorless. All types of garnets own similar physical properties and crystal forms, but differ in chemical composition. Optical transmission of garnet can range from the gemstone-quality transparent specimens to the opaque varieties. Some types of garnet have ferrimagnetic properties with high transparency and large magneto optic effect, these properties make them ideal and perfect for many electronic and magneto-optical devices application.

Rare earth iron garnets are ferrimagnetic oxides which are the most desirable materials for magneto optical devices due to their high optical transmittance and magneto optical activity. As shown in Fig. 2.1, we can mix several kinds of rare earth ions on 24c sites, and put Fe^{3+} on 24d or 16a sites. It is possible to replace Fe^{3+} by Al^{3+},

Ga^{3+} or introduce Si^{4+} or Ge^{4+} ions together with the same number of Ca^{2+} or Mg^{2+} ions. By such kind of substitution of non-magnetic ions, we can control the compensation point, saturation magnetization, magneto crystalline anisotropy, g-factor, lattice constant, etc [1].

Yttrium iron garnet (YIG) $Y_3Fe_5O_{12} = 3/2\{(Y^{3+})_2O_3\} + 5/2\{(Fe^{3+})_2O_3\}$ is one of widely well-known ferrimagnetic rare earth iron garnets, due to its large magneto optic effect, high transparency, leading to large potential in the fields of optics, magneto-optic modulator [2], isolators [3], and microwave devices [4], circulators [5 - 7], etc...

In chapter 2, I explain the atomic magnetic moments of rare earth elements, magnetic properties of ferrimagnetic rare earth iron garnets, physics and magnetic properties of Yttrium iron garnet and Gadolinium iron garnet. And I explain the mechanism of magnetic anisotropy including magneto crystalline anisotropy.
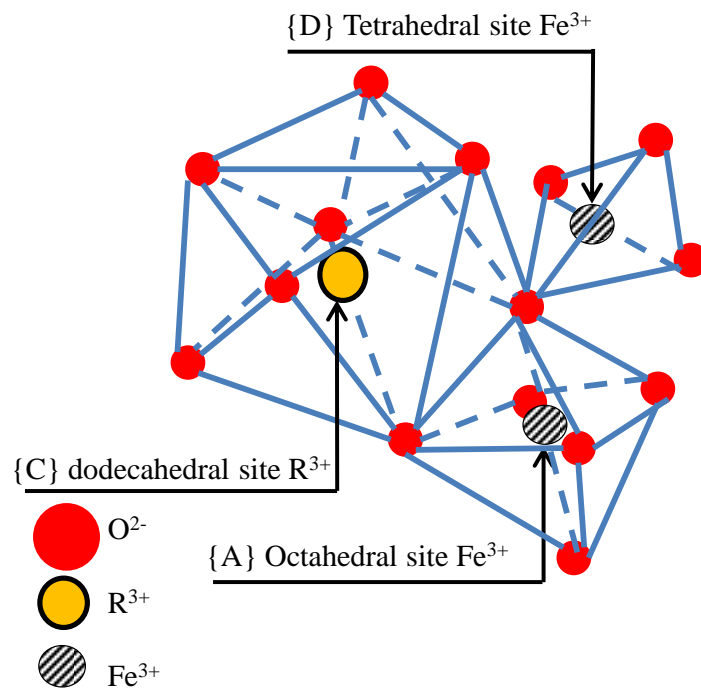
Fig. 2.1 Crystal structure of rare-earth iron garnet.

2. 2. Atomic magnetic moments of rare earth elements

The rare earth elements have $(4f)^n(5s)^2(5p)^6(5d)^1(6s)^2$ electronic structure in which the outer $(5s)^2(5p)^6$ shells protect the incomplete 4f shell from outside disturbance well so that its orbital magnetic moment is well preserved or unquenched by the crystalline field. The outermost electrons $(5d)^1(6s)^2$ are easily removed from the neutral atom, thus producing trivalent ions in ionic crystals and conduction electrons in metals or alloys. Therefore the atomic magnetic moments of rare earth elements are more or less the same as in both compounds and metals. In the rare earth elements, by increasing the number of 4f electrons (n), spin magnetic moment (s) increase from La $(4f^0)$ to Gd, $(4f^7)$ and then decreases to Lu (f^{14}) linearly. In rare earth elements, the value of angular momentum (L) increases from 0 at Lanthanum to values of 3, 5, and 6 and then decreases towards 0 at Gadolinium with $4f^7$, where a half-shell is just filled. A half-shell this state and a completely filled $4f^{14}$ state are called spherical. The total angular momentum, J changes, because, J = L – S for n = 0 to n = 7, while J = L + S for n = 7 to 14. So J is relatively small for n < 7, while it is relatively large for n> 7 as shown in Fig. 2.2.
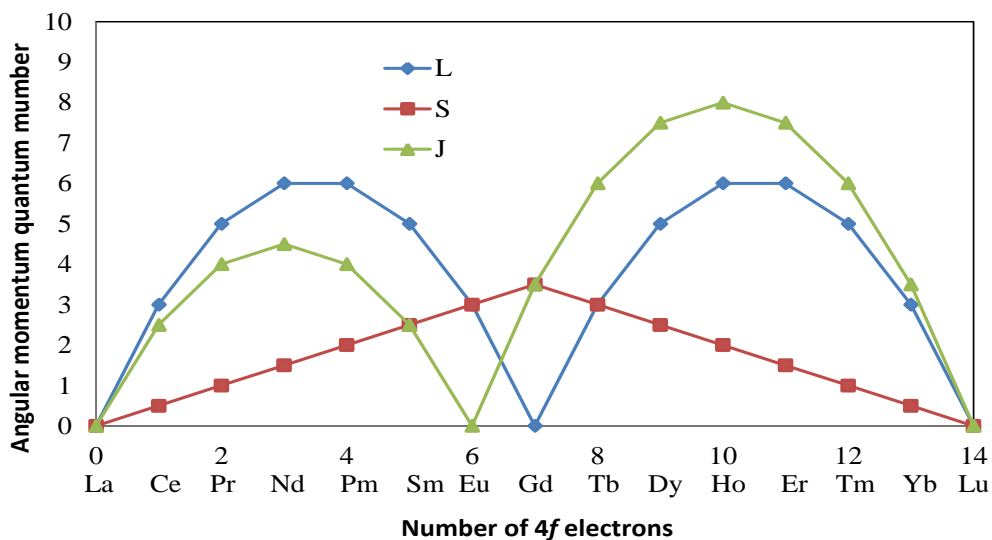
Fig. 2.2 Spin S, orbital L, and total angular momentum J as function of the number of 4f electrons of trivalent rare earth ions.

2.3 Magnetic properties of Rare Earth Iron Garnets

Ferrimagnetic rare-earth iron garnets (RIG) have the general formula of $R_3Fe_5O_{12}$, where R stands for one or more of the rare earth ions such as Y, Sm, Eu, Gd, Tb, Dy, Ho, Er, Tm, Yb, Lu, etc. The crystal structure of the rare earth iron garnet is the cubic oxide garnet-type with a unit cell of 160 atoms. One formula unit of the garnet contains three dodecahedral, two octahedral, and three tetrahedral positions ($\{C\}_3[A]_2(D)_3X_{12}$), where C is a large dodecahedral site, A is a moderately sized octahedral site, D is a small tetrahedral site, and X is an anion site that is most commonly occupied by oxygen consisting of 96 O^{2-} ions. The trivalent rare earth ions R^{3+} occupy the 24c sites of dodecahedral sites which are surrounded by 8 oxygen (O^{2-}) ions forming a

dodecahedron. The Fe^{3+} ions occupy 24d, or octahedral, sites, surrounded by six oxygen ions. In the tetrahedral position or 16a, the iron ion is bonded to four oxygen ions as shown in Fig. 2.1.

The main superexchange interaction is between the tetrahedral and octahedral iron ions. This interaction gives rise to antiparallel ordering of the magnetic moments in the octahedral and tetrahedral iron sub-lattices and hence the net magnetization is parallel to the magnetic moments in the tetrahedral direction. When magnetic rare-earth ions are placed in dodecahedral position they form a third magnetic sub-lattice in the dodecahedral magnetic sub-lattice. The main exchange interaction between the rare earth and iron ions is the interaction between the dodecahedral rare earth lattice and the tetrahedral iron lattice.

Since the interaction between R^{3+} ions is very weak, the R^{3+} moments behave para-magnetically under the exchange fields produced by the Fe^{3+} spins. Therefore, as temperature increases, the sub-lattice moment of R^{3+} ions decreases sharply, as shown in Fig. 2.3. As seen in this graph, the Curie point is almost the same for all RIGs, since only the exchange interaction Fe^{3+} survives at high temperatures.

This situation is explained by the Neel as below: under the external field H, the sub-lattice magnetization I_R of the rare earth site is given by

$$I_R = x(H + wI_{Fe}) \qquad\qquad (2.1)$$

Where I_{Fe} is the total sub lattice magnetization of Fe^{3+} ions on 24d and 16a sites, w is the molecular field coefficient, and x is the paramagnetic susceptibility of rare earth ions. Then the total magnetization (I) is given by

$$I = I_{Fe} + I_R = I_{Fe} + x(H + wI_{Fe}) = I_{Fe} (1 + xw) + xH \qquad\qquad (2.2)$$

On the right side of equation (2.2) the first term is saturation magnetization, while the second part is the incremental induced magnetization by external magnetic field. From the first term, we can find that the saturation magnetization vanishes either when

$$I_{Fe} = 0 \qquad\qquad (2.\,3)$$

In which Curie point is realized, or when

$$1+ xw = 0 \qquad therefore \quad x = -\,1/w \qquad\qquad (2.4)$$
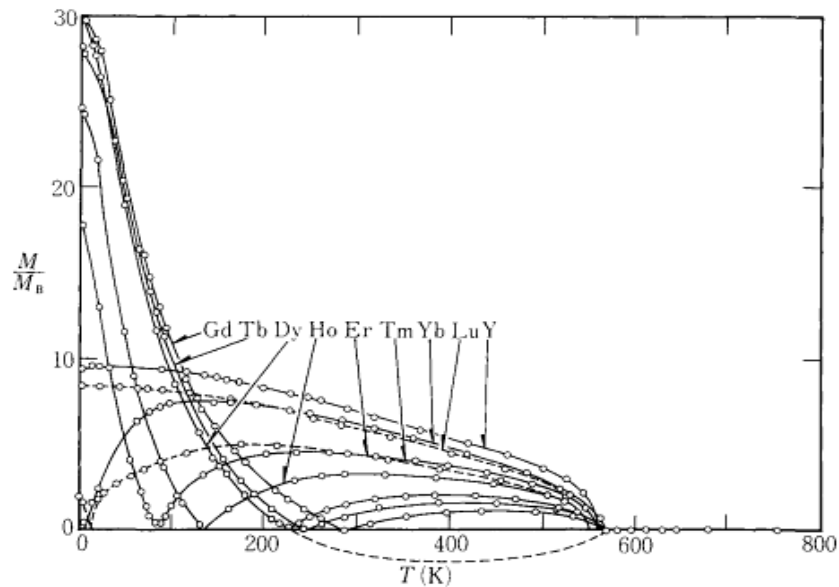
Fig. 2.3 Temperature dependence of molar saturation moment of various rare earth iron garnets [1].

The x is inversely decreases with the absolute temperature because it is the paramagnetic susceptibility and it will satisfy the condition at some temperature and this temperature is called the compensation point, Θc. Table 2.1 shows that the value of Θc decreases with the increase of the number of 4f electrons in rare-earth iron garnet because the spin magnetic moment S decreases, so that the value of w decreases [1]. The resistivity of magnetic garnet is very high, giving low magnetic losses even at high

frequencies because they contatin only trivalent ions, with no divalent ions, therefore no electron hopping occurs. Thin garnet crystals are transparent, so that optical magnetic properties can be observed by Faraday effect.

Fig. 2.4 shows the effects of temperature on magnetic properties of ferrimagnetic materials. By changing the temperature of ferimagnetic material, the magnetization changes to the zero magnetization, compensation point and Curie point.

At high temperatures, the atoms in an object vibrate strongly, and loss their alignments. This temperature is called Curie point, or Curie temperature. In general, ferromagnetic materials have higher Curie Temperatures than ferrimagnetic materials. For example, the ferromagnetic metal, cobalt, has a Curie temperature of 1,131°C where Yttrium iron garnet has lower Curie temperature of 560°C.

Some magnetic domains in a ferrimagnetic materials point in the same direction and some in the opposite direction. The ferromagnetic materials have stronger magnetic field compared to ferrimagnetic materials with the same size.
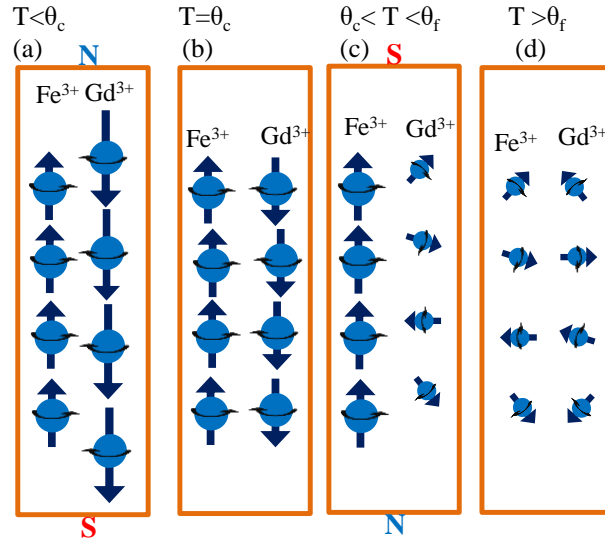
Fig. 2.4 Spin alignment of ferrimagnetic materials, (a) case for spontaneous magnetization below the compensation point ($T<\theta_c$), (b) at the compensation point ($T=\theta_c$) the magnetic components are cancelled with each other and the total magnetization is zero, (c) between the compensation and Curie point, direction of the magnetic moment of rare-earth ions are random, only the magnetic moment of Fe^{3+} survive at higher temperature ($\theta_c<T<\theta_f$), (d) above the Curie point ($T>\theta_f$) the material loses their ferromagnetism.

R^{3+}	M_{mol} (0 K, M_B)	I_S (300 K, T)	$M(R^{3+})$ (0 K, M_B)	Θ_f (K)	Θ_c (K)	Θ_a (K)	Lattice const. (Å)	Density (g cm^{-3})
Y	5.0	0.170	0	560	—	—	12.38	5.169
Sm	5.43	0.160	0.14	578	—	—	12.52	6.235
Eu	2.78	0.110	−0.74	566	—	—	12.52	6.276
Gd	16.0	0.005	−7.0	564	286	−24	12.48	6.436
Tb	18.2	0.019	−7.7	568	246	−8	12.45	6.533
Dy	16.9	0.040	−7.3	563	226	−32	12.41	6.653
Ho	15.2	0.078	−6.7	567	137	−6	12.38	6.760
Er	10.2	0.110	−5.1	556	83	−8	12.35	6.859
Tm	1.2	0.110	−1.3	549	—	—	12.33	6.946
Yb	0	0.150	−1.7	548	—	—	12.29	7.082
Lu	5.07	0.150	0	539	—	—	12.28	7.128

Table 2.1 Magnetic and crystalline properties of rare earth iron garnets [1].

By mixing several kinds of rare earth ions on 24c sites, or to replace Fe^{3+} on 24d or 16a sites by Al^{3+} or Ga^{3+} or introduce Si^{4+} or Ge^{4+} ions together with the same number of Ca^{2+} or Mg^{2+} ions. By such kind substitution of non-magnetic ions, we can control the compensation point, saturation magnetization, magneto crystalline anisotropy, g-factor, lattice constant, etc [1].

2.4 Yttrium Iron Garnet

Yttrium iron garnet is one of the important and well-known rare earth iron garnets and ferrimagnetic material. The chemical formula of yttrium iron garnet is $iY_3Fe_5O_{12} = 3/2\{(Y^{3+})_2O_3\} + 5/2\{(Fe^{3+})_2O_3\}$. The YIG crystal unit contains three dodecahedral, two octahedral, and three tetrahedral positions ($\{C\}_3[A]_2(D)_3X_{12}$), in which the iron oxide (Fe^{3+}) occupies three tetrahedral (D) sites and two octahedral [A] sites and Y^{3+} occupy three dodecahedral {C} sites. 96 oxygen ions surround the 3 sites. Fig. 2.5 shows the crystal structure of YIG. The YIG shows different spin orientation in tetrahedral site and octahedral site, where the total magnetic moment direction is parallel with tetrahedral sites. The dodecahedral site does not shows magnetic moment, because the Y^{3+} ion is non-magnetic material. Each Fe^{3+} has magnetic moment of 5 Bohr magnetrons (μ_B) at 0K. Thus each formula unit has a $5\mu_B$ magnetic moment at 0K [1, 8].

$-\dfrac{1}{4},\dfrac{1}{2},0$

$\dfrac{1}{4},\dfrac{1}{2},0$

$\dfrac{1}{4},\dfrac{1}{2},\dfrac{1}{2}$

$0,0,0$

$\dfrac{1}{4},0,\dfrac{1}{2}$
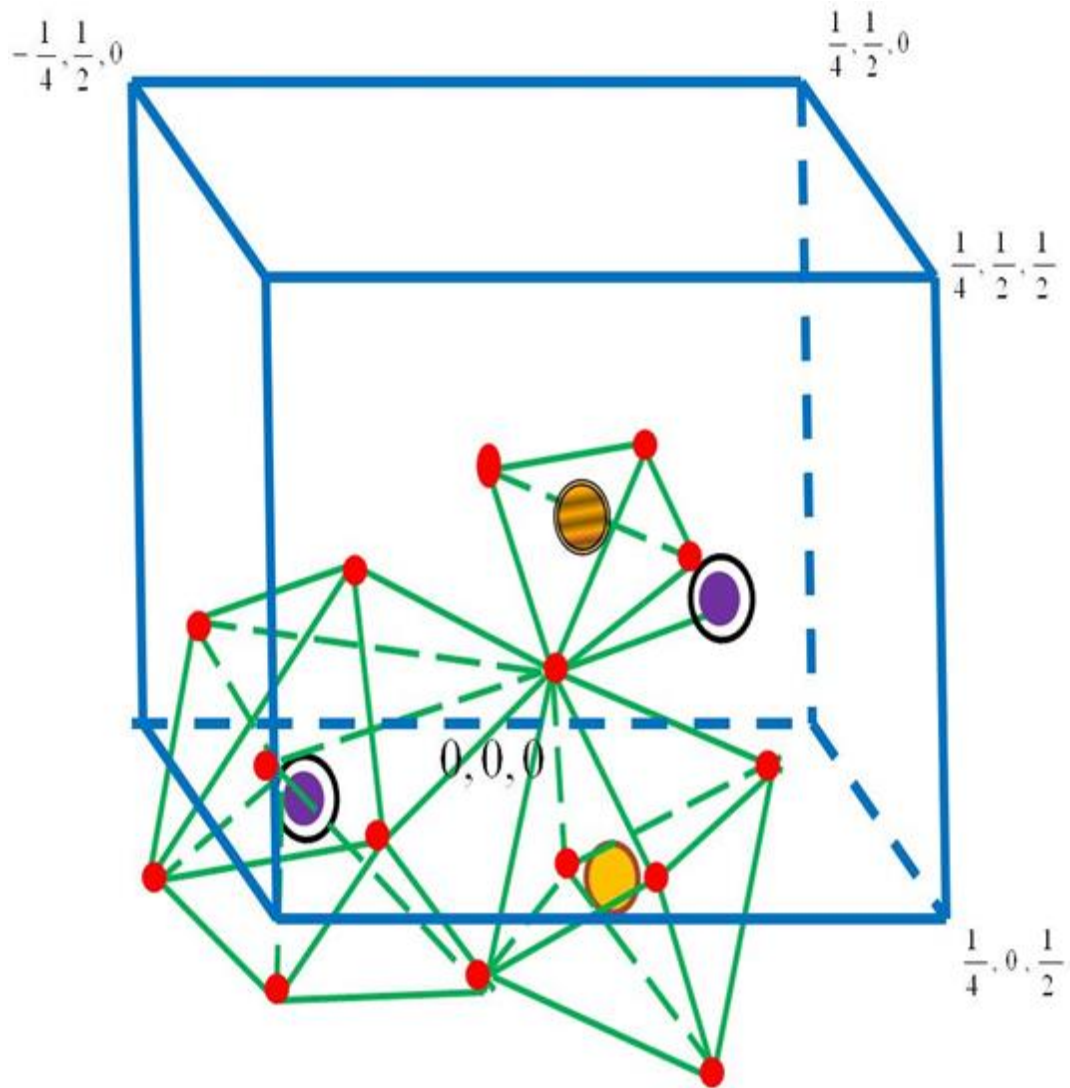
$Y^{3+}at(\dfrac{1}{4},\dfrac{1}{8},\dfrac{1}{2})\&(0,\dfrac{1}{4},\dfrac{5}{8})$

$F^{3+}(A)at(0,0,\dfrac{1}{2})$

$F^{3+}(D)at(0,\dfrac{1}{4},\dfrac{3}{8})$

O^{2-}

3x ↑↑↑↑↑ tetrahedral site
2x ↓↓↓↓↓ Octahedral site
1x ↑↑↑↑↑ Total magnetic moment

Fig. 2.5 Position of each sub-lattice site in the yttrium iron garnet crystal structure.

The large and open structure of YIG allows different elemental substitutions. The substituting elements have their preferred sites depending on the atomic diameter of the substituting ions. Substitutions for atoms influence on structural, magnetic, optical and MO properties. Bismuth and cerium are two representative substitutions for enhancing MO effect [8].

2.5 Magnetic anisotropy in a cubic crystal

The dependence of magnetic properties of a magnetic material to preferred direction is called magnetic anisotropy. The directions of magnetic moment of an anisotropic magnetic material are tended spontaneously to preferred direction without applying external magnetic field, which is called easy axis. On the other hand a magnetically isotropic material has no preferential direction for its magnetic moment except there is an applied external magnetic field.

There are several different types of magnetic anisotropy, which are basically classified in magneto crystalline anisotropy, shape anisotropy and induced magnetic anisotropy (inverse magneto restriction effect).

2.5.1   shape anisotropy

Easy magnetization direction is parallel to the plane of magnetic films, because demagnetic fields and diamagnetic field are smaller for in plane direction. When a magnetic material of finite size is magnetized by an external magnetic field the free poles which appear on its ends will produce a magnetic field directed opposite to the magnetization (Fig. 2.6), this field is called the demagnetizing field. The intensity of the demagnetizing field H_d is proportional to the magnetic free pole density and to the magnetization.
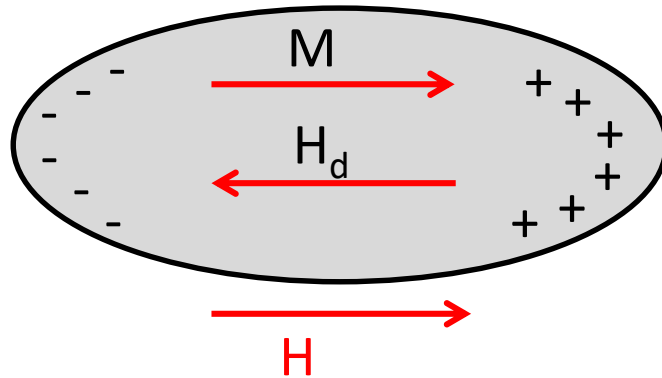
Fig. 2.6 Surface magnetic free poles and resulting demagnetizing field produced by magnetization parallel to surface of film.

2.5.2 Induced anisotropy

The magnetic anisotropy of magnetic material depends on the induced strain/stress during the thin film preparation process. The difference of thermal expansion between the film and substrate during the heating or cooling leads to strain/stress effect and change the magnetic anisotropy of magnetic material as shown in Fig. 2.7.
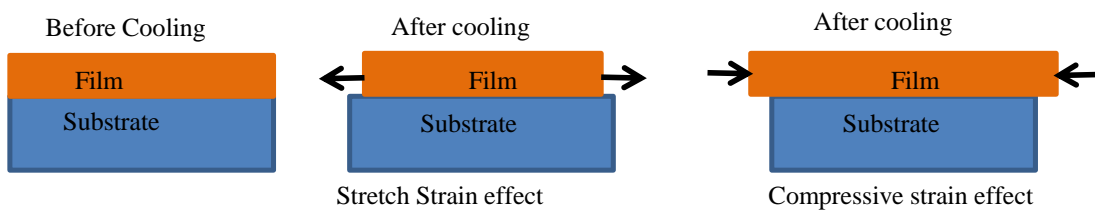
Fig. 2.7 Schematic image of induced magnetic anisotropy produced by the difference of thermal expansion between substrate and film.

2.5.3 Magneto crystalline anisotropy

Magneto crystalline anisotropy is the most common anisotropy, which is caused by the spin-orbit interaction of the electrons. The electron orbitals are linked to the crystallographic structure, and by their interaction with the spins they make alignment with crystal axis. Therefore, there are directions in space, in which a magnetic material is easier to be magnetized than in others. The magneto crystalline energy has the same symmetry as the crystal structure. The direction of the magnetization is determined only by the anisotropy, because the exchange interaction just tries to align the magnetic moments parallel, no matter in which direction as shown in Fig. 2.8.
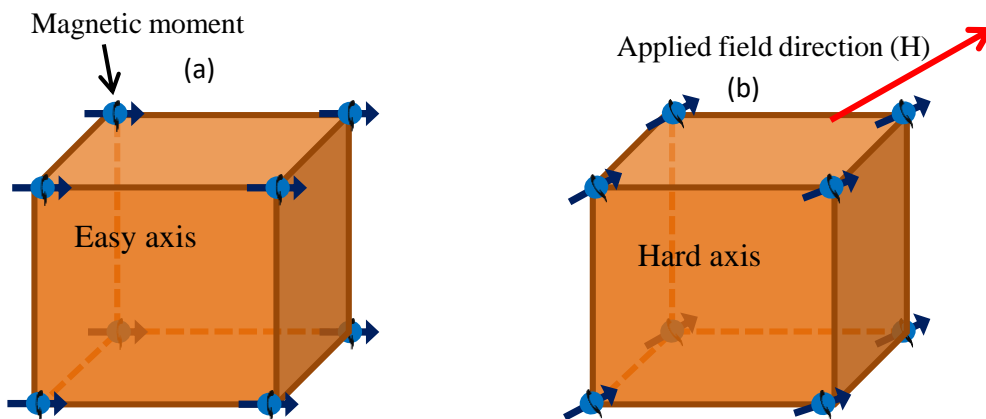
Fig. 2.8 Schematic image of magnetic crystal anisotropy in cubic crystal structure, (a) spontaneous magnetization (easy axis) has the same symmetry as crystal structure without applied field. (b) Magnetization direction is changed in hard axis by applying external magnetic field.

In the transition metal atoms, the wave functions of d-electrons are classified and separated into three d_ε and two d_γ functions when they are placed in a cubic lattice. Fig. 2.9 shows the angular distribution of these wave functions and Fig. 2.10 shows the p-orbital wave function [9].
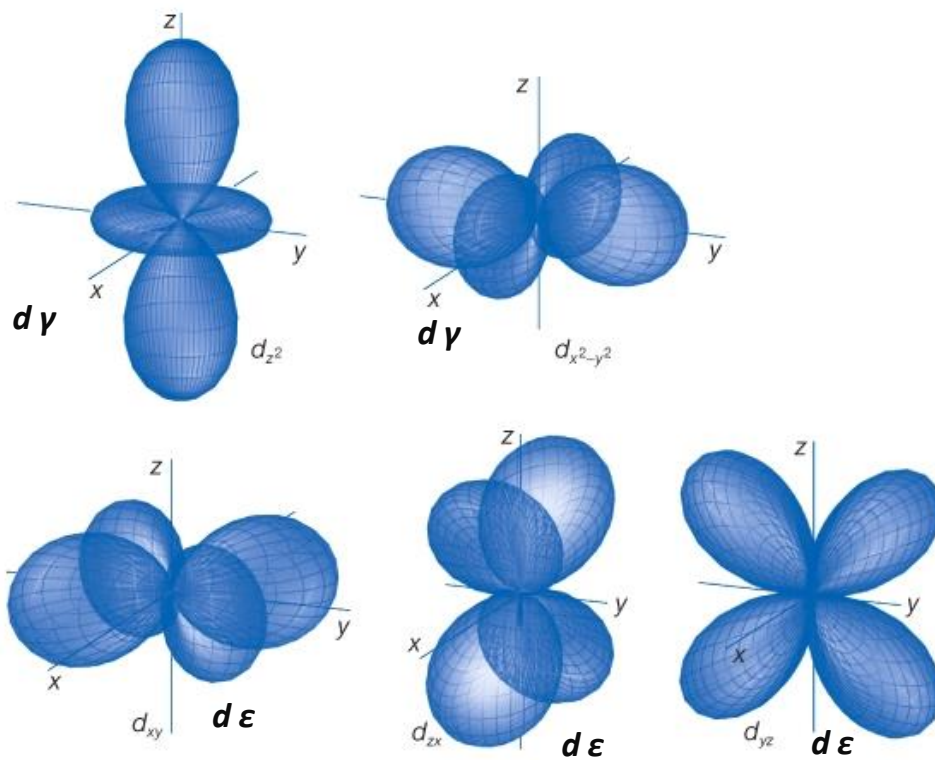
Fig. 2.9 The d(ε) and d(γ) wave functions of 3d electrons in a cubic ligand field [9].
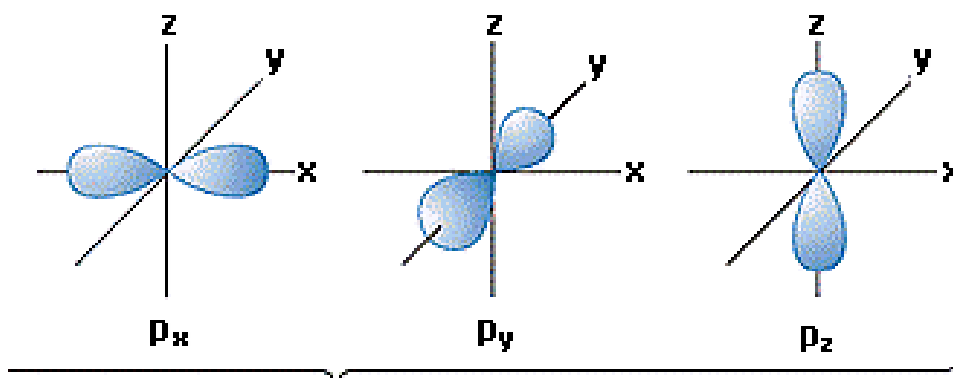
Fig. 2.10 The p-orbital wave functions of oxygen [9].

The dε stretch along <110> axis and dγ stretch along the cubic axis <100>, the magnetic crystalline anisotropy of an oxide crystal is brought by the difference of coulomb interaction between the d_ε or d_γ orbitals of Fe^{3+}, and p orbitals of O^{2-} as shown in Fig. 2.11.

(a)   (b)
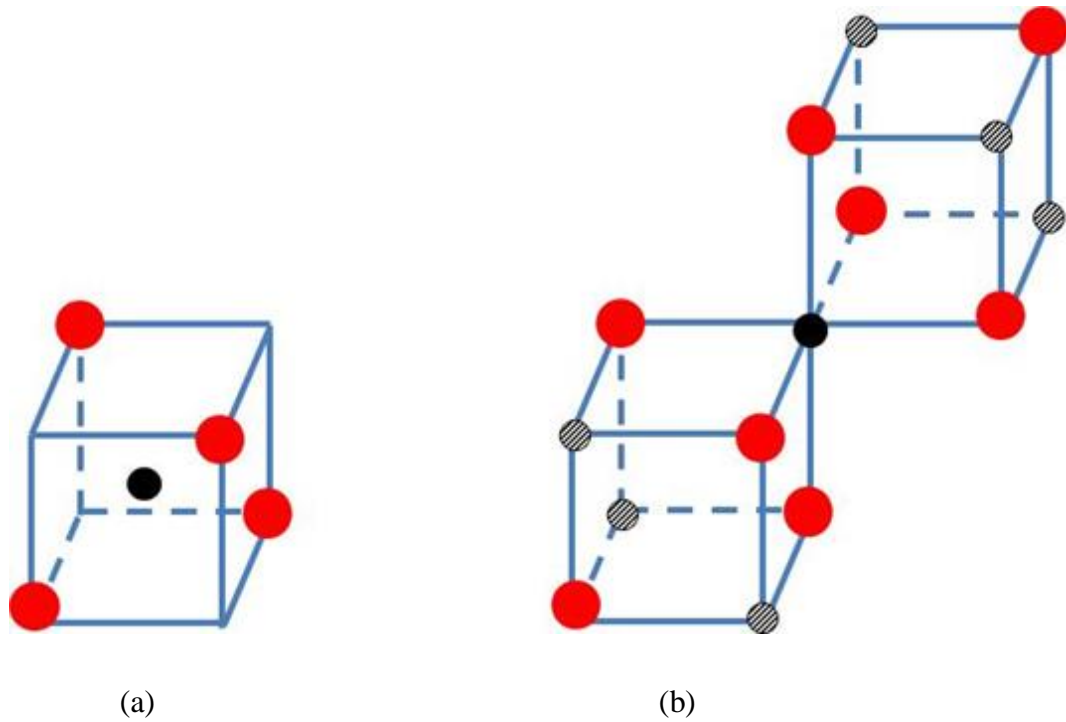
🔴 Oxygen ion

⚫ Metal ion

◒ Nearest neighbor metal ions surrounding the octahedral sites

Fig. 2.11 Interstitial sites of Fe^{3+} in an oxide lattice: (a) tetrahedral site (b) octahedral sites.

The divalent oxygen ions (O^{2-}) are forming a closely packed structure in oxide crystal, because they are indirectly interacted with each other. The divalent or trivalent metal ions (M^{2+} or M^{3+}) are squeezed into interstitial sites of the oxygen lattice because they are much smaller than the O^{2-} ions (radius 0.6 – 0.8 Å of metal ions as compared to 1.32 Å for oxygen ions O^{2-}). There are two kinds of interstitial sites. One is called tetrahedral site, surrounded by the four nearest neighbor O^{2-} ions, and the other is called octahedral site, surrounded by the six O^{2-} ions. In all the oxides, metal ions occupy these small interstitial sites [1]. The energy levels of d-electrons are splitted into doubly degenerate d_γ levels and triply degenerate d_ε levels when they are placed in an octahedral site as shown in Fig. 2.12.
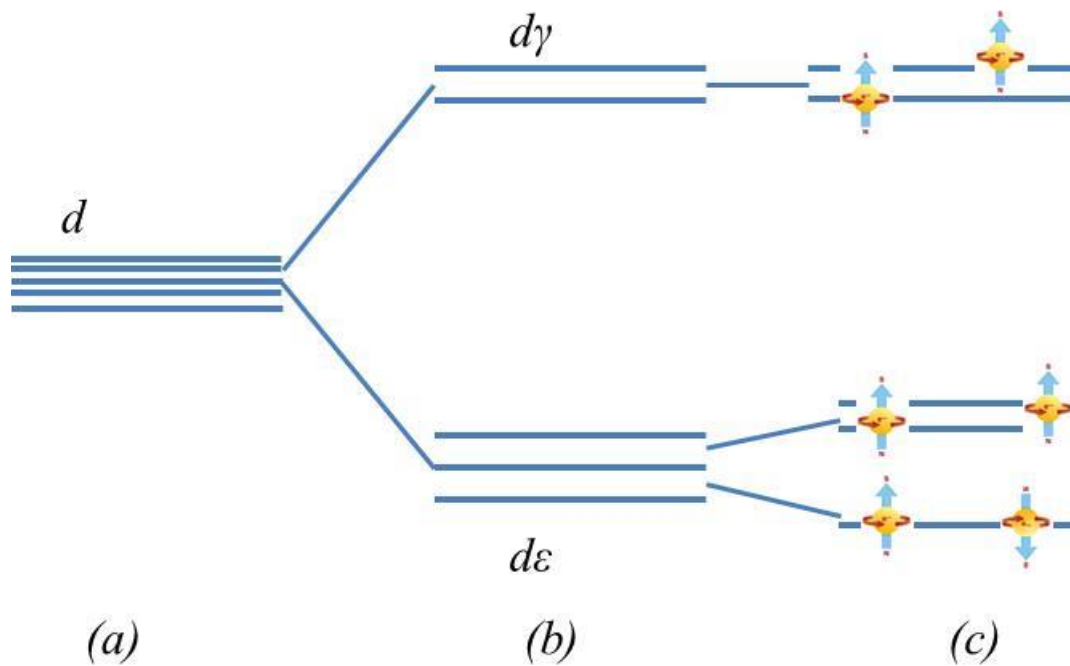
Fig. 2.12 Schematic image of the Splitting of energy levels of 3d electrons by crystalline fields: (a) free ions, (b) cubic fields similar to the case in Fe^{3+} in magnetic garnet (c) trigonal field (arrows represent the spin in a Fe^{3+} Iron ions).

Because the dγ wave function stretches along a cubic axis on which the nearest neighbor O^{2-} ion is located. However the coulomb interaction between the negatively charge electron (dγ) and the O^{2-} ion/ and the energy level of dγ is higher than that of *dε*, while the *dε* wave function stretches between two cubic axes and avoids the O^{2-} ions so that the coulomb energy is becomes smaller and the dε level is lowered. In addition, the second nearest neighbor metal ions surrounding an octahedral site (hatched circles in Fig. 2.11) are arranged symmetrically about the trigonal axis (the 111 axis in the same Fig. 2.11) so that they produce a trigonal field which tends to attract the electrons along the trigonal axis. In consequence the triply degenerate dε levels are splitted into an isolated lower single level, which corresponds to the wave function stretching along the trigonal axis and the doubly degenerate higher levels which correspond to the wave functions stretching perpendicular to the trigonal axis.

In Fe^{3+} without crystal field, the sum of the five wave functions is symmetrical, leading to no magnetic crystalline anisotropy. On the other hand, Fe^{3+} under crystal magnetic field shows spatially asymmetric wave function, leading to the magnetic crystalline anisotropy.

The magnetic anisotropy is used for description of the dependence of the internal energy on the direction of spontaneous magnetization. This kind of energy is called magnetic anisotropy energy and the magnetic anisotropy energy term has the same symmetry as the crystal structure of the material. So, it is called a magnet crystalline anisotropy.

The difference of the area between the two magnetization loops (M-H curve) in which magnetic field is applied perpendicular to and in plane of the sample plane,

corresponds to the anisotropy energy. The equation (2.5) shows the magnetic anisotropy energy.

$$E_a = \int M_\perp \, dH - \int M_\parallel \, dH \qquad (2.5)$$

E_a is anisotropy energy, H is applied magnetic field and $M_\parallel$ and $M_\perp$ are the magnetization. For example, Fig. 2.13 shows the difference of area between perpendicular and in-plane magnetization curve (anisotropy energy) of Bi:GdIG on GGG substrate.
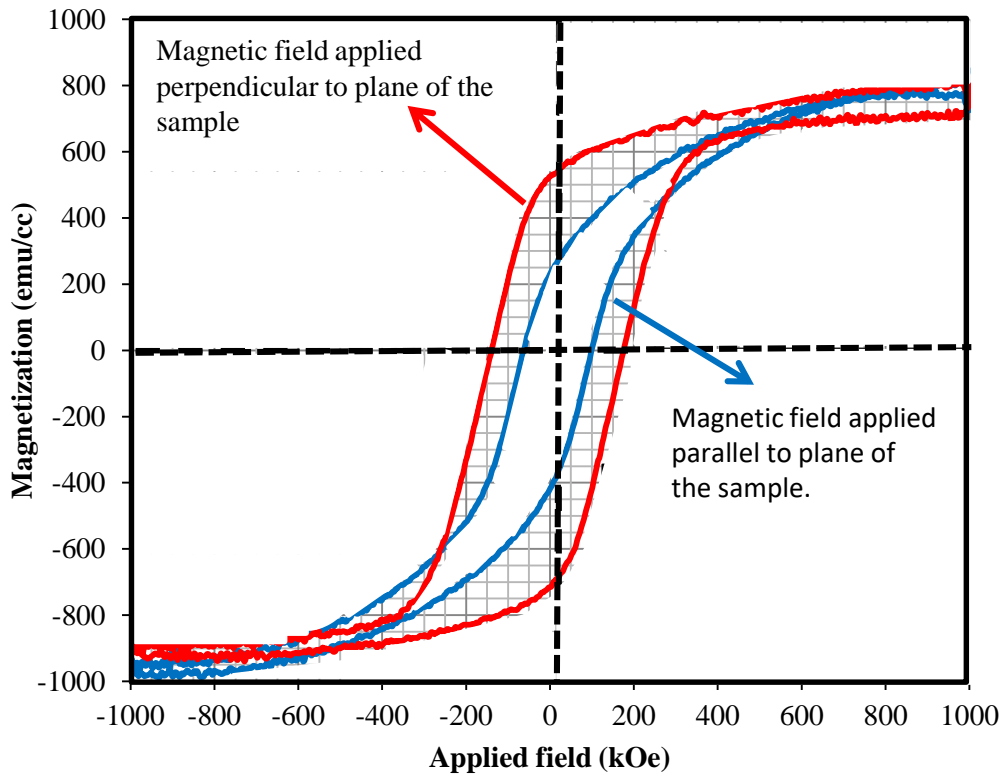
Fig. 2.13 The area between the perpendicular magnetization (red curve) and in-plane magnetization (blue curve) shows the anisotropy energy of Bi:GdIG on GGG sub.

2.6 Gadolinium iron garnet

Gadolinium iron garnet ($Gd_3Fe_5O_{12}$) belongs to the family of ferrimagnetic rare-earth garnets which are assigned to cubic structure with every cell containing eight $R_3Fe_5O_{12}$ molecules. The magnetic properties of bulk GdIG have been widely studied since the 60's of the last century including temperature dependence of magnetization, differential susceptibility in applied fields, magnetic anisotropy and other properties are discovered [10-14]. Fig. 2.14 shows the temperature variation of effective anisotropy constant (K_1) in GdIG by G. P. Rodrigue [13]. Fig. 2.15 shows the value of susceptibilities of GdIG (χ) by W. P. Wolf and Pauthenet [14].
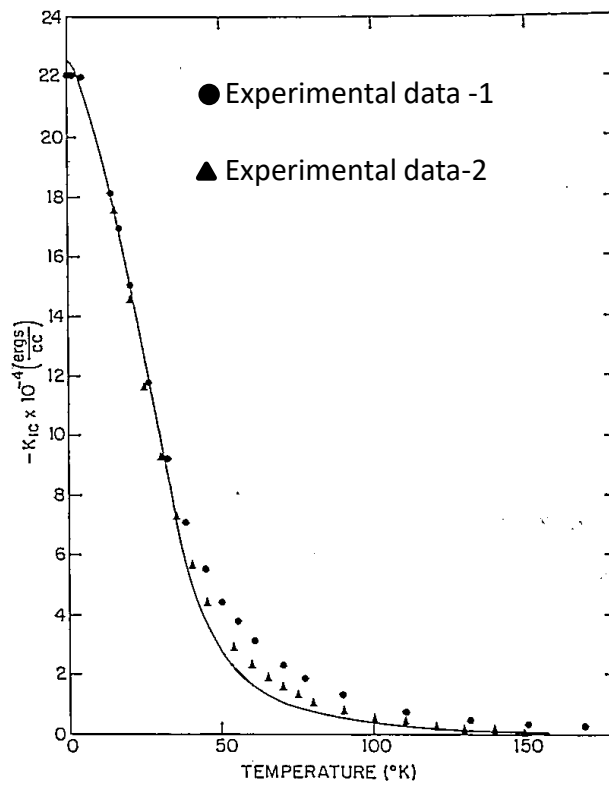
Fig. 2.14 Temperature variation of effective anisotropy constant K_1 in GdIG [13].
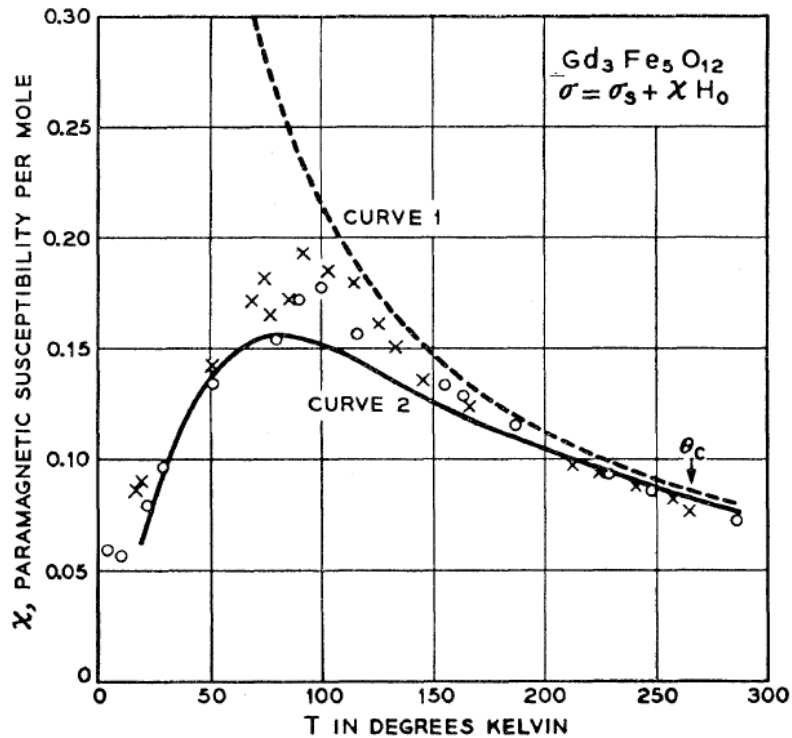
Fig. 2.15 Experimental paramagnetic susceptibilities of GdIG obtained by Pauthenet (crosses), by Wolf (circles). Curve 1 was fitted by Pauthenet, and Curve 2 was fitted by Wolf [14].

Rare-earth ion R^{3+} can only occupy dodecahedral sites which have larger space and cannot occupy the octahedral and tetrahedral sites because of its large ion radius. the iron oxide (Fe^{3+}) occupies three tetrahedral (D) sites and two octahedral [A] sites, 96 oxygen ions surround the 3 sites with coordination number of 4, 6 and 8, respectively. The Fe^{3+} ions in the octahedral sites and tetrahedral sites have opposite magnetization directions. There are strong exchange interactions between Fe^{3+} ions located at two sites and the net magnetization is parallel to the magnetic moment of Fe^{3+} in the tetrahedral site. These strong super exchange interactions between two magnetic ion sub-lattices decide the magnitude of the Curie temperature. The magnetic sub-lattice of the Gd^{3+} ions is polarized by the iron sub-lattices and becomes magnetically oriented antiparallel

to the resultant iron ion (tetrahedral direction) sub-lattice magnetization. In GdIG, the exchange field between the Fe^{3+} and Gd^{3+} sub-lattices is much weaker than that between the two iron sub-lattices. The interaction between the Gd^{3+} ions is very weak and the Gd^{3+} sub-lattice can be considered to be essentially a system of paramagnetic ions situated in an exchange field created by the Fe^{3+} sub-lattices. Due to the difference in the temperature dependence of the magnetization of the iron and the rare-earth sub-lattices, the net magnetization of GdIG falls to zero at magnetization compensation temperature T_{comp}. At this temperature, the magnetization of the iron (Fe) and Gadolinium (Gd) sub-lattices have the same magnitude but opposite sign [1]. The compensation temperature of $Gd_3Fe_5O_{12}$ is close to room temperature (286K).

Easy magnetization direction of the GdIG is perpendicular to the sample plane owing to smaller magnetization compared to that of YIG. The Yttrium ions (Y^{3+}) do not have magnetic moment; the total magnetic moment in YIG belongs to exchange interactions between octahedral site and tetrahedral site and net magnetization is parallel to the magnetic moment of Fe^{3+} located at the tetrahedral direction. The easy magnetization axis is in-plane in YIG. In GdIG, the total magnetic moment is smaller and demagnetization field is smaller leading to perpendicular magnetic anisotropy.

2.7 Bismuth substituted rare-earth Iron Garnet (Bi:RIG)

The several rare-earth ions can be substituted to dodecahedral sites; each substitution brings its own special modification in the properties of garnet. By substituting the Bi^{3+} [15], Pb^{2+} [16] and Ce^{3+} [17] to the rare-earth iron garnet, the Faraday rotation increased within certain wavelength intervals and magnetic properties are changed. By increasing the amount of Bi^{3+} in RIG the Faraday rotation increased in

the visible to near infrared range and the crystal has high transparency that make them most frequently used material for magneto optical device [15, 18-21].

It has been reported that the Faraday rotation is increased by increasing the amount of bismuth substitution. The reason for this is enhanced, spin orbit splitting in the excited states caused by formation of hybrid molecular orbits between the 3d orbital in Fe^{3+} and 2p orbital in O^{2-} mixed with the 6p orbital in Bi^{3+}, leading to larger spin orbit interaction coefficient [22-27]. Fig. 2.16 shows the influence of Bi substitution on the Faraday rotation in bismuth substituted YIG [28].
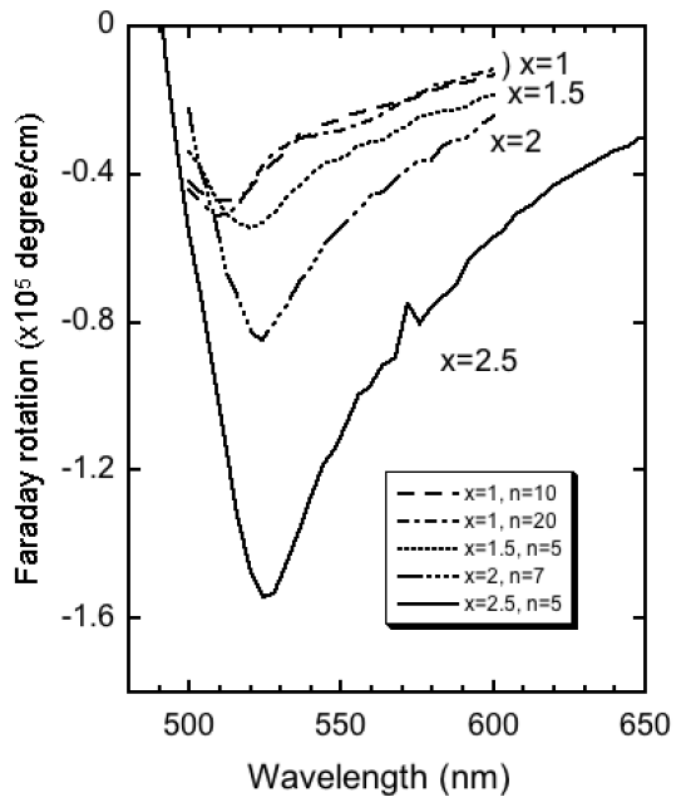
Fig. 2.16 Faraday rotation spectra of Bi:YIG prepared by metal organic decomposition (MOD) method with x = 1.0 - 2.5. *n* indicates a number of coating of MOD solution [28].

CHAPTER
3

Principle of Experiment and characterizations

3.1 Introduction

There are several methods to prepare the bismuth substituted rare-earth iron garnet thin films such as a laser ablation [1-3], a liquid phase epitaxy[4-6], RF magnetron sputtering [7-9], MOCVD [10], pyrolysis [11], crystal ion slicing [12] and sol-gel method [13]. Among them, metal organic decomposition (MOD) method is a promising to prepare magnetic garnet films, because it is a simple fabrication method which is composed of spin coating of the MOD solution and annealing, and guarantees high uniformity in chemical composition and purity combined with chemical stability [14-17]. I have prepared several bismuth substituted gadolinium iron garnet (Bi:GdIG) thin films on (111) Gadolinium gallium garnet (GGG), (111) $(GdCa)_3(GaMgZr)_5O_{12}$ (SGGG) and glass substrates by metal organic decomposition method (MOD).

I characterized my samples by X-ray diffraction (XRD), optical transmittance / reflectivity spectra, magneto optical Faraday effect and magnetization.

In this chapter, I will explain the preparation methods of magnetic garnet thin films. I discuss the comparison among several preparation methods. Furthermore I will

describe the principle of characterizations of the magnetic garnet thin films, such as XRD, optical measurement, Faraday effect and magnetization.

3.2 Preparation of magnetic garnet

3.2.1 Reported preparation methods of magnetic garnet

3.2.1.1 Liquid phase epitaxy method

The liquid phase epitaxy (LPE) method has been applied for growing garnet for the first time in 1968 [18]. Due to high growth rate (0.1-10μm/min) and crystalline perfection owing to this method, it becomes useful when thick layers are required [19]. This has the ability to produce very flat surfaces and excellent structural perfection [20]. The main disadvantage of LPE method is substrate limitation that requires lattice-matched substrate. Furthermore highly Bi doped rare-earth iron garnet cannot be obtained by LPE because ionic radius of Bi^{3+} (1.17Å) is larger than that of Y^{3+} (0.95Å), leading to very large lattice constant expansion. At high temperature, combinatorial entropy becomes energetically favorable making it difficult to substitute Bi for Y because nonequilibrium phase is necessary for full bismuth substitution [21]. Also It is difficult to control the thickness of the film precisely by LPE method, because of the high growth rate (0.1-10 μm/min) [22-23].

3.2.1.2 Pulsed laser deposition method

Pulsed laser deposition (PLD) method uses a high intensity pulsed laser to create plasma, to modify plasma properties, and to transfer the plasma to a substrate surface to create thin films. The pulsed laser deposition technique has been used in some research laboratories to deposit high quality films of materials for more than a decade [21]. The

high power laser pulses are used by this technique to melt, evaporate and ionize material from the surface of a target. The properties of the film are influenced and changed by numbers of variables, such as laser flounce, background gas pressure and substrate temperature [3, 24].

The advantage of the PLD method is the possibility to prepare films with complex composition, relatively high deposition rates, and control of film thicknesses in real time by simply turning the laser on and off. The PLD method has some disadvantages such as the plasma plume and molten droplet created during the laser ablation process, leading to the adherence to the substrate and rough surface. The most important difficulty is to fabricate a large area with uniform film thickness [25].

3.2.1.3 Sputtering deposition

RF-sputtering is used to fabricate thin films on a substrate. A sputtering system consists of a vacuum chamber, an anode (substrate) and a cathode (target). Normally they are faced to each other. The RF electric field between anode and cathode is applied, and accelerates the electrons which approach the outer shell electrons of neutral gas atoms of Ar in their path and, being ionize to Ar^+. At this point the positively charged ions (Ar^+) are accelerated by the electric field towards negatively charged electrode cathode and approaches to the target surface. The impact results in a series of collisions between the incident ions and target atoms, and ejection of one or more atoms from the target material. This phenomenon is called as sputtering. The sputtered atoms or particles will move through space and then condense on the surface of substrate to form films [26].

One of the advantages of sputtering is the thickness control capability. The main drawback of this technique is hard to maintain stoichiometric composition and low deposition rate [24, 26, 27]. Since the amount of FR rotation is highly related to the amount of Bi and composition of magnetic garnet, it is difficult to control precisely the amount of Faraday rotation by controlling the amount of Bi and composition by sputtering deposition method.

3.2.1.4 Metal Organic Decomposition (MOD)

The metal organic decomposition (MOD) method is a simple and easy method for fabrication of magnetic garnet thin films. The process is composed of contain 3 steps, that is spin-coating, drying and annealing. The MOD method requires a spin-coater, hot plate and a furnace, does not require vacuum chambers. The solution is spin-coated in 2 steps process to drop and distribute the solution on the surface of substrate properly (500 rpm for 5 second in this study), and coated in higher rotation speed (2000 rpm for 20 second in this study) for flatness of the surface and control the thickness of the sample, followed by drying on hot plate (120°C for 10 min) for evaporating the solvent, pre-annealing in order to decompose the organic material and obtain amorphous oxide film (550° for 10 min). The spin-coating, drying and pre-annealing are repeated in order to obtain the desired thickness for the film. Finally the film is annealed at higher temperature for crystallization (620-800°C for 2 hours). Since the composition of the MOD solutions can be precisely controlled, we can control the magneto optic and magnetic properties of the garnet films. The spin-coating can be applied over large area. Therefore films can be formed over a large area. Since the metal oxide carboxylates are dissolved in organic solvents, they have a much longer shelf storage life. The MOD

method is based on the metal carboxylates which are stable in liquid and compatible with glass substrates. The MOD method needs a relatively low temperature compared with the melting point of Bi:RIG for crystallization. Therefore by using MOD method, garnet films can be deposited easily on non-crystal glass substrates. The thickness of the sample in MOD depends on the viscosity of solution (viscosity of solution depends on the composition), speed of spin-coating and number of spin-coating. Therefore it is difficult to control the thickness of the sample in the range of d < 10 nm. The magneto optical properties, crystallization and physical properties of the films that are prepared by MOD method are strongly dependent on the types of solution, and fabrication condition.

I used two types of commercial MOD solutions to fabricate bismuth substituted gadolinium iron garnet (Bi:GdIG) thin films. One is MOD solution and the other is EMOD solution. The differences between the MOD and EMOD are as follow.

a) Metal organic decomposition (MOD)

The MOD solution contains 2-3 types of metal oxides carboxylates such as Fe_2O_3, Bi_2O_3 and R_2O_3 (R = rare-earth metal) carboxylates in acetic ester to prepare $Bi_xR_{3-x}Fe_5O_{12}$ thin films. The Bi content x is fixed and we cannot change the value of x to control the composition of the films. The viscosity of the MOD solution depends on their composition. Some MOD solution is sticky leading to thicker thickness per spin-coating time and problems of the thickness control. As follows

1- Difficult to control the thickness of the film (in thinner films)

2- The thicker thickness per spin-coating makes it difficult to be decomposed, and to provide rare-earth iron garnet amorphous during decomposition because of sticky solution.

43

The advantage of the MOD solution is that the surface of the film is very clean and homogeneous owing to the stable solution.

b) Enhanced metal organic decomposition method (EMOD)

EMOD solutions developed by Symetrix Corporation of the United States and Kojundo Chemical Laboratory Ltd [28]. The most advantage of the EMOD solution is that it contains one metal oxide carboxylate in xylene and can be mixed with other EMOD solutions containing other metal oxides. Therefore it is possible to prepare the $Bi_xGd_{3-x}Fe_5O_{12}$ thin films in any proportion of Bi content x, which enables greater degree of freedom and more precise control of composition of thin films. The EMOD solution is water like, where we can control the thickness of the film and the metal oxides decomposition can be processed more easily than MOD solution. The main disadvantage of the EMOD solution is that, some smudge and precipitates may form or viscosity may increase depending on the combinations of mixed material making them unsuitable for some applications. The EMOD liquid used in my experiment were SYM-FE05 containing Fe_2O_3 carboxylates, SYM-BI05 containing Bi_2O_3 carboxylates, and SYM-GD01 containing Gd_2O_3 carboxylates by Kojundo Chemical Laboratory.

Table 3.1 shows the comparisons among LPE, PLD, sputtering and MOD method for thin films fabrication.

Table 3.1 Comparisons of the methods to deposit magnetic garnet thin film. d is stand for the thickness of the film.

Feature	LPE	PLD	sputtering	MOD
Vacuum process	Required	Required	Required	Not Required
High substitution of bismuth	Not possible	Possible	Possible	Possible
Lattice matched substrate	Required	Not required	Not required	Not required
Control of thickness	difficult	fine	Coarse	Difficult in the range of d<10nm
control the stoichiometric composition	controllable	controllable	Difficult	controllable
Fabrication over large area	possible	difficult	possible	possible

3.2.2 Procedure of preparing magnetic garnet thin films by MOD method

Here I explain the procedure of preparing magnetic garnet thin films by the MOD method.

1-   Preparation of MOD solution which contains stoichiometric quantities of the decided metal oxides.

For example in the case of preparation of magnetic garnet thin films, I used MOD solutions with Bi, Gd and Fe carboxylates with chemical composition ratio of $Bi_2O_3:Gd_2O_3:Fe_2O_3 = 1:2:5$ and $2:1:5$ by Kojundo Chemical Laboratory Ltd to fabricate $Bi_1Gd_2Fe_5O_{12}$ and $Bi_2Gd_1Fe_5O_{12}$ thin films. The total concentration of carboxylates in these MOD solutions was fixed at 3 %.

I also used EMOD solutions to prepare the $Bi_xGd_{3-x}Fe_5O_{12}$ thin films with different Bi content x. The EMOD solutions of Fe_2O_3 carboxylates (product name

SYM-FE05), Bi_2O_3 carboxylates (product name SYM-BI05), and Gd_2O_3 carboxylates (product name SYM-GD05), are mixed and combined for different Bi content $x = 1$, 2 and 2.5 and stirred well.

I determined the volumes for each EMOD solution for desired composition ratio as following.

$w/a = 0.5$ mole/ litter (concentration of Bi_2O_3 EMOD solution) ………… … (3.1)

$y/b = 0.1$ mole/ litter (concentration of Gd_2O_3 EMOD solution)……… …….(3.2)

$z/c = 0.5$ mole/ litter   (concentration of Fe_2O_3 EMOD solution)……….....(3.3)

$w{:}y{:}z = x{:}x{-}3{:}5$ (desired stoichiometric composition ratio)…….…………..(3.4)

The values of concentration (molarity) of the solutions are given by Kojundo   Chemical Company. w, y, and z are the molar ratio of Bi_2O_3, Gd_2O_3 and Fe_2O_3. x is the desired amount of Bi substitution in $Bi_xGd_{3-x}Fe_5O_{12}$. a, b and c are the volumes of Bi_2O_3, Gd_2O_3, Fe_2O_3 solution respectively, can be determined as following equations.

From equation (3.4), w and z are expressed as

$w = y (x/x{-}3)$...…………………………………………………...(3.5)

$z = y (5/x{-}3)$ ……………………………………………….…….(3.6)

From (3.1), (3.2) and (3.3) a, b, and c are expressed as

$a = 2w$, $b = 10y$,   and $c = 2z$ ..…………………………………………(3.7)

From (3.5), (3.6) and (3.7)   a, b, and c can be determined

$a = 2y(x/x{-}3)$, $b = 10y$, $c = 2y(5/x{-}3)$……....................................…........(3.8)

$a + b + c = v$ ……..………………………………………………….(3.9)

The v is the total volume of mixed solutions for $Bi_xGd_{3-x}Fe_5O_{12}$. The amount of v is depending to the size and thickness of samples.

From (3.8) and (3.9)

$2y(x/3-x) + 10y + 2y((5/x-3) = v$ …………………………….…..….…(3.10)

Value of y is obtained from (3.10). By substituting y to 3.8 the volumes *a*, *b*, and *c* are determined.

2- The solution was then filtered by advantec filter paper.

3- Cleaning the substrate:

The substrates were cleaned with acetone, propanol and water subsequently in ultra-sonic cleaner.

4- Spin-coating:

The solution was spin-coated in 2 steps process of 500 rpm for 10 second and 2000 rpm for 20 second.

5- Drying

After spin-coating, the samples have been dried on a hot plate at 120°C for 10 min to evaporate the solvent.

6- Pre-annealing

In order to decompose the organic materials and obtain the amorphous metal oxide films without carboxylates, the samples were annealed at 550°C for 10 min (pre-annealing) at atmospheric pressure.

In order to obtain desired thickness, the spin-coating drying and pre-annealing were repeated.

7- Final-annealing

The samples are annealed at higher temperature and longer time (in case of garnet 620-800°C for 2 hours) for crystallization. This process is called "final annealing". The pressure during the annealing was atmospheric pressure. We used two kinds of

annealing gas, (the choice of the gas is different with the purpose) that is clean air (80% N_2 + 20% O_2) and 100% N_2 gas.

Fig. 3.1 and 3.2 show the graph of thermal gravimetric (TG) and differential thermal analysis (DTA) for YIG and GdIG respectively. The mass of carbon decreases sharply with increasing the temperature, and become minimum around 550°C (pre-annealing for decomposition). The maximum evaporation and decomposition are happening in the range of 400 ~ 550°C for both YIG and GdIG [28].
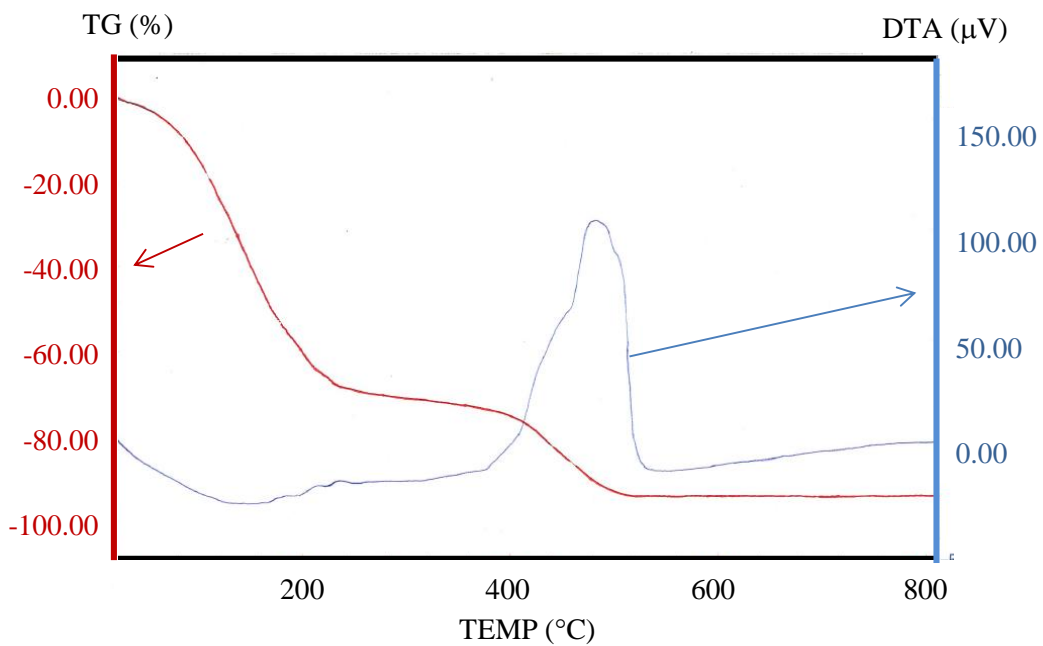

Fig. 3.1 Temperature dependence of thermal gravimetric (red line) and differential thermal analysis (blue line) for $Gd_3Fe_5O_{12}$ MOD solution [28].
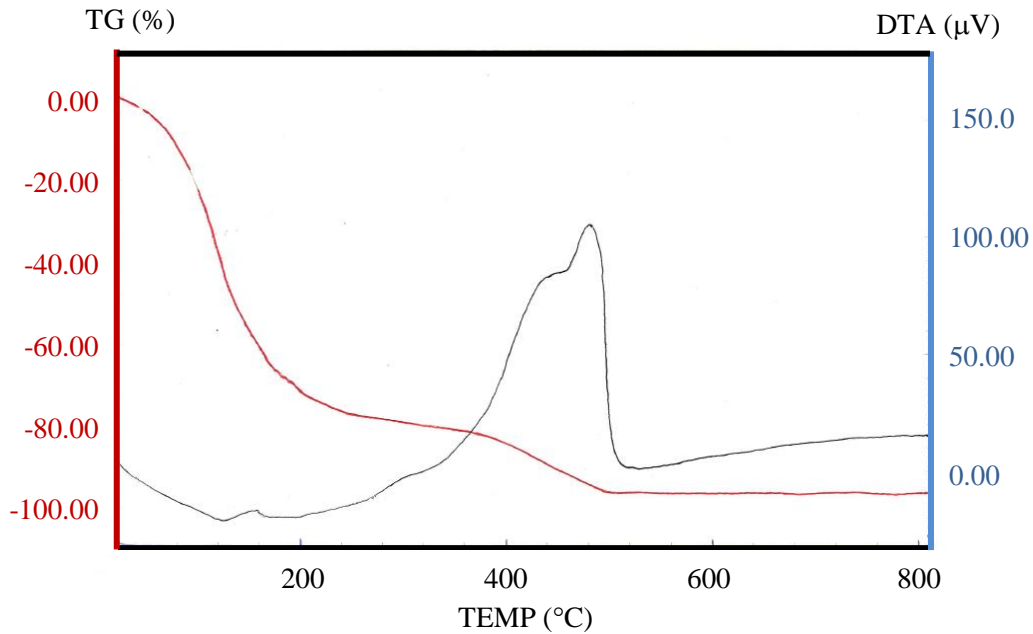
Fig. 3.2 Temperature dependence of thermal gravimetric (red line) and differential thermal analysis (blue line) for $Y_3Fe_5O_{12}$ MOD solution [28].

The different substrates, annealing temperatures and annealing gases were selected in my experiments depending on the purposes. I will discuss in detail in chapter 4, 5 and 6.

There are several reports on fabrication of magnetic garnet thin films by MOD method. $Bi_xGd_{3-x}Fe_5O_{12}$, $Bi_xY_{3-x}Fe_5O_{12}$ (Bi:YIG) and $Bi_xY_{3-x}Ga_yFe_{5-y}O_{12}$ thin films have been fabricated on (111) oriented gadolinium gallium garnet (GGG) single crystal substrates [5,7, 14, 27], and glass substrates [29].

The Polycrystalline $Dy_{1.6}Bi_{1.4}Fe_{5-x}Ga_xO_{12}$ and $Gd_2Bi_1Fe_{5-x}Ga_xO_{12}$ garnet thin films have been deposited on glass substrate by metal organic decomposition (MOD) method for the first time by A. Azevedo, et al. in 1994. The Faraday rotation and ellipticity spectra of 300 nm thick $Dy_{1.6}Bi_{1.4}Fe_{5-x}Ga_xO_{12}$ thin film are shown in Fig. 3.3 [14].

Fig. 3.4 shows Faraday rotation spectra of Bi:YIG thin films with x = 2.5 crystallized at 500 - 750 °C prepared on (111) gadolinium gallium garnet (GGG) single crystal substrates by MOD method [17].
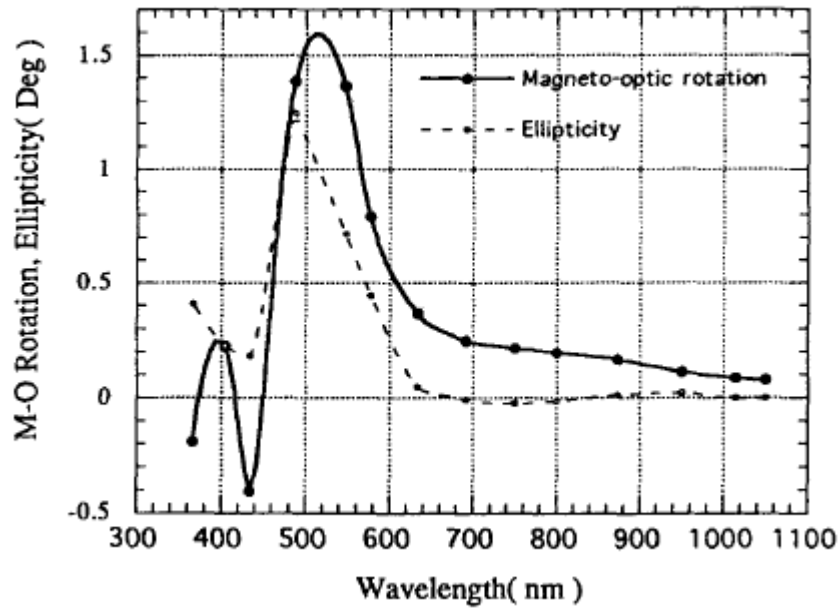
Fig. 3.3 Faraday rotation and ellipticity spectra of 300 nm - thick $Dy_{1.6}Bi_{1.4}Fe_{5-x}Ga_xO_{12}$ thin film on glass substrate [14].
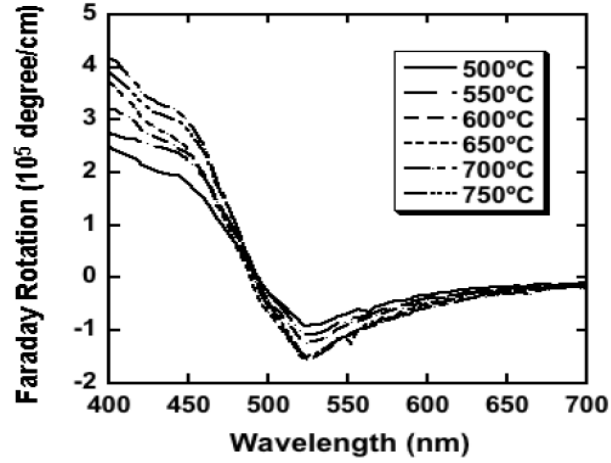
Fig. 3.4 Faraday rotation spectra of Bi:YIG with x = 2.5 prepared on GGG (111) substrate at temperature of 500 -750 ◦C. Thickness of these films are 200 nm [17].

Table 3.2 shows the calculation of composition ratio for mixing EMOD solution and figure 3.5 shows a schematic image of the process and procedure of the MOD method.

Table 3.2. Calculating the volume of EMOD solution with desired amount of Bi (x) for fabricating $Bi_xGd_{3-x}Fe_5O_{12}$.

	Bi_2O_3	Gd_2O_3	Fe_2O_3
mole	w	y	z
Volume	a	b	c
Concentration (Mole/litter)	w/a = 0.5	y/b = 0.1	z/c = 0.5
Stoichiometric composition	x	3-x	5
Molar ratio	w:y:z = x:3-x:5		
v = desired total volume	a+b+c = v		
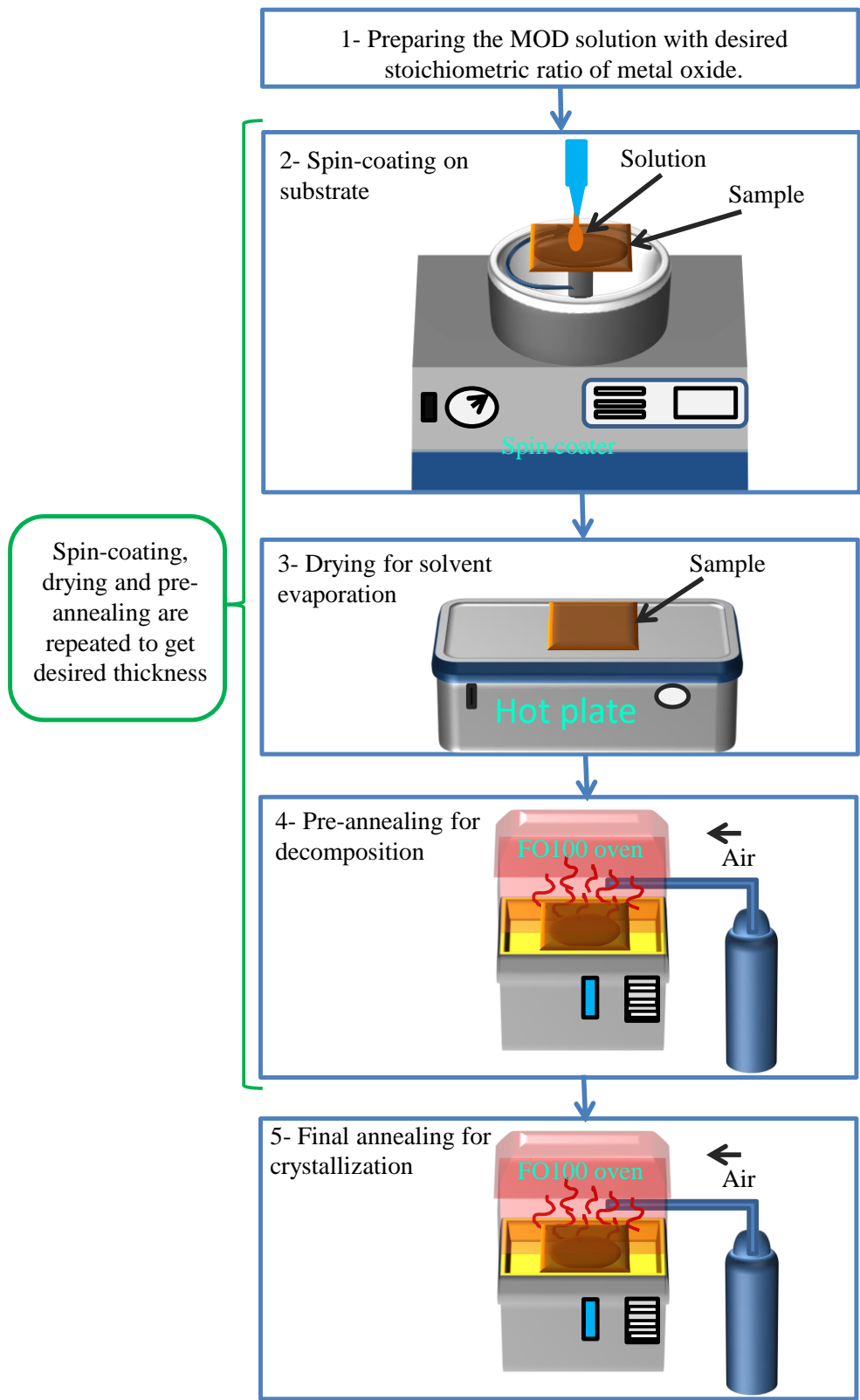
Fig. 3.5 A schematic image of the process flow of the MOD method.

3.3 Principle of characterization of the magnetic garnet thin films

3.3.1 Principle of XRD measurement

We characterized the lattice constant/ crystalline orientation of the magnetic garnet thin films. Therefore, we explain the principle of the X-ray diffraction for this purpose.

3.3.1.1 Bragg's law

Bragg's Law was introduced by W.H. Bragg and his son W.L. Bragg to identify the structures of crystals and molecules using x-ray diffraction studies, which are called as Bragg's Law. The Bragg's law explains the relationship between the x-ray incident angle and its diffraction angle from the crystal surface. Figure 3.6 shows a schematic image of the Bragg's law.

The law states that when the x-ray incidents onto a crystal surface, with the angle of incidence θ, diffracted back with the same angle, θ. And, when the path difference between two X-ray beams (AB+BC) is equal to $n\lambda$, constructive interference occurs, where n is a positive integer, λ is the wavelength of the X-ray beam and d is the lattice spacing. From the Fig. 3.6 we can write the Bragg's law as follow.

$n\lambda = AB + BC \longrightarrow AB = BC \longrightarrow n\lambda = 2AB$

$Sin\,\theta = AB/d \longrightarrow AB = d\,sin\,\theta \longrightarrow n\lambda = 2dsin\theta$

$$\lambda = 2d_{hkl}\,sin\theta_{hkl}$$

- λ = the wavelength of the x-ray
- d_{hkl} = lattice spacing
- θ_{hkl} = the incident angle
- n = positive integer

- *h, k* and *l* are known as Miller indices (*hkl*) and are used to identify each lattice plane.
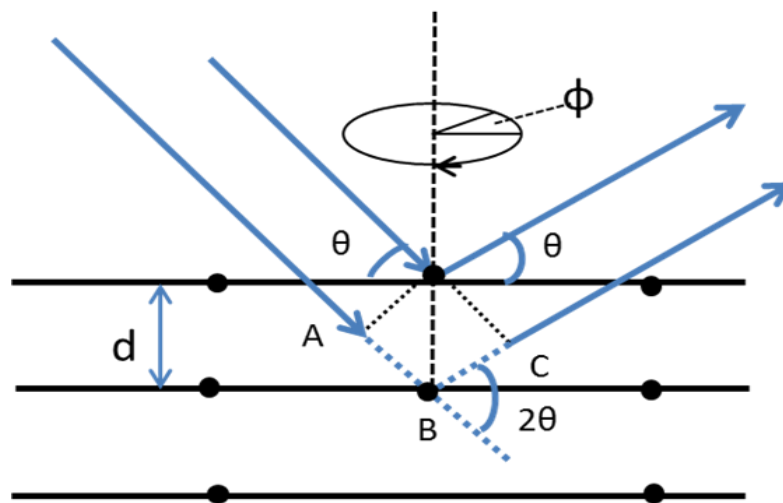
Fig. 3.6 A schematic image of the Bragg's law in X-ray diffraction.

axis	x	y	z
Intercept points	1	1	∞
Reciprocals	1/1	1/1	1/∞
Miller indices	1	1	0
hkl	110		
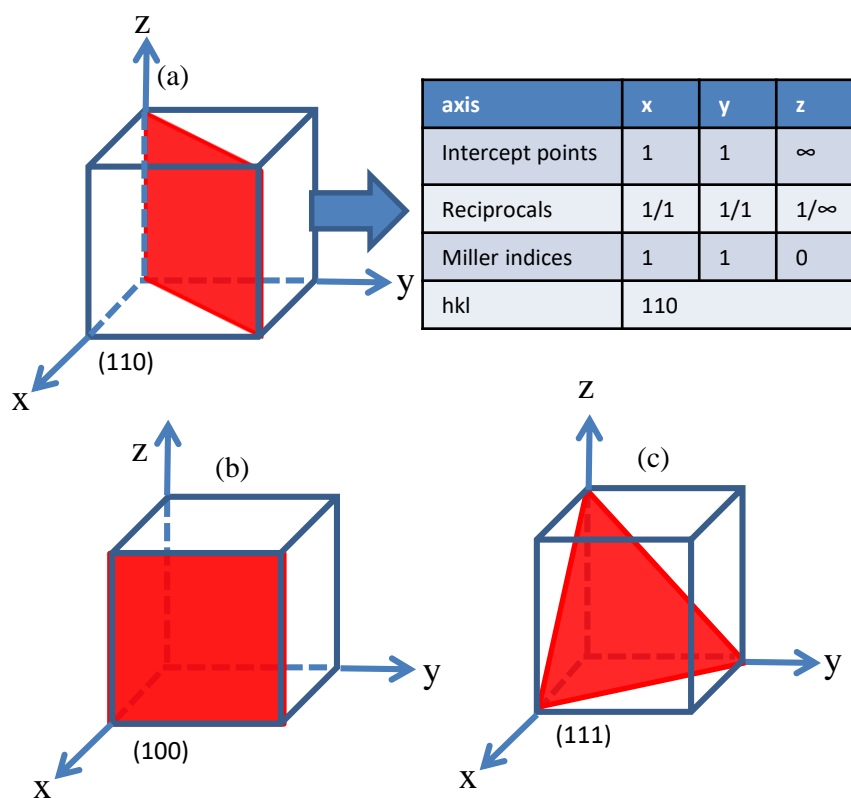
Fig. 3.7 Cubic crystal structures with miller indices (hkl) of (a) 110, (b) 100, and (c) 111.

Figure 3.7 shows an example of lattice planes cut the x, y, and z axis of the unit cells in

(a) 1,1and ∞; (b) 1, ∞ and ∞; (c) 1, 1 and 1 intercepts point. The miller indices (*hkl*) are

(a) (110), (b) (100) and (c) (111).

The relationship between miller indices (*hkl*), lattice spacing d_{hkl} and lattice constants *a*

in cubic system is as follows:

$$\boldsymbol{d_{hkl}} = \frac{a}{\sqrt{h^2+k^2+l^2}}$$

3.3.1.2 Analysis of crystalline structure by X-ray diffractometer

The purpose of X-ray diffraction is to study the crystal structure of thin films and to characterize what kinds of compounds are included in the films. I used the XRD for identification of the phase and crystalline orientation included in the magnetic garnet samples.

I used x'pert PRO x-ray diffractometer system by Philips Co., ltd to measure the x-ray diffraction (XRD) spectra of the fabricated samples. This instrument uses X-ray radiation by Cu-kα with the wavelength of $\lambda = 1.5405980$ Å for the $K_{\alpha1}$ line, $\lambda = 1.54439$ Å for the $K_{\alpha2}$, with line long fine focus window 12 mm x 0.4mm dimensions and working power of 45 kV/40 mA.

Fig. 3.8 shows the pictures of the XRD machine used in this study. After the X-rays are generated by a x-ray tube, the divergent x-ray beam from a line focus tube will convert to a quasi-parallel beam with a pure $K_{\alpha1}$ by Hybrid monochromator or intense quasi-parallel beam with K_{α} radiation by x-ray mirror. After controlling and reducing the intensity of these rays by automatic beam attenuator (filter), the beam is incident toward the sample on the sample stage. When the Bragg's Law, *$n\lambda = 2d \sin \theta$,* is satisfied, the interaction of the incident rays with the sample produces the strong diffracted ray by the constructive interference. The diffracted rays become parallel by collimator and can be detected. The detector counts the intensity of the diffracted beam at certain *2θ* position. As the sample and detector are rotated, the intensity of the diffracted X-rays is recorded by the detector, and then the recorded X-ray signals are saved in the PC. The rotation of the sample is in the path of the collimated X-ray beam at an angle θ, while the X-ray detector collects the diffracted X-rays, with the angle of 2θ. By scanning the sample through a range of 2θ, all possible diffraction peaks from

single phase or multiple phases of the lattice planes can be attained in a specific 2θ angle. The parameter *d* of the lattice plane can be achieved from attained 2θ. Then the value of *d* can be used to identify the materials and their crystals specifications because each material has a set of unique lattice spacing. By comparing the lattice constant of two materials, I estimated the composition of our single crystal films. Also the diffraction peaks associated with different phases of the polycrystalline or single crystalline can be confirmed by comparing *d* of the lattice planes with the powder diffraction file of international center for diffraction data (ICDD) to identify and estimate the crystal structure.
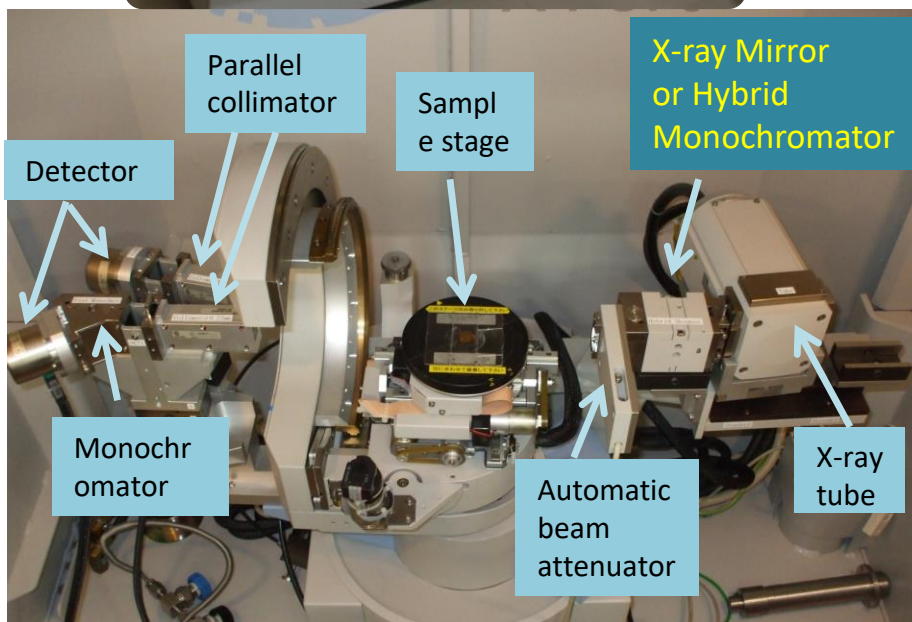
Fig. 3.8 X'pert PRO x-ray diffractometer system PHILIPS.

3.3.2 Principle of the characterization of Magneto Optical Faraday effect

Michael Faraday observed the effects of interaction between light and magnetic field in a medium for the first time in 1845, that known as the magneto optical Faraday effect or Faraday rotation. The Faraday rotation describes the rotation of the plane of polarization of a linearly polarized light. When the plane-polarized light passes through an optically transparent (or semi-transparent) medium with an applied magnetic field along the direction of light propagation, the plane of polarization is changed. The amount of Faraday rotation angle (θ) is described by the following formula.

$$\theta = VHL \tag{3.11}$$

Where the L is the distance (thickness of the sample) traversed by light in a medium along the direction of the applied field (H) and the V called the Verdet constant depends to the properties of the medium, the frequency of light, and the temperature of sample. The sign of the rotation angle θ depends on the sign of the magnetic field H. Therefore if the light travels twice through the sample under a magnetic field (first along the field direction, and then after normal reflection by a mirror in the opposite direction of the magnetic field) the total rotation angle is twice as large as θ.

1- This is a basic principle of free space optical isolators and MOSLMs, composed of a Faraday rotators ($\theta = 45°$) and two linear polarizers (0° and 45°) as shown in Fig. 1.1.

2- This is a unique property of magnetic materials.

3.3.2.1 Phenomena of Faraday Effect

The magneto optical Faraday effect or Faraday rotation is based on the interaction between light and magnetization in a medium. The Faraday effect is caused by the difference of propagating speed between the left and right circularly polarized light in a medium as schematically shown in Fig. 3.9 and Fig. 3.10. This property is known as circular birefringence and is due to the splitting of the energy levels of electrons in atoms or molecules under a magnetic field. The quantum transitions between the levels require the emission and absorption of the right and left circularly polarized light parallel with the applied magnetic field, in the case of parallel propagation, the original level may be regarded as being split into just two sublevels. As a result the refractive indices and absorption coefficients, which are dependent on the wavelength or frequency of the light, become different for the right circularly polarized light (RCP) and left circularly polarized light (LCP). The difference in the phase velocities is due to the difference in the wavelengths or frequencies of the light that is absorbed and reemitted by the particles of the substance. The selection rules for light-induced quantum transitions show that LCP and RCP induce different electronic transition, hence different refractive indices when magnetic field is applied. In non-magnetic materials at magnetic field H=0, LCP and RCP obey equal transition process and consequently no FR occur.

The level splitting can be caused by electron-electron interactions, spin-orbit coupling, crystal field splitting, exchange interaction, and the Zeeman effect. Under these circumstances, there are two possible transition types: paramagnetic and diamagnetic [34, 35] which are showed in Fig. 3.11.
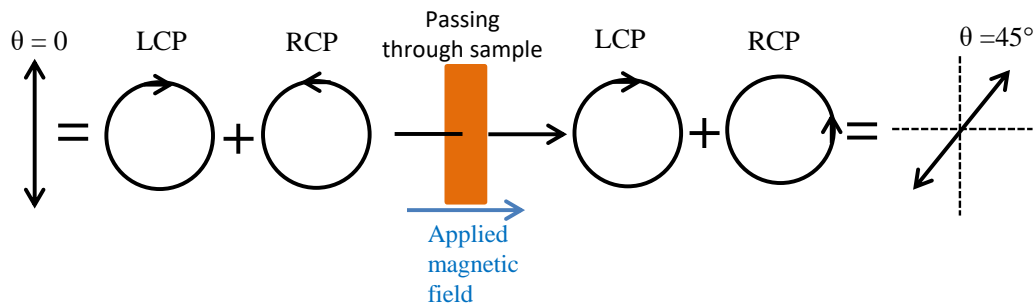
Fig. 3.9 A schematic image of the Difference of refractive index for RCP and LCP leads to different phase velocities of RCP and LCP, leading to that the polarization of linearly polarized light is rotated.

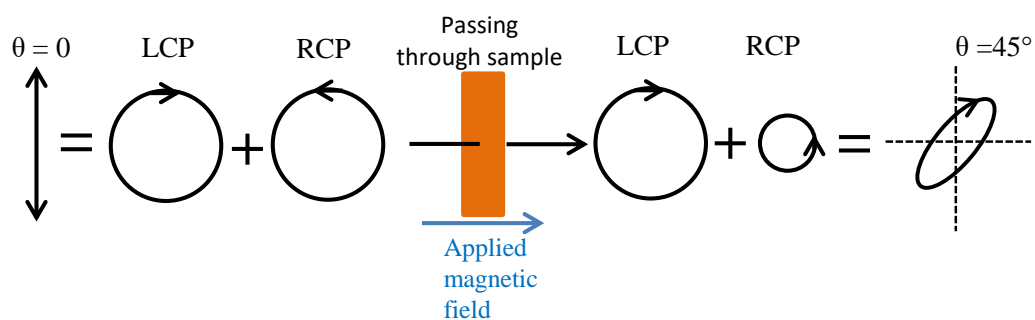Fig. 3.10 A schematic image of the difference of absorption indices for RCP and LCP leading to difference phases amplitude leading to magnetic circular dichroism or Faraday ellipticity.
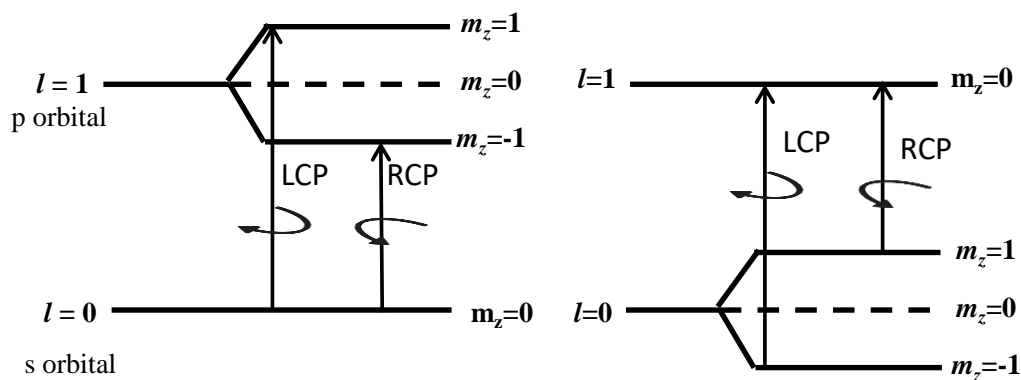

Fig. 3.11 A schematic image of diamagnetic and paramagnetic transitions. LCP and RCP represent left- and right-circularly polarized light.

l is orbital angular momentum quantum number, m_z is the magnetic quantum number.

3.3.2.2 Magneto-optic Faraday effect and the dielectric tensor in YIG

The propagation of electromagnetic waves in a material with a cubic geometry like YIG and magnetization parallel to the z axis can be described by the dielectric tensor ε and magnetic permeability μ, where in optical frequencies μ can be taken equal to unity and ε can be expressed as following equation.

$$\hat{\epsilon} = \begin{pmatrix} \epsilon_0 & i\epsilon_1 & 0 \\ -i\epsilon_1 & \epsilon_0 & 0 \\ 0 & 0 & \epsilon_z \end{pmatrix} \tag{3.12}$$

The all element have real and imaginary part:

$$\epsilon_j = \varepsilon_j' + i\epsilon_j'' \tag{3.13}$$

The diagonal element ε_0 is related to the normal refractive index n and the normal extinction coefficient k can be shown by

$$\epsilon_0' = n^2 - k^2 \tag{3.14}$$

$$\epsilon_0'' = 2nk \tag{3.15}$$

The off-diagonal element ε_i is related to the refractive indices $n_{\pm}$ and absorption indices $k_{\pm}$ for right and left circularly polarized light, RCP and LCP.

$$(n_+ - n_-) + i(k_+ - k_-) = \frac{\epsilon_1}{\sqrt{\epsilon_0}} \tag{3.16}$$

The Faraday rotation θ_f is half of the phase difference between the LCP and RCP.

$$\theta_f = = \frac{\pi(n_+ - n_-)}{\lambda} = Re(\frac{\pi\epsilon_1}{\lambda\sqrt{\epsilon_0}}) \tag{3.17}$$

The Faraday ellipticity (η_f) is the difference in absorption of the RCP and LCP waves:

$$\eta_f = = \frac{\pi(k_+ - k_-)}{\lambda} = Im(\frac{\pi\epsilon_1}{\lambda\sqrt{\epsilon_0}}) \tag{3.18}$$

Fig. 3.12 shows the spectra of ε_0 of $Bi_xY_{3-x}Fe_5O_{12}$ [36]. The two broad maxima optical transitions corresponding to 2.8 and 3.4 eV are observed.

Fig. 3.13 shows the extinction coefficient k (absorption) spectra of the $Bi_xY_{3-x}Fe_5O_{12}$ thin films. The two absorption maxima exist near 2.8 and 3.4 eV. Furthermore the absorption increases noticeably with increasing the bismuth substitution [36].
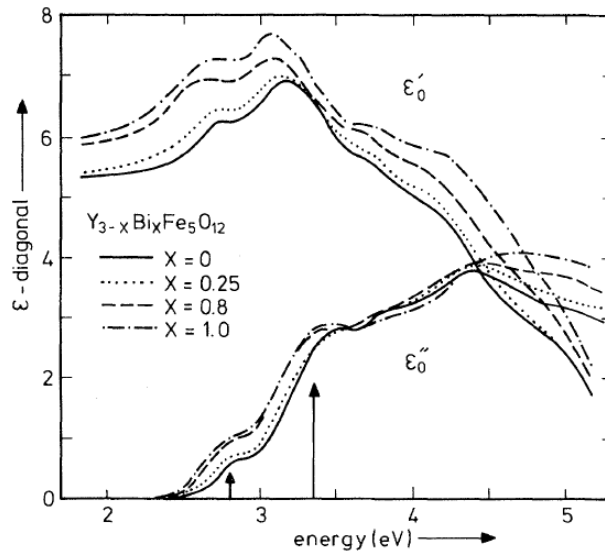
Fig. 3.12 Diagonal elements ε_0' and ε_0'' of the dielectric tensor of $Bi_xY_{3-x}Fe_5O_{12}$ thin films fabricated by LPE method [36].
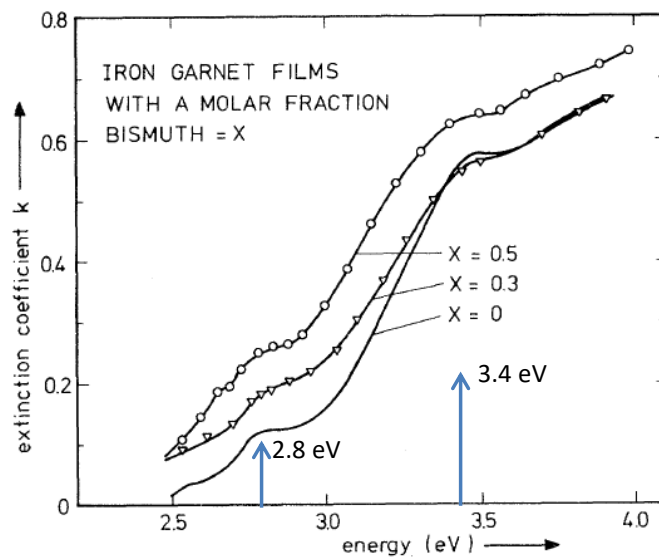
Fig. 3.113 Extinction coefficient k versus photon energy for $Bi_xY_{3-x}Fe_5O_{12}$ thin films fabricated by LPE method [36].

Fig. 3.14 shows the schematic diagram for energy level of oxygen and iron in tetrahedral site (t_{2g}) and octahedral site (e_g) in YIG. There are two types of transitions; the charge transfer transition of an electron from oxygen to iron ($Fe^{3+} + O^{2-} \rightarrow Fe^{2+} + O^-$) and the transition of an electron from one iron ion to another iron ($2Fe^{3+} \rightarrow Fe^{2+} + Fe^{4+}$). The energy gap between the valence band of O^{2-} and Fe^{2+}_{oct} (t_{2g}) is 2.8 eV, and energy gap between the valence band of O^{2-} and Fe^{2+}_{tetra} (e) is 3.4 eV [34, 36].

Fig. 3.14 Schematic diagram of the energy-level for O_2 and Fe (oct and tetr) in iron garnets. Solid arrows (I_a, II_a) denote the lowest oxygen-to-iron charge transfer transitions. Dashed arrows (I_b, II_b) indicate the lowest intervalence transitions within an Fe^{3+} (oct) and Fe^{3+} (tetra) pair [36].

It is considered that the optical transitions at 2. 8 eV (I) and 3.4 eV (II) (Fig. 3.14) are mainly responsible for the remarkable increase of the Faraday rotation in $Bi_xY_{3-x}Fe_5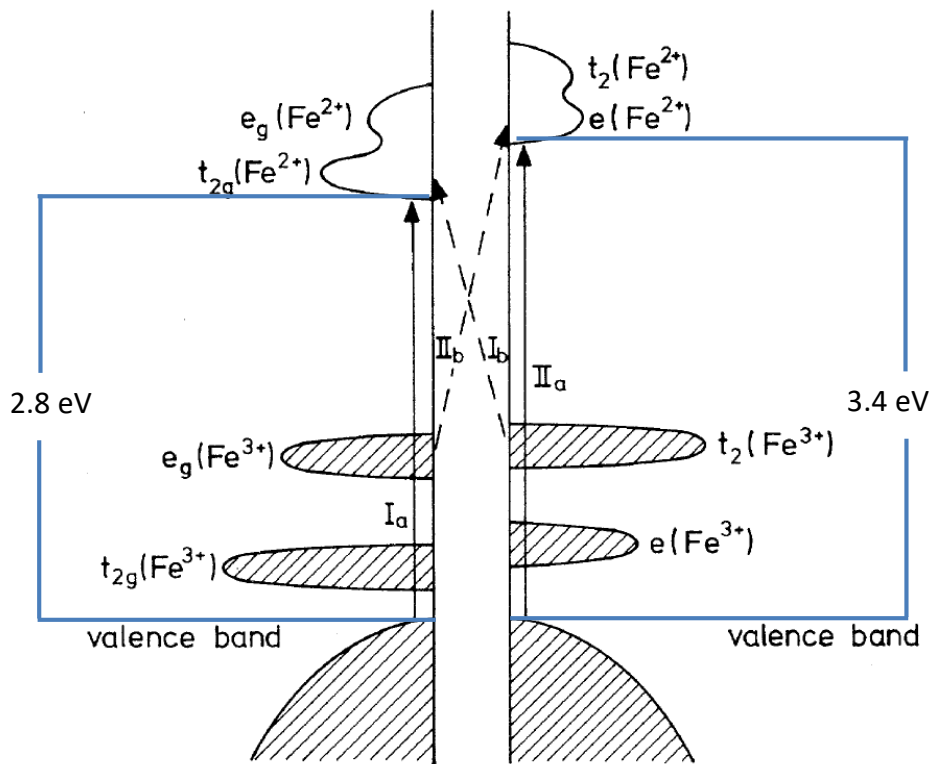O_{12}$ in the visible and near infrared region [35, 36]. Fig. 3.15 shows that, with increasing the amount of Bismuth in $Bi_xY_{3-x}Fe_5O_{12}$ thin films, the FR is increased. The origin for the increase of FR belongs to high spin-orbit coupling of 6p orbital of bismuth (Bi^{3+}) ion and 2p orbital of oxygen (O^{2-}) ion, and 3d orbital of iron Fe^{3+} ion. A noticeable covalent mixing of oxygen 2p orbitals and bismuth 6p orbitals occur due to the large electronegativity of Bi^{3+} ion. And the charge transfer transitions from oxygen 2p orbitals to iron 3d orbitals are most effectively affected by the electronic character of Bi^{3+}. Therefore, by increasing the Bi substitution in $Bi_xY_{3-x}Fe_5O_{12}$ the spin-orbit coupling interaction of the mixed (oxygen-iron) increases, leading to the increase of FR rotation.
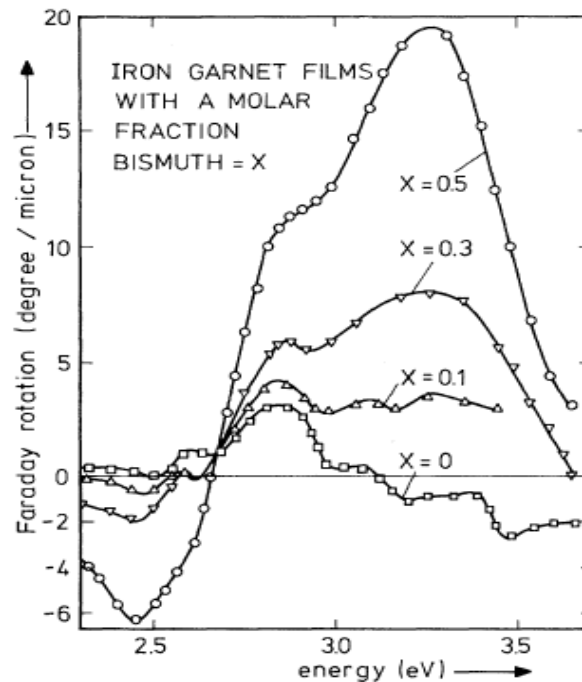
Fig. 3.15 Faraday rotation spectra of $Bi_xY_{3-x}Fe_5O_{12}$ thin film prepared by LPE method [36].

3.3.2.3 Principle of the Faraday effect measurement by polarization modulation technique

Here in this section I will explain the principle of the measurement of the Faraday rotation by the polarization modulation technique. The polarization modulation technique was proposed by K. Sato [37]. Fig. 3.16 shows the schematic image of the principle of this technique. The z axis is parallel to the direction of the propagating light.
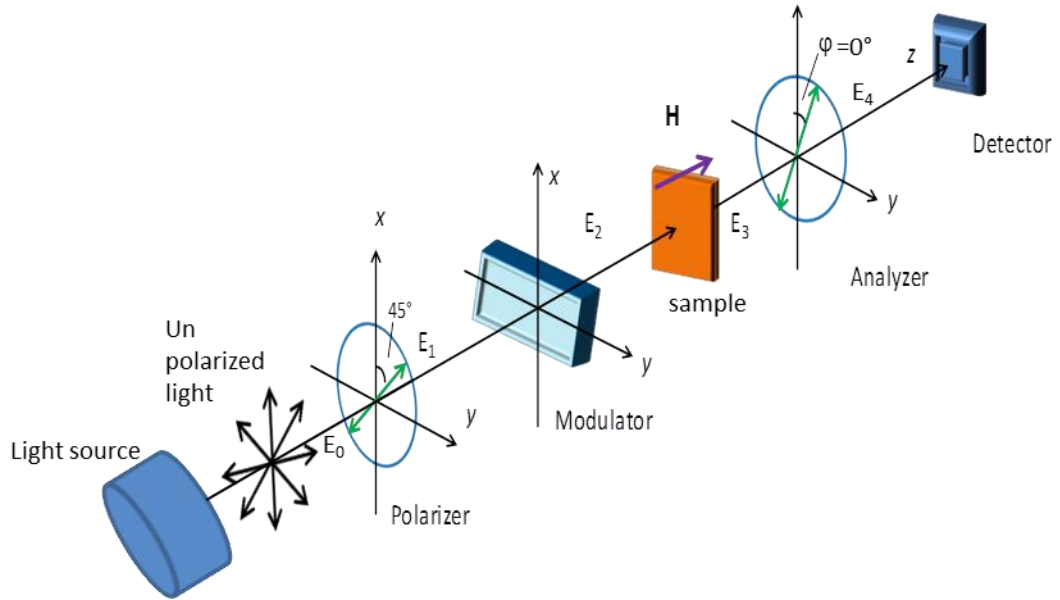
Fig. 3.16 Schematic diagram of polarization modulation technique for magneto optical Faraday effect measurements.

1- We put a polarizer after the light source with the angle of 45° with respect to x axis. The electric field (E_1) of the light after transmitting through polarizer can be expressed as

$$E_1 = \frac{E_0}{\sqrt{2}} \hat{x} + \frac{E_0}{\sqrt{2}} \hat{y} \qquad (3.19)$$

Where E_0 is the amplitude of electric field vector passing throgh polarizer, $\hat{x}$ and $\hat{y}$ denote the unit vectors for the x and y directions respectively.

2-   In the second step the polarized lighte (E_1) is modulated by a photoelestic modulator (PEM). The PEM is a phase modulator by using a crystal having piezoelectric effect. Its principle of operation is based on the photoelastic effect, in which a mechanically stressed element exhibits birefringence which is proportional to the resulting strain. The PEM producing oscillating birefringence at a fixed frequency p of ultrasound range (our system is working on p = $42\ kHz$). The amplitude of the birefringence is controlled electronically by the PEM controller. When the light passed through PEM, it receives a periodically varying opical retardation between x and y directions,   which   is   described   by $\delta = \delta_0 \sin 2\pi pt$. Where δ_0 is the amplitude of the retardation and p is the modulation frequency. The electric field (E_2) of the light after transmitting through the PEM can be expressed as following equation.

$$E_2 = \frac{E_0}{\sqrt{2}}\hat{x} + \frac{E_0}{\sqrt{2}}e^{i\delta}\hat{y}$$
(3.20)

3-   When the light is passing through a sample which is placed in electromagnetic field, the difference of the complex refractive index between the left and right circularly polarized light brings the modulation on the phase between two circularly polarized light, and the transmitted light (E_3) can be expressed as

$$\mathbf{E_3} = \frac{E_0}{2}\left\{\frac{1-ie^{i\delta}}{\sqrt{2}}\begin{pmatrix}1\\i\end{pmatrix}T_+ + \frac{1+ie^{i\delta}}{\sqrt{2}}\begin{pmatrix}1\\-i\end{pmatrix}T_-\right\}$$
$$= \frac{E_0}{2\sqrt{2}}\begin{pmatrix}T_+\left(1-ie^{i\delta}\right)+T_-\left(1+ie^{i\delta}\right)\\iT_+\left(1-ie^{i\delta}\right)-iT_-\left(1+ie^{i\delta}\right)\end{pmatrix}$$
(3.21)

where the values of T_ and T_+ are optical transmissivity for the left and right cirrcularly polarized light.

$$T_- = \exp i(n_- + i\kappa_-)k_0 d$$
$$= \exp(-\kappa_- k_0 d) \cdot \exp i(n_- k_0 d)$$
(3.22)

$$T_+ = \exp i(n_+ + i\kappa_+)k_0 d$$
$$= \exp(-\kappa_+ k_0 d) \cdot \exp i(n_+ k_0 d)$$
(3.23)

Where the k_0 is the wavenumber, d is the thickness of the sample, $n_\pm$ are the refractive indices and $k_\pm$ are the absorption indices of the sample for the right and left circularly polarized light.

4- When the light E_4 is transmitted through the analyzer (angle = 0°) and the x component of the light was exppessed as following equation.

$$\mathbf{E_4} = \begin{pmatrix} 1 & 0 \\ 0 & 0 \end{pmatrix} \mathbf{E_3} = \frac{E_0}{2\sqrt{2}} \{T_+(1 - ie^{i\delta}) + T_-(1 + ie^{i\delta})\}\hat{\mathbf{x}} = \frac{E_0}{2\sqrt{2}} \{(T_+ + T_-) - ie^{i\delta}(T_+ - T_-)\}\hat{\mathbf{x}}$$ (3.24)

The intensity of the light was detected and expressed as

$$I = |E_4|^2 = \frac{E_0^2}{4} \{T + \frac{\Delta T}{2} \sin\delta + T\sin(2\Delta\theta)\cos\delta$$ (3.25)

Where transmission coeffieient of intensity T, ΔT and Δθ are defined as

$$T = \frac{1}{2}(T_+^2 + T_-^2)$$

$$\Delta T = T_+^2 - T_-^2$$
(3.26)

$$\Delta\theta = (n_+ - n_-)k_0 d = \theta_+ - \theta_-$$
(3.27)

The relationship of the Faraday rotation ϕ_F, Faraday ellipticity η_f and complex refractive index can be expressed as following.

$$\phi_F = \frac{1}{2}\Delta\theta = -\frac{1}{2}(n_+ - n_-)k_0 d \qquad (3.28)$$

$$\eta_F = \frac{1}{4}(\frac{\Delta T}{T}) = -\frac{1}{2}(k_+ - k_-)k_0 d \qquad (3.29)$$

By applying $\delta = \delta_0 \sin 2\pi pt$ to equation (3.25) and using expansion formula, like

$$\sin(\delta_0 \sin 2\pi pt) = 2J_1(\delta_0)\sin 2\pi pt + \dots, \cos(\delta_0 \sin 2\pi pt) = $$
$$J_0(\delta_0) + 2J_2(\delta_0)\sin 4\pi pt + \dots, \qquad (3.30)$$

where $J_n(x)$ is an nth order Bessel function

We obtain the output light intensity I, as follows.

$$I = I(0) + I(p)\sin 2\pi pt + I(2p)\sin 4\pi pt + \dots, \qquad (3.31)$$

where

$$I(0) = I_0 T\{1 + J_0(\delta_0)\sin(\Delta\theta + 2\phi)\}$$
$$I(p) = I_0 \Delta T J_1(\delta_0) \qquad (3.32)$$
$$I(2p) = 2I_0 T J_2(\delta_0)\sin(\Delta\theta + 2\phi)$$

The output intensity consists of three frequency components I_1 ($dc_{(p=0)}$), I_2 (p) and I_3 (2p) components and con be detected by lock-in amplifiers for frequencies of dc , p and 2p respectively as shown in figure 3.12 and can be expressed as following equations.

$$I_1 = q_1 I_0 T\{1 + J_0(\delta_0)\sin(\Delta\theta + 2\phi)\} \qquad (3.33)$$

$$I_2 = q_2 I_0 \Delta T J_1(\delta_0) \qquad (3.34)$$

$$I_3 = 2q_3 I_0 T J_2(\delta_0)\sin(\Delta\theta + 2\phi)\} \qquad (3.35)$$

We get the output from system as,

$$\frac{I_2}{I_1} = A\frac{J_1\delta(0)\Delta T/T}{1+J_0(\delta 0)\sin(2\Delta\theta)}$$ (3.36)

$$\frac{I_3}{I_1} = B\frac{2J_2(\delta_0)\sin(2\Delta\theta)}{1+J_0(\delta_0)\sin(2\Delta\theta)}$$ (3.37)

Where A is q_2/q_1 and B is q_3/q_1

When we adjust the value of $\delta_0 = 2.4048$ radian

$$J_0(\delta_0 = 2.4048) becomes 0$$ (3.38)

Then we have simpler forms as

$$\frac{I_2}{I_1} = AJ_1(2.4048)\Delta T/T$$ (3.39)

$$\frac{I_3}{I_1} = 2BJ_2(2.4048)\sin(2\Delta\theta)$$ (3.40)

The value of $\Delta T/T$ and $\Delta\theta$ can be determined from the equation (3.39) and (3.40). By applying the value of $\Delta T/T$ and $\Delta\theta$ to equation 3.28 and 3.29 we can determine the value of Faraday rotation (ϕ_f) and Faraday ellipticity (η_f).

Fig. 3.17 Shows a schematic descriptions of the detected transmitted light for the frequencies at the p and $2p$ that represents the magneto optical Faraday ellipticity and Faraday rotation.

Curve (a) shows the time dependence of the retardation produced by the PEM modulator.

Curve (b) shows the vector loci of the electric field E_3 and the variation of the polarization state (LP-RCP-LP-LCP-LP) in one period of time. In this case, the sample

causes neither Faraday rotation nor circular dichroism. The x component of E_3 remains

constant as shown in curve (c). When there is some difference between phase shifts for

RCP and LCP, the Faraday rotation exists, and the plane of the linearly polarized light

rotates, while the vector loci for circularly polarized light remain unchanged. The x

component of E_3 changes as shown in curve (e). On the other hand, when the magnetic

circular dichroism is present, the vector lengths for RCP and LCP become different as

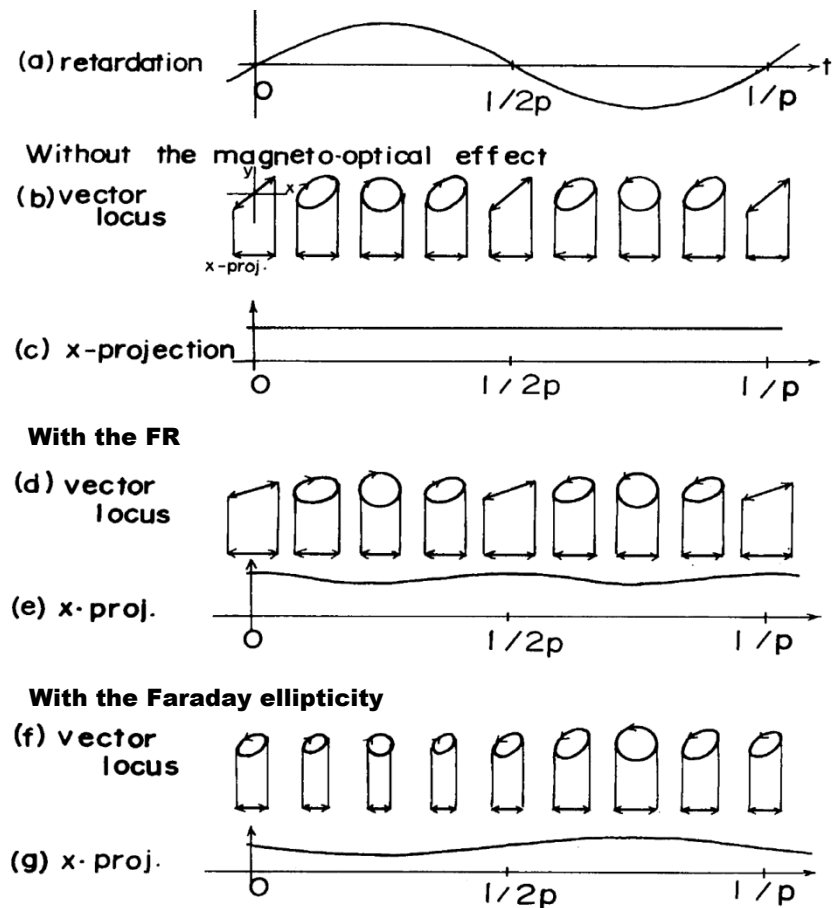illustrated in (f), resulting in the appearance of a frequency with p as shown in curve (g).

Fig. 3.17 A schematic illustration of frequencies of p and 2p components of the output
light intensity that represents Faraday ellipticity and Faraday rotation [37].

3.3.2.4 Measurement of Faraday rotation

Fig. 3.18 shows the overall diagram of polarization modulation system for Faraday rotation measurement in this study. The light from halogen lamp (XENOPHOT HLX-646632) is modulated with a frequency of 280 Hz by a chopper (SR540). The frequency of the chopper is used as a reference signal for lock-in amplifier-1 to detect the transmitted light intensity. Then the light is filtered by color filter in a specific wavelength ranges (λ= 390-680, 680-1200, 1200-1900 nm), then incident to the monochrometer (jasco-CT250). The monochromatic light is polarized by a polarizer to the angle of 45° and modulated by piezo-birefringent modulator with p = 42 kHz frequency (PEM-90^{TM}/ model-I/FS50). The modulated light passes through the sample under magnetic field of -1.2 ～ +1.2 T applied perpendicular to the sample. After passing through the analyzer, the light is detected by the photo diode. The detector converted the optical signal to electrical signal and sent it to lock-in amplifiers. We have three types of lock-in amplifiers 1, 2 and 3 corresponding to the frequencies of dc, p and $2p$. The lock-in amplifier-1 detects the dc optical signal (transmitted optical intensity) while the lock-in amplifier 2 and 3 detect the signals that related to Faraday ellipticity and Faraday rotation respectively. All the measurement systems are controlled by GPIB cables and these signals are saved to Excel file. All the measurements have been done at room temperature. Fig. 3.19 shows the picture of equipment for polarization modulation systems used in this study.
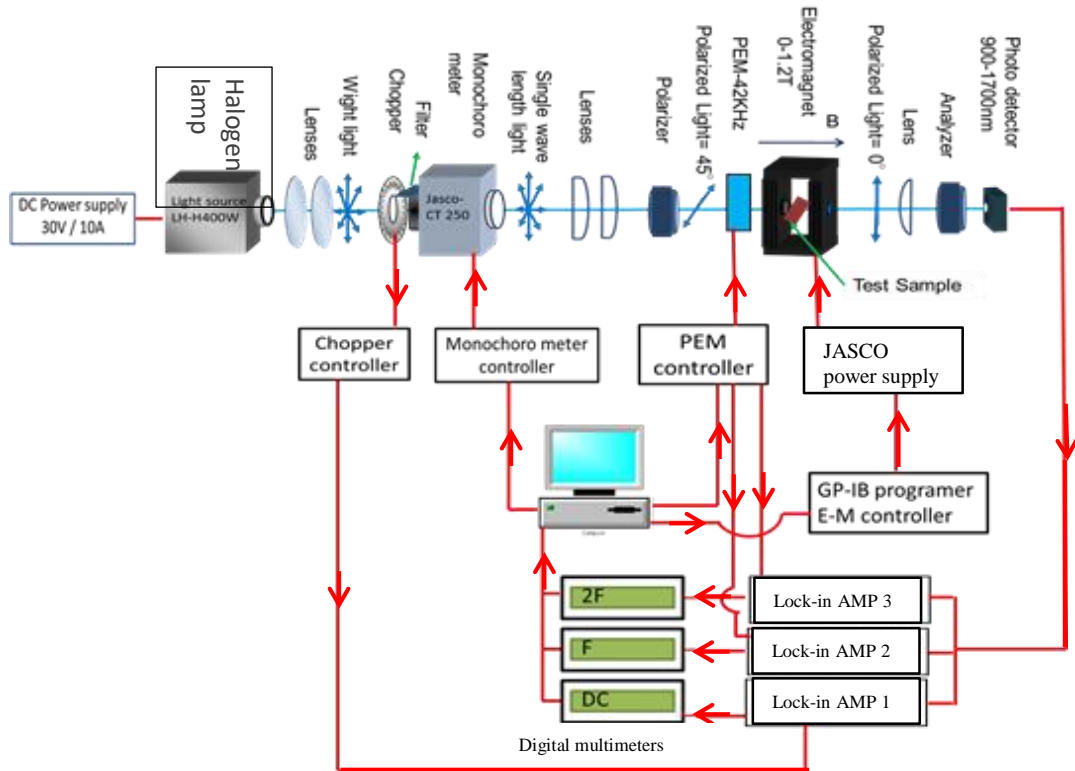
Fig. 3.18 Overall diagram of Faraday effect measurement by the polarization modulation technique.
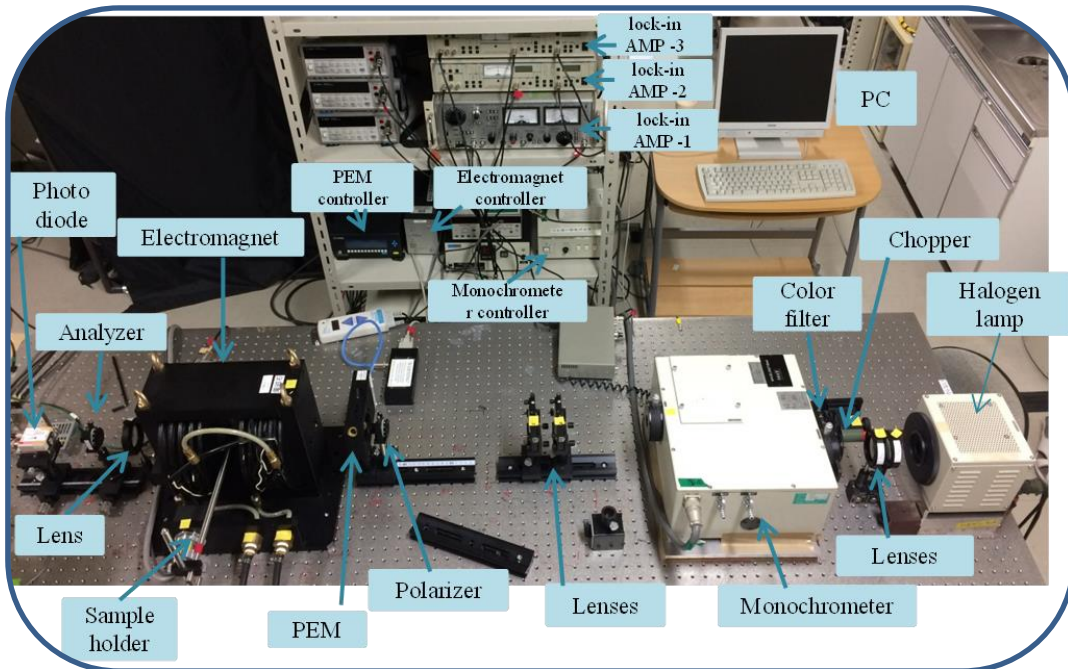
Fig. 3.19 Polarization modulation system for FR measurement.

3.3.3 Optical transmittance and reflectivity measurement

3.3.3.1 Transmittance measurement

In order to measure the Faraday rotation of a sample in a specified wavelength ranges, the sample must be transparent. Therefore it is necessary to measure the transmittance spectra for further Faraday rotation measurement in a specified wavelength ranges. Also I used the transmittance spectra for estimating the thickness of the films. The measurement of the optical transmittance is conducted from one sides of the sample at the angle of 90° (normal) to the surface of the film. The measurement has been done at room temperature in $\lambda = 250 – 2500$ nm wavelength region. I determined the transmittance spectra as following formula (3.41).

$$T(\%) = \frac{\text{Intensity of light through sample I}_{out2}}{\text{Intensity of light without sample I}_{out1}} \times 100 \qquad (3.41)$$

Fig. 3.20 Schematically shows the optical transmission of light with and without sample.

Fig. 3.20 A schematic diagram of the optical transmittance measurement.

3.3.3.2 Reflectivity measurement
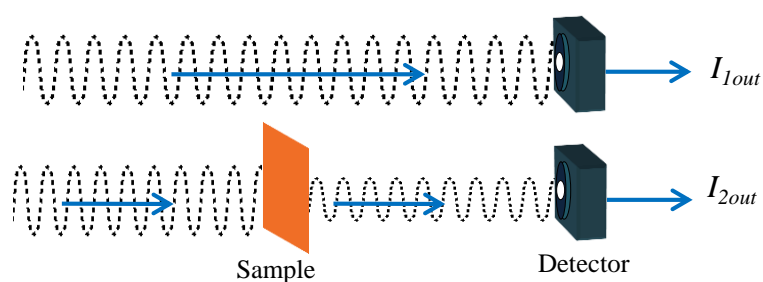
In order to measure the thickness of magnetic garnet thin films I used the reflectivity spectra. The measurement of the reflectance is conducted from one sides of the sample at the angle of 90° (normal) to the surface of the film. The measurement has been done at room temperature in $\lambda = 250 - 2500$ nm wavelength range. I used the reflectivity spectra of Si mirror as reference or baseline in the system for measurement of reflectivity spectra of my samples. Other types of mirror like aluminium mirror also can be used.

Fig. 3.21 shows an example of the transmittance and reflectivity spectra of the $Bi_2Gd_2Fe_5O_{12}$ magnetic garnet thin film on a single crystal (111) SGGG substrate.
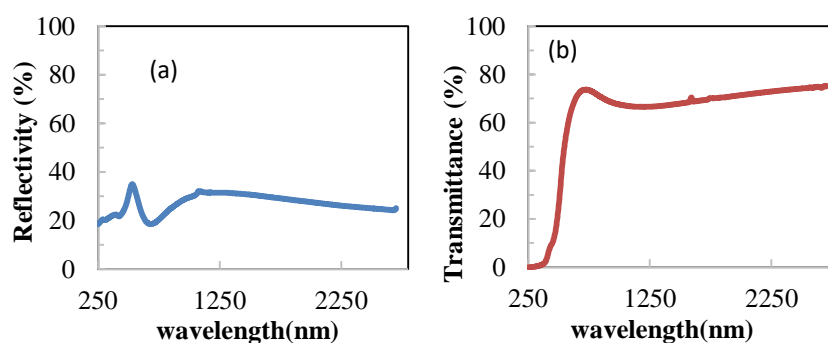
Fig. 3.21 (a) Optical reflectivity and (b) optical transmittance spectra of Bi:GdIG on (111) SGGG substrate

We used the spectrophotometer (JASCO V-670) for the optical transmittance and reflectance measurement. The double-beam spectrophotometer V-670 utilizes a unique, single monochromator design covering a wavelength range from 190 to 2500 nm (3200nm optional). The monochromator features dual gratings (automatically exchanged):1200 grooves/mm for the UV/VIS region and 300 grooves/mm for the NIR

region. A PMT detector is provided for the UV/VIS region and a Peltier-cooled PbS detector is employed for the NIR region. Both gratings and detectors are automatically changed within the user selectable 750 to 900 nm range. Fig. 3.22 (a) shows the image of V-670 spectrophotometer [38]. Fig. 3.22 (b) shows the light path for optical transmittance and Figure 3.22 (c) shows the light path for optical reflectance spectra measurements in V-670 spectrophotometer.

Fig. 3.22 Transmittance and reflectance measurement concept, M_1-M_8 and M_a-M_f stand for mirror, D stand for detector and S stand for sample.

3.3.4 Principle of thickness estimation of thin films

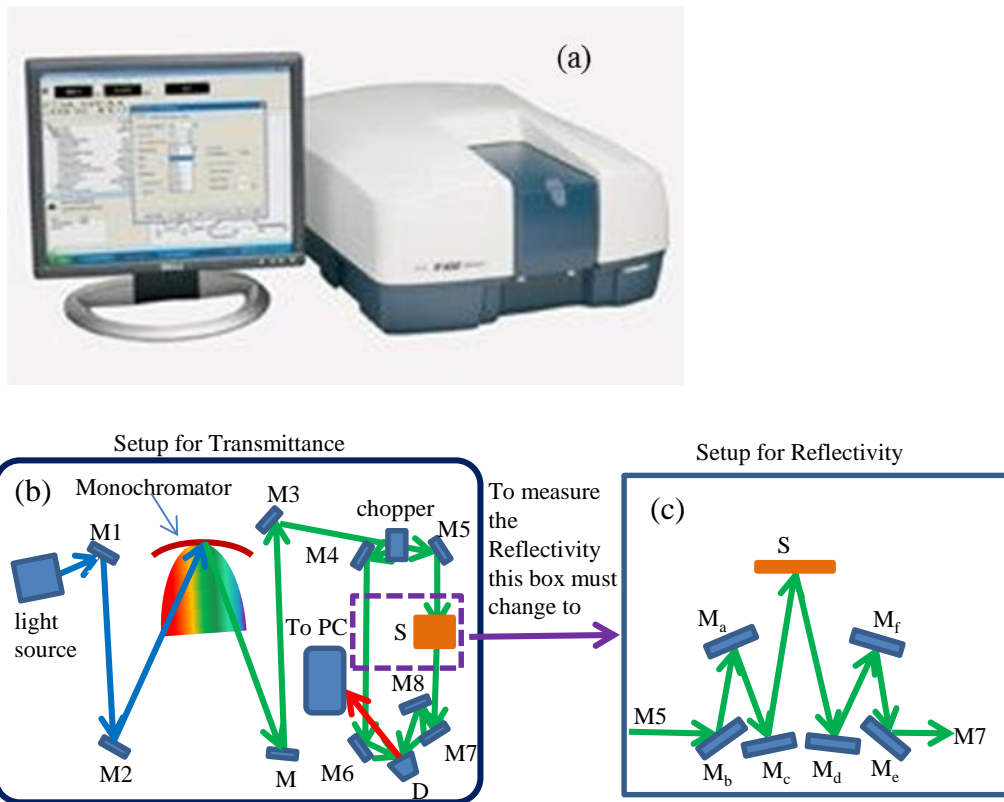The Faraday rotation of thin films is proportional to the thickness as described by formula (3.11). Also the magnetic anisotropy and Faraday rotation are influenced by crystalline quality and strain effect. The crystalline quality and strain effect of the sample depend on the thickness of the thin films. Therefore it is important to measure the thickness of thin film.

I estimated the thickness of our samples by optical reflectance and transmittance spectra. I fitted the measured optical reflectivity spectra to reproduce the experimental results by the calculated reflectivity spectra. I calculated the reflectivity spectra by considering the multiple reflections inside the $Bi_xGd_{3-x}Fe_5O_{12}$ films by interfaces between air / film (af), and film / glass substrate (fs) [39-40]. We assumed that the film thickness is uniform and the glass substrate is non-absorbing and incoherent material [41].

3.3.4.1 Calculation of three layered structure

Fig. 3.23 shows the schematic illustration of the optical transmittance and reflectance of a uniform plane wave with normal incident ($\theta = 0$) in a three layer structure of {air/ thin film/ air} (afa), where layer 1 has a real index of refraction n_0 and extinction coefficient $k_0 = 0$, ($\tilde{n}_0 = n_0$), layer 2 has a finite geometrical thickness d_1 and a complex index of refraction $\tilde{n}_1 = n_1 - jk_1$, and the complex index of layer 3 is the same as that of the layer 1.

$R_{af} = r_1$, $R_{fs} = r_2$, $T_{af} = t_1$ and $T_{fs} = t_2$ are the reflectance and transmittance coefficient of air/film, inside the film, and film/air, q_1 is the phase factor.

$$r_1 = \frac{\tilde{n}_0 - \tilde{n}_1}{\tilde{n}_0 + \tilde{n}_1} \tag{3.42}$$

$$r_2 = \frac{\tilde{n}_1 - \tilde{n}_0}{\tilde{n}_1 + \tilde{n}_0} \tag{3.43}$$
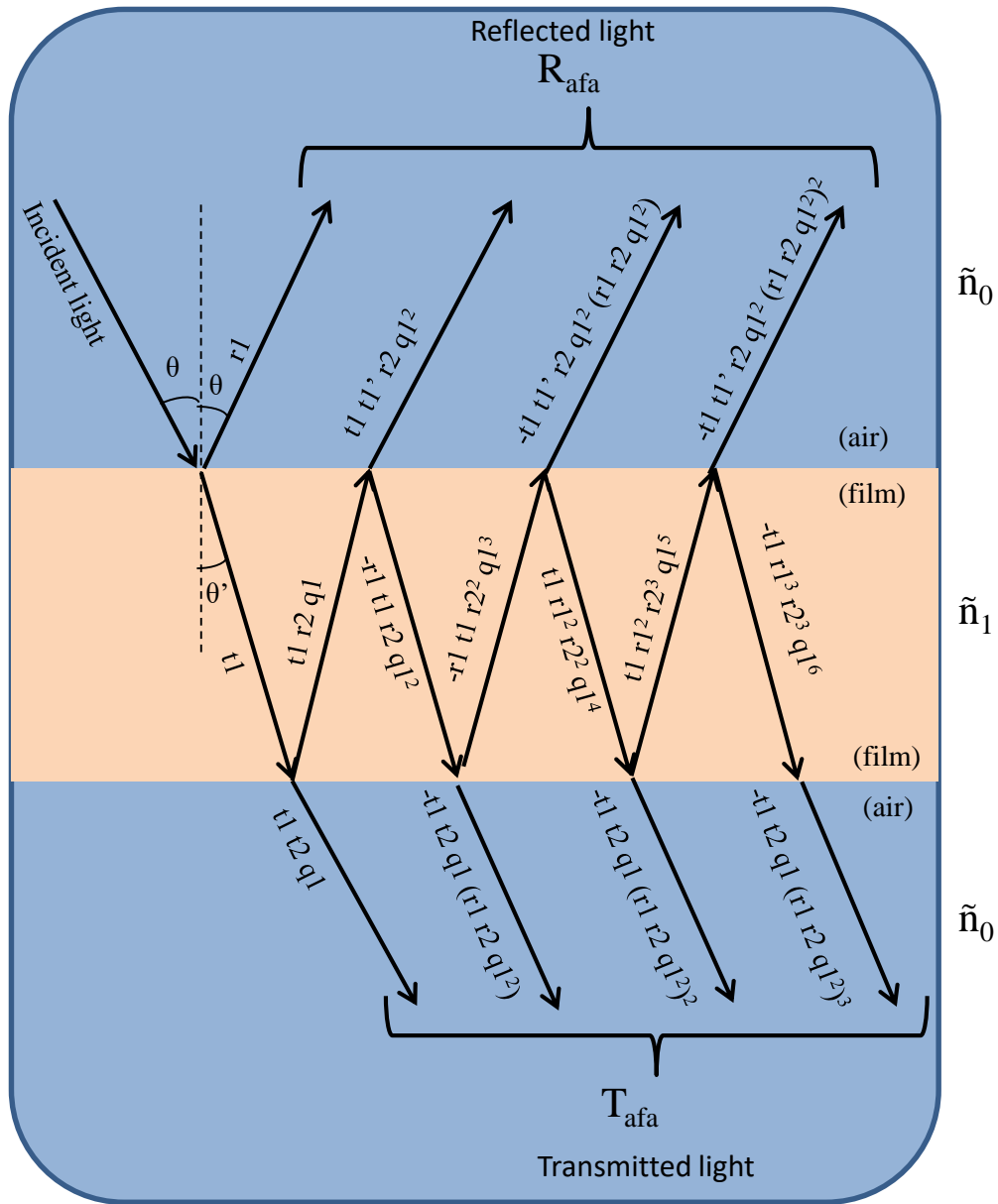

Fig. 3.23 A Schematic image of the optical transmittance and reflectance in the three layered structures (air/film /air).

$$t_1 = \frac{2\tilde{n}_0}{\tilde{n}_0 + \tilde{n}_1} \tag{3.44}$$

$$t_2 = \frac{2\tilde{n}_1}{\tilde{n}_1 + \tilde{n}_0} \tag{3.45}$$

$$q_1 = e^{-ik_0(n_1 - ik_1)d_1} \tag{3.46}$$

If the $\theta = 0$ (normal incidence), the reflected amplitude R $_{air,film,air}$ (R_{afa}) is expressed as

R_{afa}= r1 + t1t1'r2q1^2 + t1t1'r2q1^2 (-r1r2q1^2) +…..

$$= \frac{r1 + r2q1^2}{1 + r1r2q1^2} \tag{3.47}$$

Here, the multiple reflections within the film are considered.

The transmitted T $_{air,film,air}$ amplitude is expressed as

T_{afa}= t1t2q1+t1t2q1 (-r2r1q1^2) + t1t2q1 (-r1r2q1^2) (-r1r2q1^2) +……

$$= \frac{(r1 + 1)(r2 + 1)q1}{1 + r1r2q1^2} \tag{3.48}$$

3.3.4.2 Calculation of four layer structure {air / film / sub / air}

I fabricated magnetic garnet thin films on (111) GGG, (111) SGGG substrate and non-crystal glass substrates. The optical behavior of thin films treated in the framework of the coherent formulations already discussed in preceding sections (3.3.4.1). However, the effect of thick substrate should be considered and treated incoherently. We assumed that the substrate has refractive index and small optical absorption. It is necessary to consider four layer structures [air/film/substrate/air] to estimate the thickness of the thin film fabricated on substrates. To estimate the thickness of the thin films deposited on top of a sufficiently thick substrate, such as GGG, SGGG or glass substrates, I assumed that both thin film and substrate have smooth and flat surfaces.

Fig. 3.24 shows the schematic image of the multiple transmittance and reflectance of light among three interfaces {air/thin film/thick sub/air}. When a light beam is incident on the *air-film* interface from air medium (layer 1), it will be partially reflected and the other part is refracted into the film (layer 2) toward the *film-substrate* interface. This refracted (transmitted) light beam in turn is partly reflected inside the film and partly transmitted into the substrate (layer 3). The light beam transmitted inside the substrate, continue propagating toward its backside of the substrate and reach to the interface between substrate and air (layer 4). A part of the light is transmitted to air (layer 4) while the other part is reflected into the substrate, propagating through it in the opposite direction and heading toward its internal boundary with the film. The reflected light beam is in turn partly transmitted inside the film and partly reflected again into the substrate, as shown in Fig. 3.24.

The complex refractive indices of air, layer 2 (film) and substrate are $\tilde{n}_0 = n_0$, $\tilde{n}_1 = n_1 - jk_1$, $\tilde{n}_2 = n_2 - jk_2$. The film thickness is d. The reflectivity R is calculated as the following formula, based on the discussion in the previous subsection.

$$R = R_{afs} + \frac{R_{sa}(T_{afs})^2}{1 - R_{sa}R_{sfa}} \tag{3.49}$$

where R_{afs}, is the reflectivity within the interface between air (a)/film (f), and the interface between film (f)/substrate (s), R_{sfa} is the reflectivity within the interface between substrate (s)/film (f), and the interface between film (f)/air (a) T_{afs} is the transmission within the interface between air (a)/ film (f), and the interface between film (f) substrate (s). R_{afs}, R_{sfa} and T_{afs} include the effect of the multiple reflections inside the film and can be expressed by the following formulas (3.50), (3.51) and (3.52). They are related to the film thickness d, wavelength λ, and refractive index n - ik of the

film.

$$R_{afs} = \frac{R_{af} - (2R_{af}R_{fs} - R_{fs})e^{-\frac{4\pi}{\lambda}(n-ik)d}}{1 - R_{af}R_{fs}e^{-\frac{4\pi}{\lambda}(n-ik)d}}$$ (3.50)

$$T_{afs} = \frac{(1 - R_{af})(1 - R_{fs})e^{-\frac{2\pi}{\lambda}(n-ik)d}}{1 - R_{af}R_{fs}e^{-\frac{4\pi}{\lambda}(n-ik)d}}$$ (3.51)

$$R_{sfa} = \frac{R_{fs} - (2R_{af}R_{fs} - R_{af})e^{-\frac{4\pi}{\lambda}(n-ik)d}}{1 - R_{af}R_{fs}e^{-\frac{4\pi}{\lambda}(n-ik)d}}$$ (3.52)

The refractive index has wavelength dependence. Since magnetic garnets is absorptive in $\lambda \leq 1000$ nm and almost transparent in $\lambda \geq 1000$ nm, I divided the optical reflectivity spectra to two regions ($\lambda < 1000$ nm and $\lambda > 1000$ nm), and changed the refractive index and thickness to reproduce the experimentally obtained optical transmission spectra [39,40]. In the final stage of the fitting, the films thickness d is obtained.
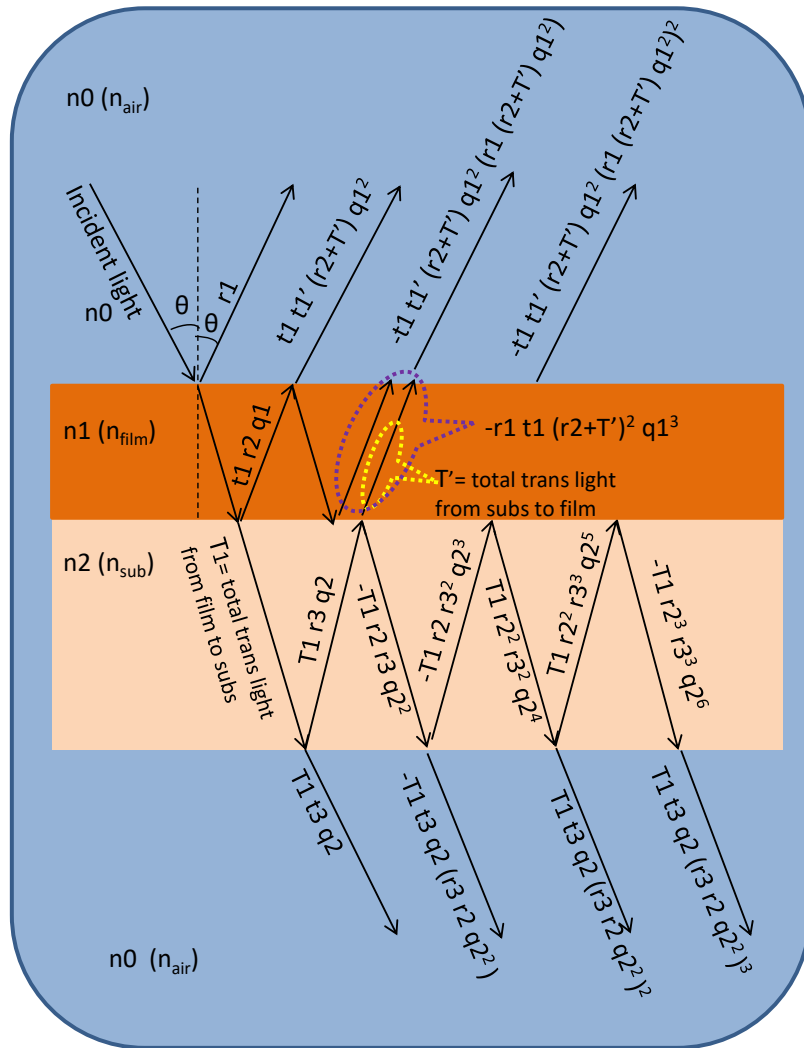
Fig.3.24 A schematic image of the optical reflection and transmission in four layer structure considering multiple transmittance and reflectance with normal incident ($\theta = 0$).

Fig. 3.25 shows an example of the optical reflectivity spectra (wavelength range λ = 250 - 2600 nm) of the $Bi_xGd_{3-x}Fe_5O_{12}$ samples annealed at 620, 650 and 700 °C, with the Bi content x = 0, 1, 2 and 2.5 on glass substrates. The simulated reflectivity spectra shown by dotted lines are fitted to the measured reflectivity spectra. The thicknesses were estimated to 170 - 210 nm for the samples with x = 1, 200 - 260 nm for the samples with x = 2, and 330 - 360 nm for the samples with x = 2.5. The detail analysis

will be discussed in the later section.

Fig. 3.25 An example of the optical reflectivity spectra (solid lines) with simulated spectra of $Bi_xGd_{3-x}Fe_5O_{12}$ samples annealed at 620, 650 and 700 °C, with bismuth content $x = 0$, 1, 2 and 2.5 on glass substrates. The fitted spectra are shown by dashed lines.
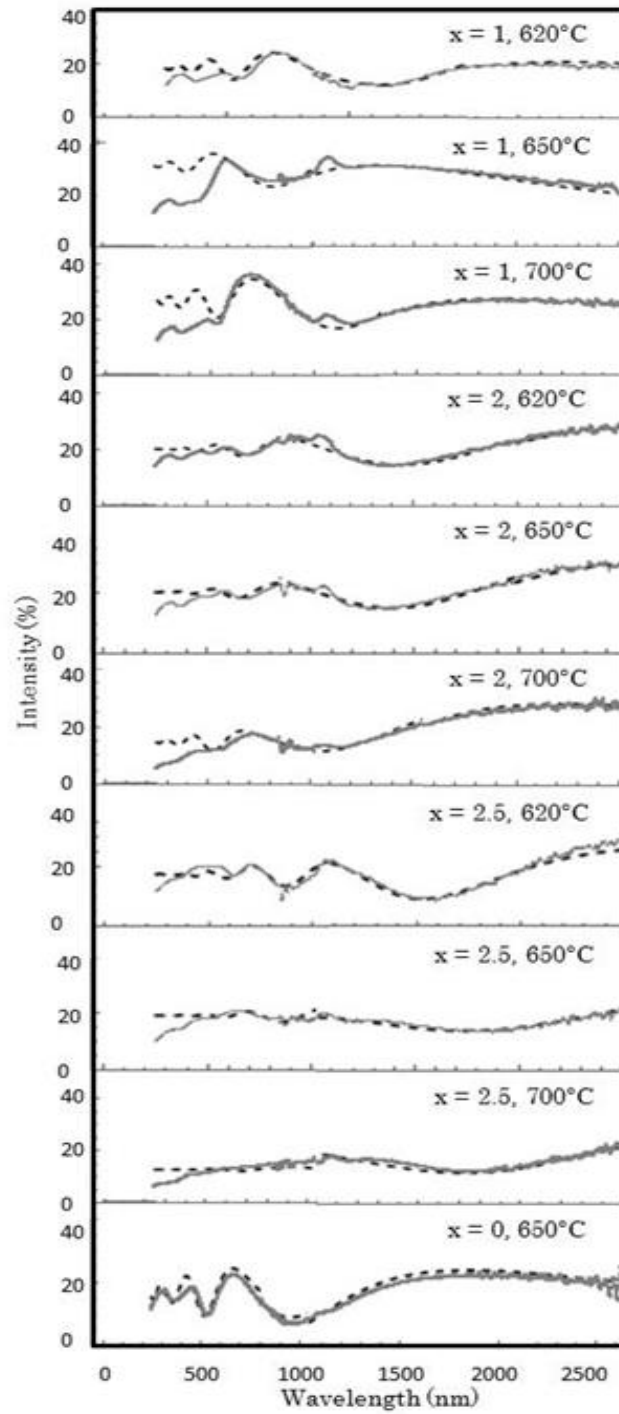
3.3.5 Principle of Magnetization measurement by alternating gradient field magnetometer (AGFM)

Since one of the core purposes of my research is to control and change the magnetic anisotropy of magnetic garnet thin films by the fabrication conditions, the measurement of magnetization is very important. The magnetization under magnetic field perpendicular to the sample is proportional to the Faraday rotation. The magnetic field dependence of the Faraday rotation is proportional to the magnetization.

Magnetization is defined as the number of magnetic dipoles (magnetic moment) in unit volume. The origin of magnetic moment arises from the electron spin and orbital magnetic moment as described in chapter 2. Usually the magnetization is denoted by M. When there are magnetic moments m_1, m_2, m_3, …..m_n in a unit volume of the magnetic material the magnetization is given by.

$$M = \sum_{i=1}^{n} m_i \tag{3.53}$$

When a magnetic material is placed under magnetic field, magnetic moments start to align to the direction of magnetic field, leading to magnetization M. Magnetic flux density is defined as

$$B = M + \mu_0 H \tag{3.54}$$

Where B is magnetic flux density, M is magnetization, μ_0 is permeability in vacuum and H is the intensity of magnetic field.

We used the Alternating Gradient Field Magnetometer (AGFM) technique to characterize the magnetization of fabricated magnetic samples.

The idea for the AFGM was introduced by Zijlstra for the first time [42].

The AGFM uses a set of gradient coils that produce a gradient AC magnetic field. The AC field produces a force on the sample that fixed on a quartz glass capillary that causes the sample to start vibrating and the amplitude of this vibration is proportional to the magnetic moment of the sample. This vibration is detected by a displacement or force sensor in the system. These sensors are usually based on piezo electric devices. To increase the sensitivity of the AGFM, the sample is vibrated at a frequency close to the resonance frequency of the sample rod. Then, the system is sensitive to the actual weight of the measurement sample.

I placed a 3x3 mm^2 Bi:GdIG sample on GGG substrate at the end of glass capillary that is connected to piezo-electric bimorph. The provided piezo voltage is connected to lock-in amplifier, and converted to the total magnetic moments inside the sample. The magnetization curve is shown in unit of (emu) to the magnetic field in unit of kOe. I changed the unit of [emu] to [emu/cc] and (T) Tesla by using the following formulas (3.55) and (3.56). Also I converted the unit of magnetic field [kOe] to μ_0H[T] by using the following formula (3.57).

$$emu/cc = \frac{\text{magnetization in emu}}{\text{Total volume of magnetic sample (cm}^3)} \tag{3.55}$$

$$1 \text{ emu/cc} = 1 \text{ gauss [G]} = 0.0001 \text{ Tesla [T]} \tag{3.56}$$

$$B = \mu_0 H, \qquad 10\text{kOe} = 1\text{Tesla [T]} \tag{3.57}$$

Fig. 3.26 shows an example of the magnetization curve of the $Bi_1Gd_2Fe_5O_{12}$ thin film on (111) GGG substrate.
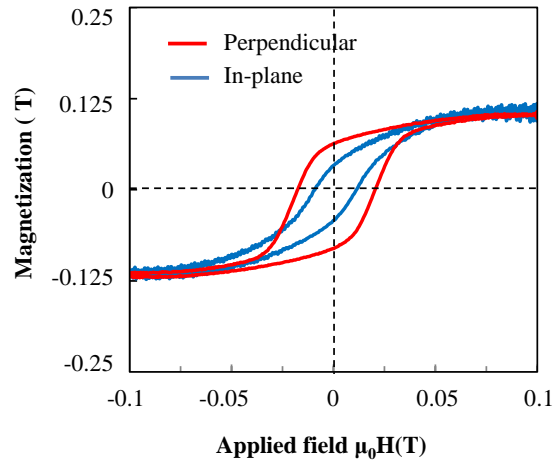
Fig. 3.26 An example of the magnetization curve of the Bi:GdIG thin film on single crystal (111) GGG substrate, red curve shows M under magnetic field ⊥ sample plane (perpendicular) and blue curve shows M under magnetic field ‖sample plane (in plane).

Fig. 3.27 shows the picture of the AGFM system used for this study in Prof. Tanaka's Lab at the University of Tokyo.

Fig. 3.27 AGFM system used for measuring the magnetization of the samples. M-Poles stand for electromagnet poles.

CHAPTER 4

Preparation and Characterization of $Bi_1Gd_2Fe_5O_{12}$ thin films by MOD method on (111) GGG substrate

4.1. Introduction

In this chapter, I will discuss the preparation and characterization bismuth substituted gadolinium iron garnet (Bi:GdIG) thin films on gadolinium gallium garnet (GGG) substrates prepared by metal organic decomposition (MOD) method i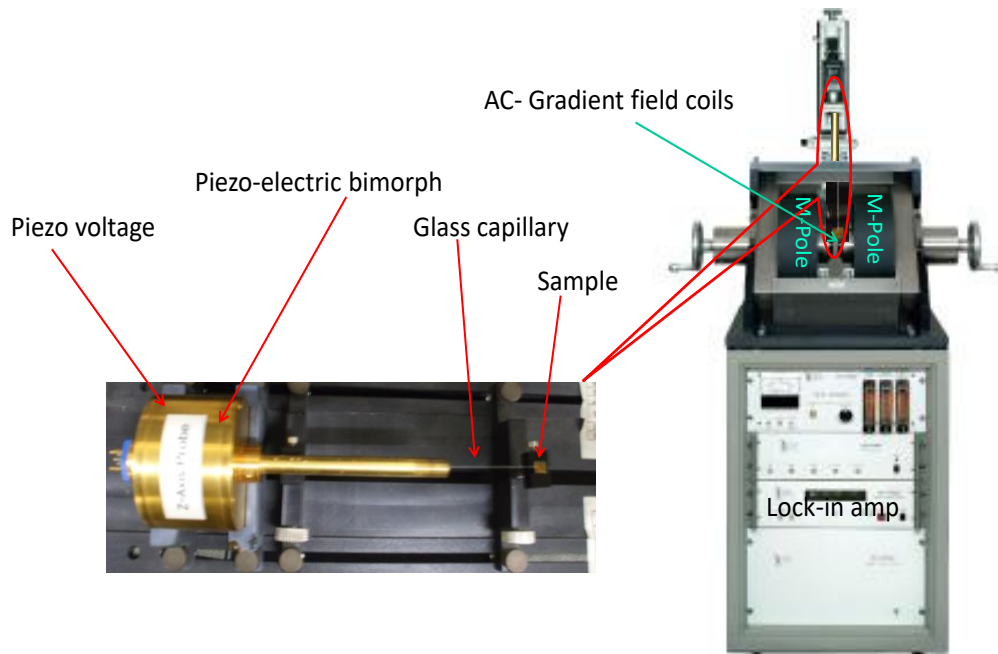n order to obtain high-quality garnet crystal with a large Faraday rotation and control the magnetic anisotropy of magnetic garnet by changing the fabrication conditions, such as annealing temperature and annealing gas. Because there have been no reports about investigation of the presence of O_2 gas in the annealing process of the MOD method and its influence on the magneto-optical property, and magnetic anisotropy of Bi:GdIG films. We used two kinds of annealing gas of 100% N_2 and 20% O_2 + 80% N_2 and crystalized the

samples at annealing temperatures of 620, 650, 700, 750, and 800°C. We measured the magnetization, X-ray diffraction, Faraday effect, and optical transmittance of the fabricated samples.

Magnetization, Faraday rotation and X-ray diffraction (XRD) were used to examine their dependence on annealing temperatures and different annealing gas mixture (with and without O_2). Our results revealed that Bi substituted gadolinium iron garnet samples annealed without O_2 (100% N_2) crystallized at lower annealing temperatures. The magnetic fields to saturate the Faraday rotation were larger for the samples annealed without O_2 (100% N_2) than those of samples annealed with 20% O_2. The possible mechanisms responsible for these phenomena are discussed in this chapter. This work has been published on the Journal of Magnetic Society of Japan [1] in 2015.

4.2. Fabrication and characterization of $Bi_1Gd_2Fe_5O_{12}$ thin film

We have fabricated bismuth substituted gadolinium iron garnet (Bi:GdIG) thin films by metal organic decomposition method on (111) GGG substrates with different annealing temperature and annealing gas. The area of the GGG substrate is 12 mm x 12 mm. A MOD liquid used in this experiment consists of solutions made from Bi_2O_3, Gd_2O_3 and Fe_2O_3 carboxylates with chemical composition ratio of $Bi_2O_3:Gd_2O_3:Fe_2O_3$ = 1:2:5 by Kojundo Chemical Laboratory Ltd. The total concentration of carboxylates in these MOD solutions was fixed at 3 %. After spin coating in 2 steps process of 500 rpm for 10 s and 3000 rpm for 20 s, followed by drying on a hot plate at 120°C for 10 min. In order to decompose organic materials and obtain amorphous oxide films, the samples were annealed at 550°C for 10 min (pre-annealing). and annealed at 620 - 800°C for 2 hours (final annealing) for crystallization. Spin coating, drying and pre-annealing, were repeated for 6 times to obtain an appropriate thickness. In order to investigate the presence of O_2 gas in annealing process of the MOD method and its influence on the magneto-optical property of Bi:GdIG, the pre annealing and final annealing were performed with two kinds of annealing gas of 20% O_2+80% N_2 and 100% N_2. The pressure during the annealing was atmospheric pressure. Bi:GdIG thin films prepared in this study were investigated by X-ray diffraction (XRD), optical transmittance spectra, Faraday effect with its spectra and magnetic field dependence and magnetization measurements. All the measurement was done at room temperature. We measured the XRD from the central part of the samples. The diameter d of the X-ray beam is about 0.4 mm. Therefore, the measurement results of the XRD show average crystallinity of the samples over $d = 0.4$ mm. The film thickness is thin at the center of the samples, and thicker at the edge of the samples, owing to the influence of the

viscosity of the MOD solution, and the spin coating process. Because of the limited sample area, we could not fully discuss the in-plane uniformity of the crystallinity of all over the samples.

Table 4.1 shows the summary and the Fig. 4.1 shows the photo image of $Bi_1Gd_2Fe_5O_{12}$ thin films prepared on (111) GGG substrate at different annealing

Table 4.1. Summary of $Bi_1Gd_2Fe_5O_{12}$ thin films on (111) GGG substrate.

No.	Sample	T_{FA} [°C]	Annealing gas
1	A	620	100%N_2
2	B	650	100%N_2
3	C	700	100%N_2
4	D	750	100%N_2
5	E	800	100%N_2
6	A'	620	20%O_2+80%N_2
7	B'	620	20%O_2+80%N_2
8	C'	700	20%O_2+80%N_2
9	D'	750	20%O_2+80%N_2
10	E'	620	20%O_2+80%N_2

(a)

(b)
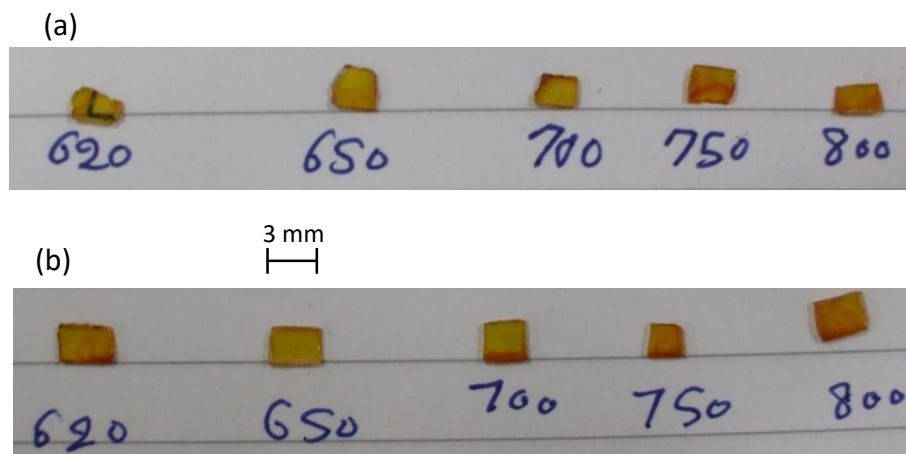

Fig. 4.1 Photo images of $Bi_1G_2Fe_5O_{12}$ thin films on (111) GGG substrate annealed at different annealing temperature 620 – 800° C under different annealing gas (a) 20%O_2+80N_2 (b) 100%N_2

91

4.3. Results and Discussion

Fig. 4.2 shows the X-ray diffraction of the Bi:GdIG thin film on GGG substrates crystallized at $620 - 800°C$ for 2 hours with two kinds of annealing gas. 444 and 888 diffraction peaks of the Bi:GdIG are clearly observed and other peaks associated with polycrystalline or impurity phases were not observed. The diffraction peaks indicate that single crystal garnet structures are observed for all the samples.

Figures 4.3 and 4.4 show the diffraction intensities and lattice constants of the lattice plane of 444 for the Bi:GdIG crystallized at different annealing temperature of $620 - 800°C$ with different annealing gas of 20% O_2 and 0% O_2, respectively. The X-ray diffraction intensities of the Bi:GdIG films annealed with 0% O_2 were stronger than those annealed in 20% O_2, indicating good crystallinity of the samples annealed with 0% O_2. The lattice constants were smaller for the samples annealed at $620 - 700°C$ with 0% O_2, compared with the samples annealed with 20% O_2, and smaller at higher annealing temperature of $750 - 800°C$ for both annealing gases, compared with the samples annealed at lower temperature of $620 - 700°C$.

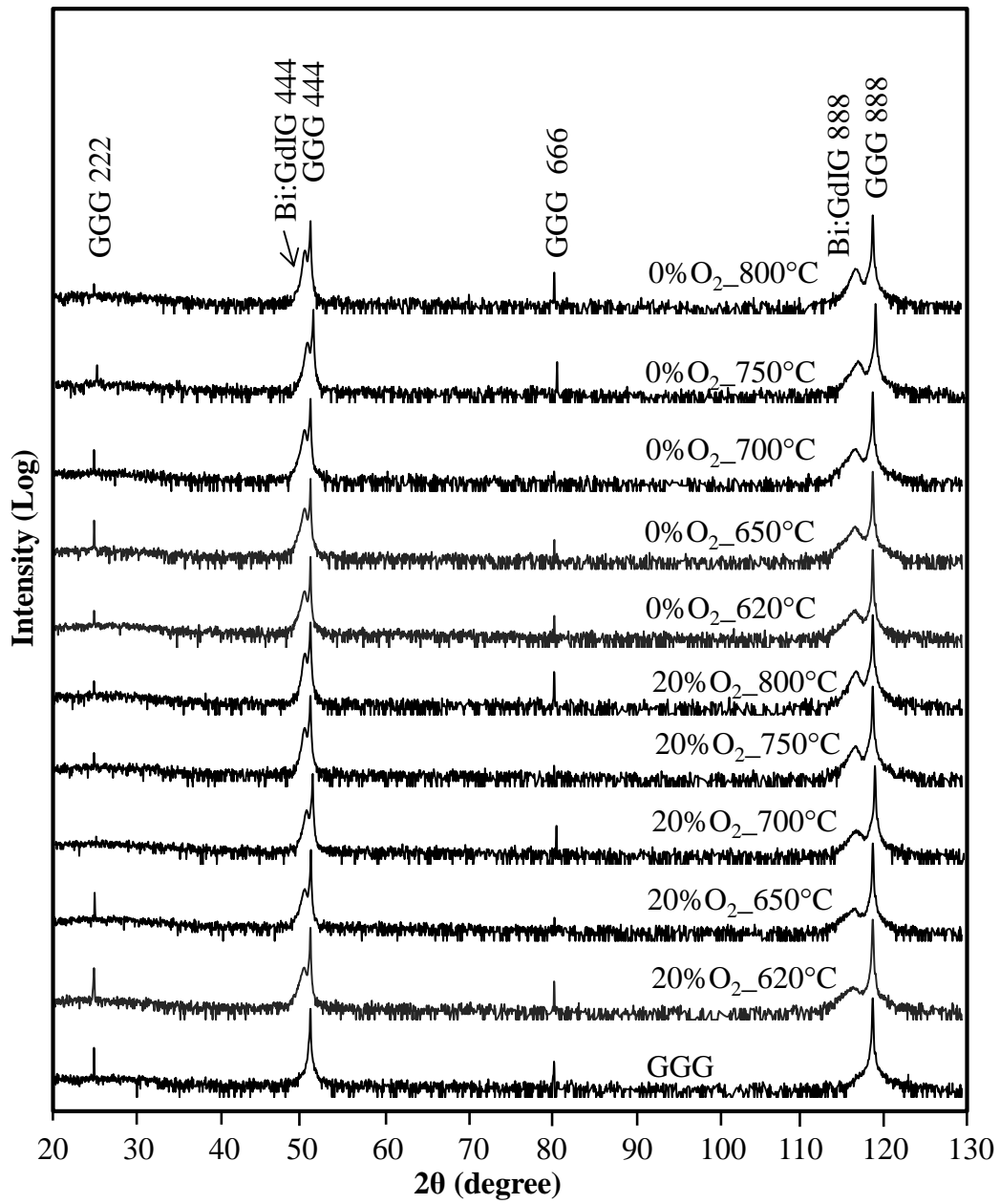Fig. 4.2 X-ray diffractions of the Bi:GdIG samples annealed at 620°C–800°C with annealing gas of 20% O_2 and 0% O_2.
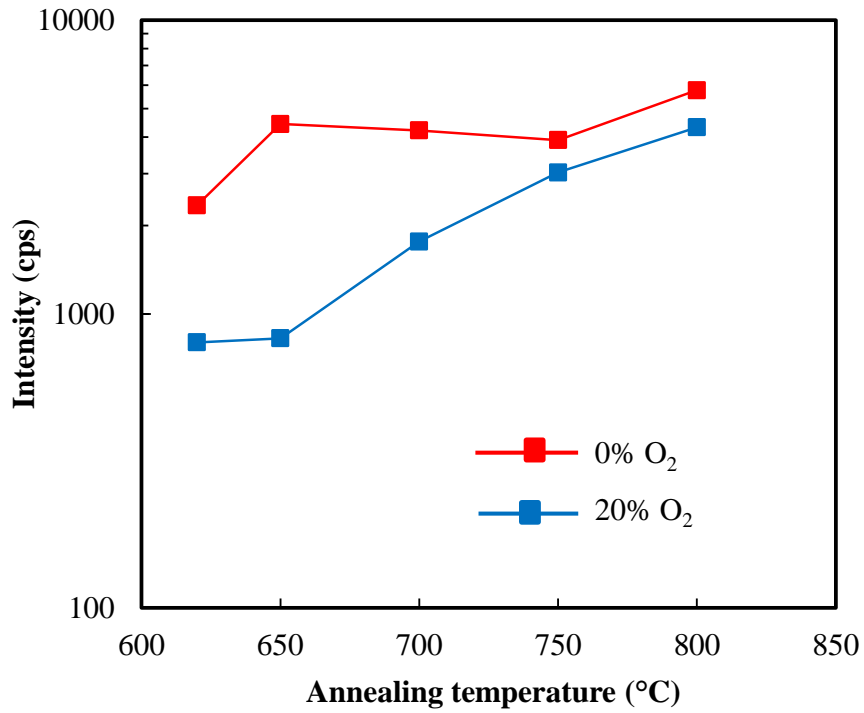
Fig. 4.3 Annealing temperature dependences of the diffraction signal from the 444 plane of the Bi:GdIG samples annealed with 20% O_2 and 0% O_2.
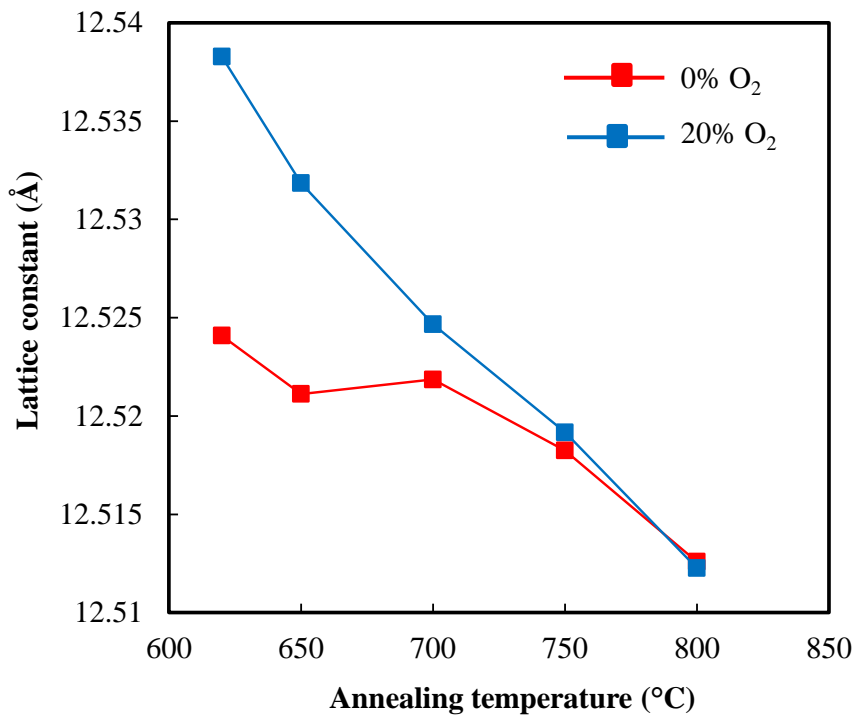

Fig. 4.4 Annealing temperature dependences of the lattice constant of the Bi:GdIG samples annealed with 20% O_2 and 0% O_2.

These experimental results indicate that the crystals grow pseudomorphically at lower annealing temperature of 620 – 700°C with 20% O_2, and the strain relaxed for the samples annealed at higher temperature of 750 - 800°C with 20% O_2, and the samples annealed with 0% O_2. The amount of the compressive strain and the dislocation defects at the interface between the Bi:GdIG film and GGG substrate are smaller for the samples annealed at higher temperature of 750 - 800°C with 20% O_2, and the samples annealed with 0% O_2. This situation is similar to superconducting $YB_2Cu_3O_{7-\delta}$ thin films grown by an electrochemical method, where $YB_2Cu_3O_{7-\delta}$ thin film was grown at lower temperature with lower O_2 pressure [2]. The authors discussed that equilibrium decomposition line could be favorable in the growth process of $YB_2Cu_3O_{7-\delta}$ thin films. The equilibrium decomposition process is one of the key to explain the reason why Bi:GdIG samples annealed with 0% O_2, crystallized better at lower annealing temperature compared with those annealed with 20% O_2. Figure.4.5 shows Faraday rotation spectra of Bi:GdIG crystallized at 620 – 800°C with 20% O_2 and 0% O_2. The magnetic field of 1T was applied perpendicular to the samples. The Faraday rotation of Bi:GdIG increases with increasing the annealing temperature. Faraday rotation showed maxima at the wavelength of about 510 nm for all the samples. In order to find the influence of annealing temperature and annealing gas on Faraday rotations, the Faraday rotation at the wavelength of 510 nm were summarized in Fig. 4.6. It was found that the sample with annealing temperature of 800°C and annealing gas of 20% O_2 shows the largest Faraday rotation among all the samples. Furthermore the maximum Faraday rotation is almost the same between the samples with two kinds of annealing gas for all the annealing temperature.
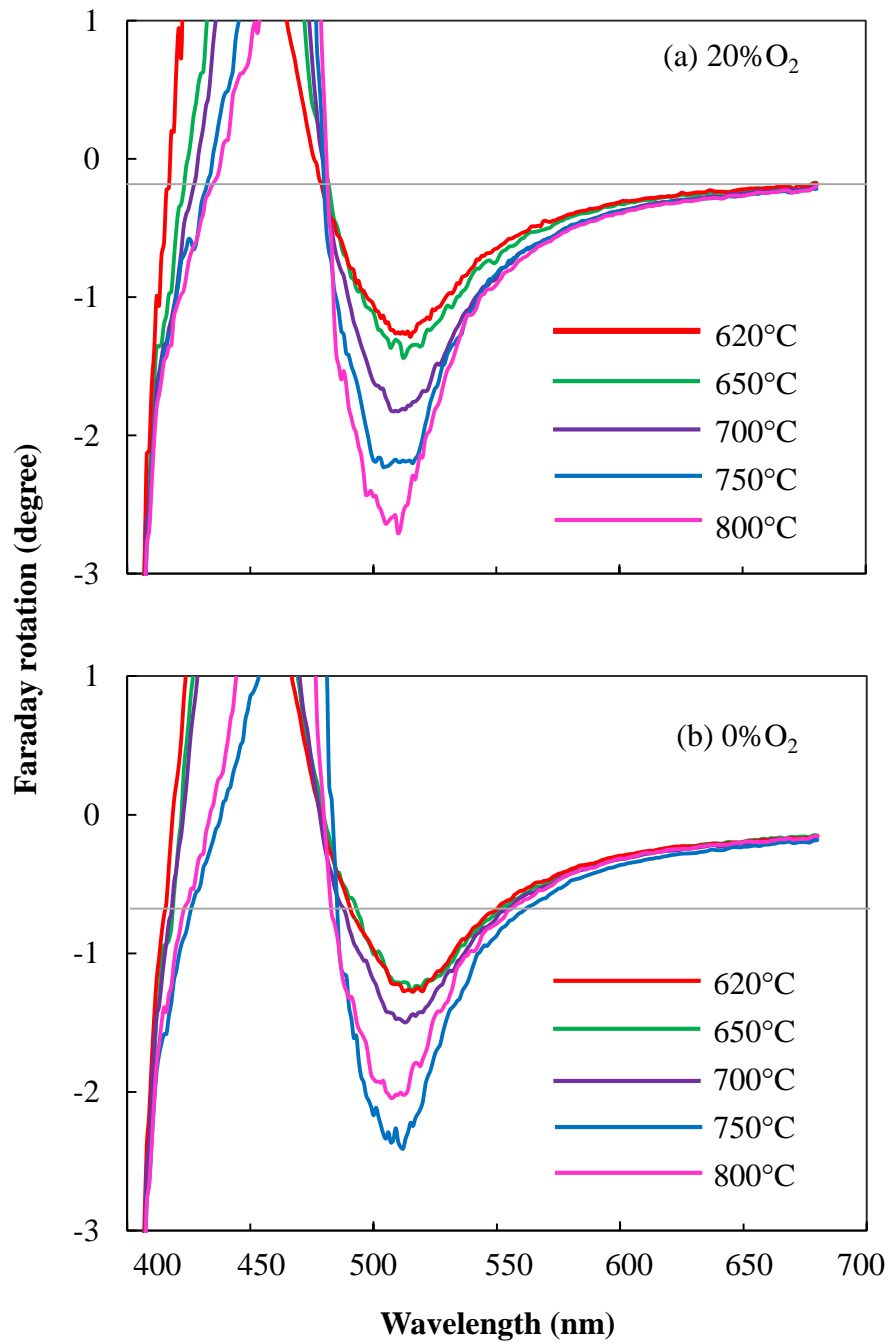
Fig. 4.5 Faraday rotation spectra of the Bi:GdIG samples with different annealing temperatures. (a) Annealed with 20% O_2 and (b) 0% O_2.
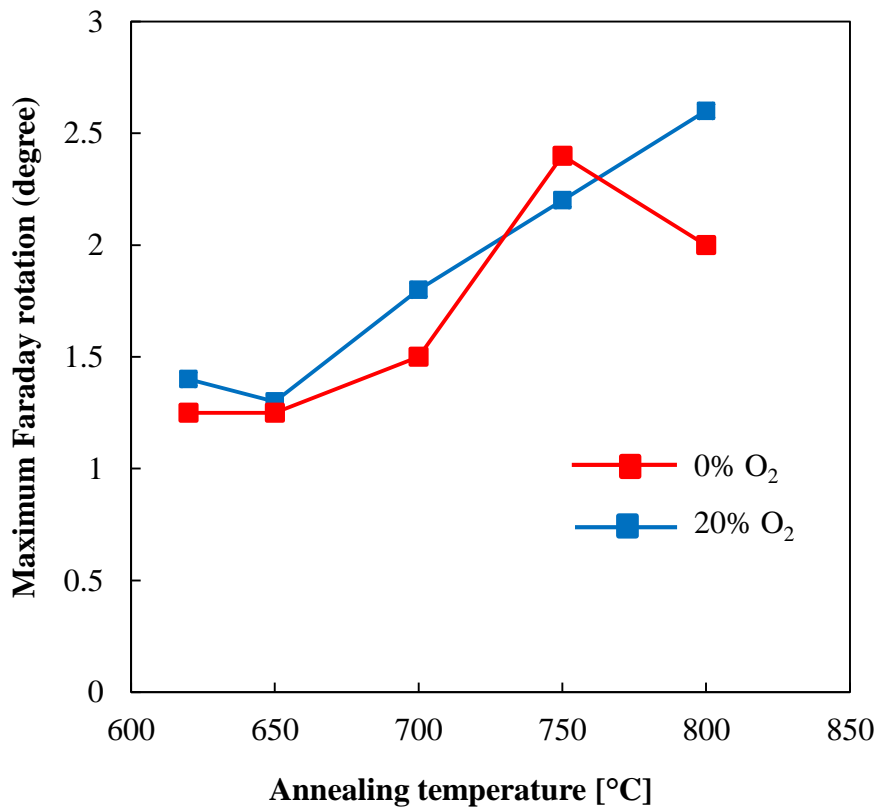
Fig. 4.6 Maximum Faraday rotation of the Bi:GdIG samples around wavelength of 510 nm annealed with 20% O_2 and 0% O_2.

Fig. 4.7 shows the optical transmission spectra of the samples. With increasing the annealing temperature, the transparency decreased in the wavelength range between 430 nm (2.88 eV) and 900 nm (1.38 eV), and almost the same in the wavelength longer than 900 nm.
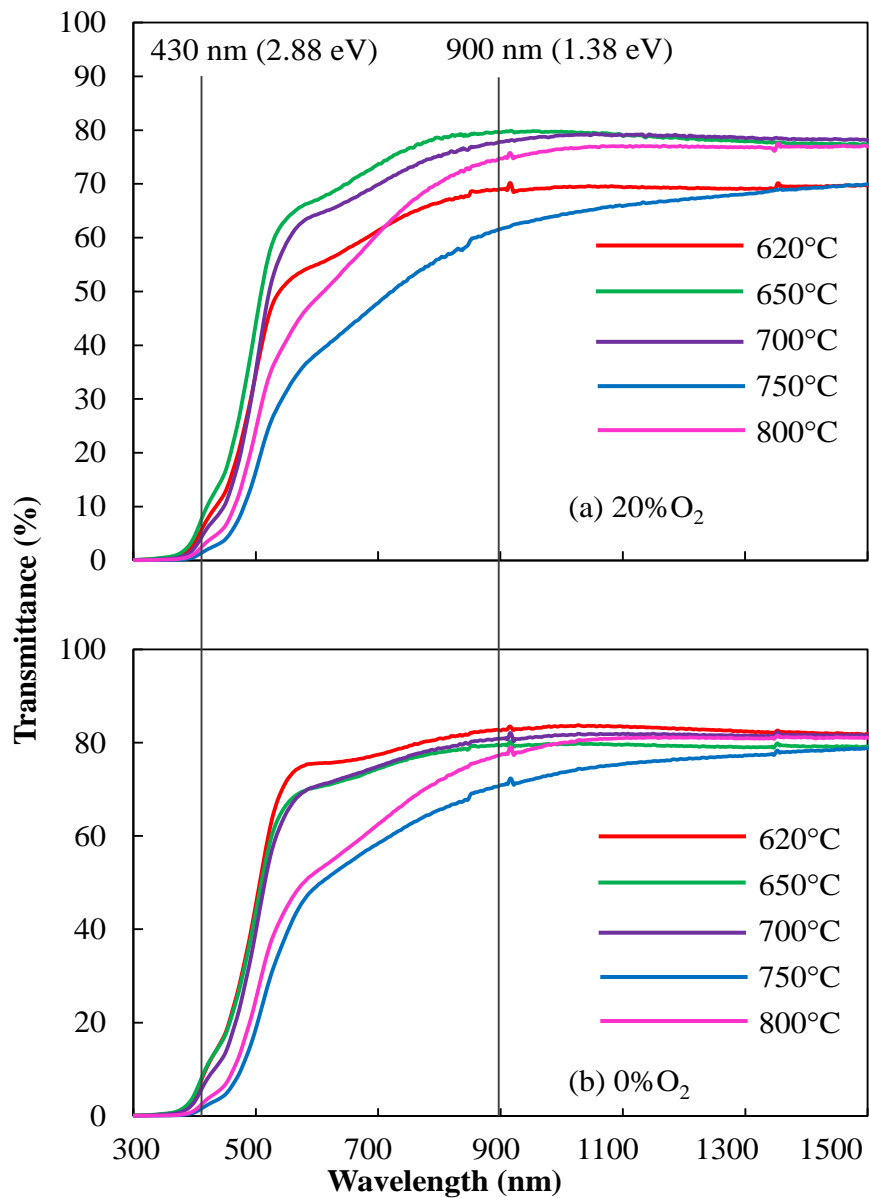
Fig. 4.7 Optical transmittance spectra of the Bi:GdIG samples annealed with
(a) 20% O_2 and (b) 0% O_2.

It was reported that the energy gap between the valence band of O^{2-} and Fe^{2+}_{oct} (t_{2g}) was 2.88 eV in YIG as shown in figure 4.8 [3]. The reason for the drop of the optical transmission at the wavelength of 430 nm can be the roughness, pinning sites or domain size, etc. One of the possible reasons is energy gap between the valence band of O^{2-} and Fe^{2+}_{oct} (t_{2g}). There are donor levels by the O_2 vacancy (defect) with the activation energy of ~1eV below the Fe^{2+}_{oct} (t_{2g}) state.

Fig. 4.8 Density of states diagram for YIG. Hatched areas denote states filled at T = 0K, The zero point of the energy scale is set at the top of the valence band [3].

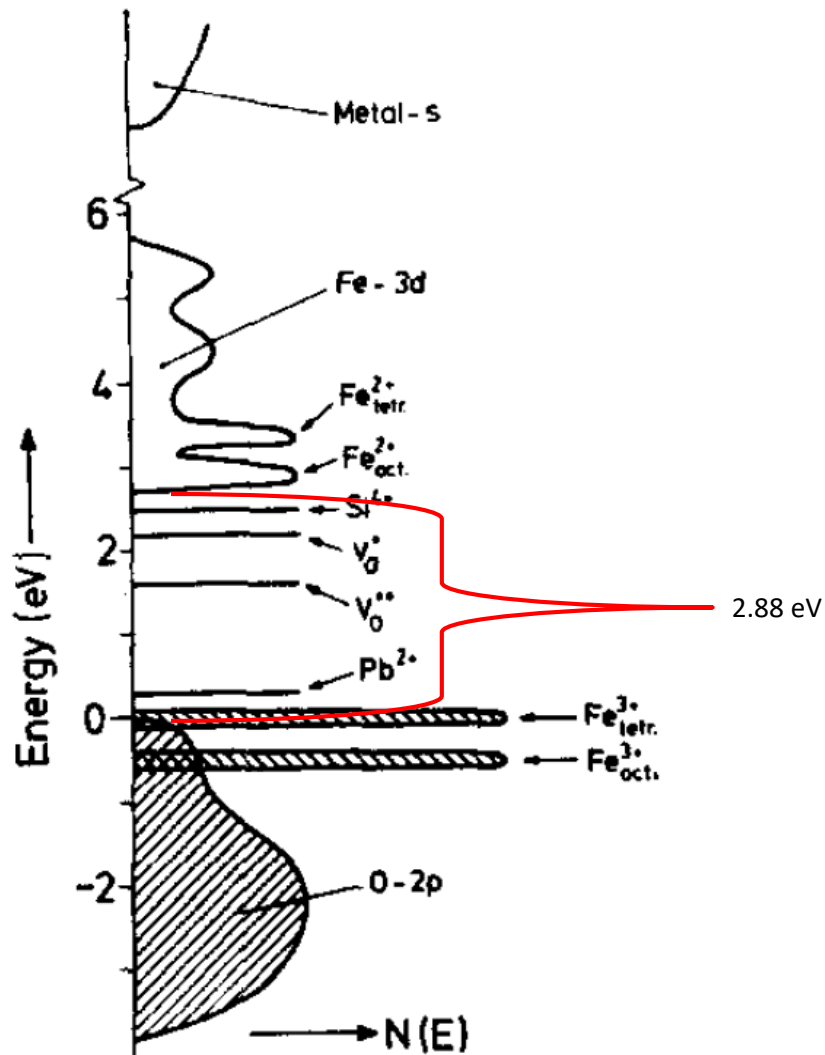The samples annealed at higher temperature showed lower optical transmittance in the wavelength range of 430 nm and 900 nm, suggesting that concentration of the O_2 vacancy (defect) states increased and the transition between the Fe^{2+}_{oct} (t_{2g}) states and the O_2 vacancy (defect) states increased in the samples annealed at higher temperature. The bumps at the wavelengths of 900, and 1350 nm are observed, which was generated by changing optical filters during the spectral measurements.

Fig. 4.9 shows the magnetic field dependence of the Faraday rotation (normalized) of the Bi:GdIG samples at the wavelength of 600 nm. The wavelength of 600 nm was selected, because the samples have high transparency (Trans > 40%). With increasing the annealing temperature, the magnetic field to fully magnetize the sample became lower. The coercive forces (H_c) of the samples are slightly higher in the samples annealed with 0% O_2, compared with samples annealed with 20% O_2. The magnetic field dependence of the Faraday rotation of the sample annealed with 0% O_2 at 620°C is similar to that annealed with 20% O_2 at 800°C.
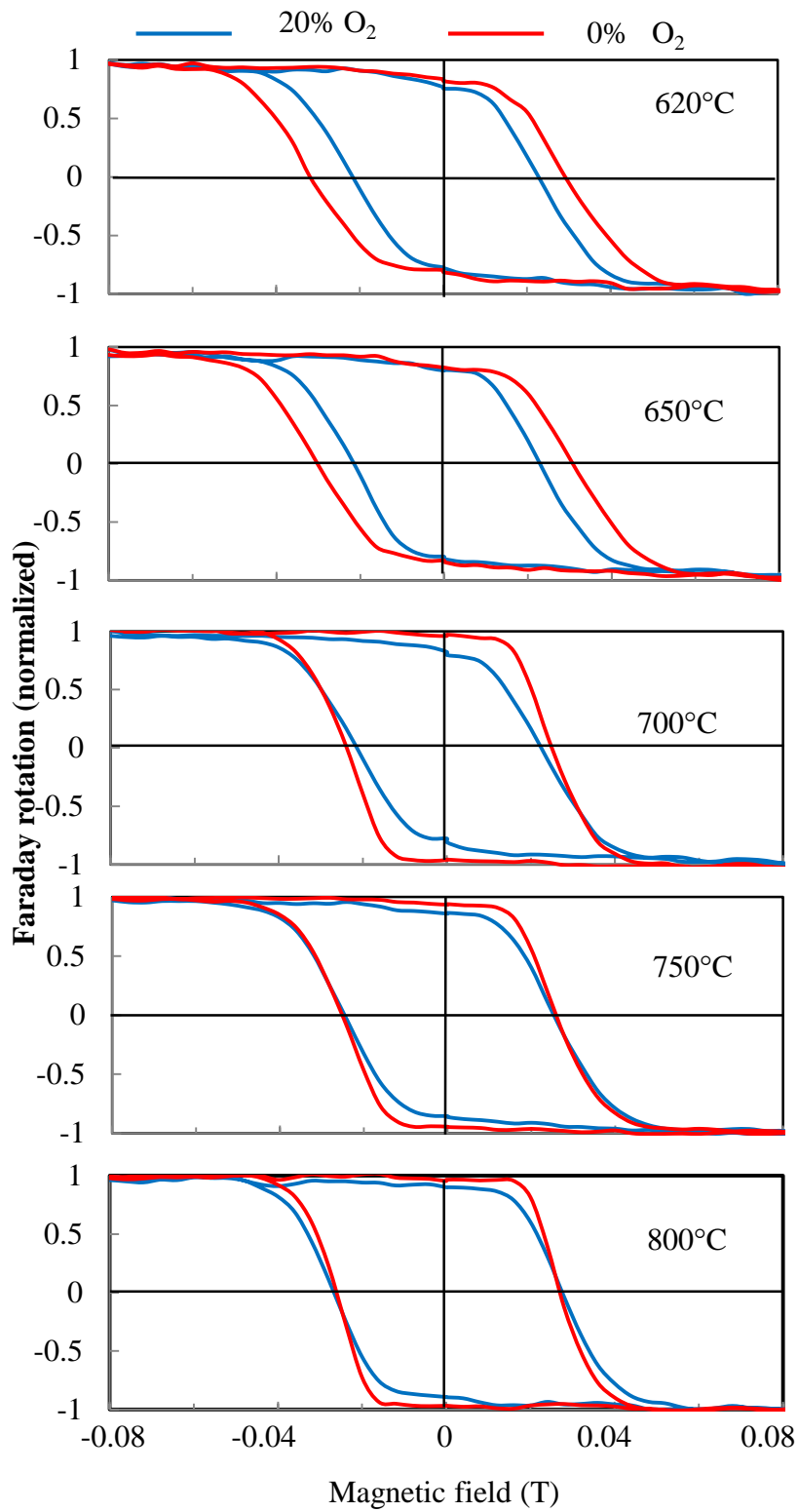
Fig. 4.9. Magnetic field dependence of the Faraday rotation of the Bi:GdIG samples annealed at 620, 650, 700, 750, and 800°C, with 20% O_2 and 0% O_2.

Fig. 4.10 shows the magnetization characteristics of the samples measured by an alternating gradient field magnetometer (AGFM), where magnetic field is applied perpendicular and in-plane to the films. The hashed areas shown by green lines show the difference of the area between the two magnetization loops.

The difference of the area between two magnetization loops is proportional to magnetic anisotropy energy as following formulas.

$$E_a = \int M_\perp \, dH - \int M_\parallel \, dH$$

$$\underline{\Delta A = Ap - Ai}$$

Where E_a is magnetic anisotropy energy, H is applied magnetic field, M is the magnetization, A_p is the area under the magnetization loop of applied magnetic field perpendicular to surface of the film. A_i is the area under the magnetization loop of applied magnetic field parallel to surface of the film and ΔA is the difference of the area between two magnetization loops. Fig. 4.11 shows that the magnetic anisotropy energy which was summarized from the magnetization characteristics of Fig.4.10. The magnetic anisotropy energy increased and larger perpendicular magnetic anisotropy was observed for $Bi_1Gd_2Fe_5O_{12}$ thin films annealed at $620 - 700°C$ with 100% N_2 and $Bi_1Gd_2Fe_5O_{12}$ thin films annealed with 20% O_2 + 80% N_2 and $100\%N_2$ at higher annealing temperature of 750 and $800°$ C than the other samples. The AGFM is very sensitive to the noise (sound). And the noise gives some error on measurement results. Therefore the saturation magnetization between in-plane and perpendicular magnetization curve are different in samples annealed at 650, 700 and $750°C$ with 0% O_2 and samples annealed at 620 and $650°C$ with $20\%O_2$.

Fig. 4.3 shows the summary of XRD intensities of the $Bi_1Gd_2Fe_5O_{12}$ thin films. Two figures (Figs. 4.11 and 4.3) show similar behavior meaning that magnetic

anisotropy energy is related to the crystalline quality and strain of the films. When the films are annealed at lower temperature (620 – 700°C) under 20% O_2 + 80% N_2, the films includes more defects inside or at the interface with GGG substrate leading to prevent the movement of the magnetic domain and smaller magnetic anisotropy, compared with other samples. When the films are annealed with 100%N_2, we found that the films are crystallized at lower annealing temperature. Please note that the amount of magnetization and Faraday rotation are almost the same regardless of the change of the annealing gas. With increasing the annealing temperature, both the magnetization and Faraday rotation became larger, meaning that the crystalline quality or strain is reduced in the films. Magnetization and magnetic anisotropy are slightly larger for the samples annealed with 100%N_2. Possible reason is that the amount of O^{2-} deficiency and Fe^{2+} increased in the samples annealed with 0%O_2, leading to slightly larger magnetization and magnetic anisotropy.
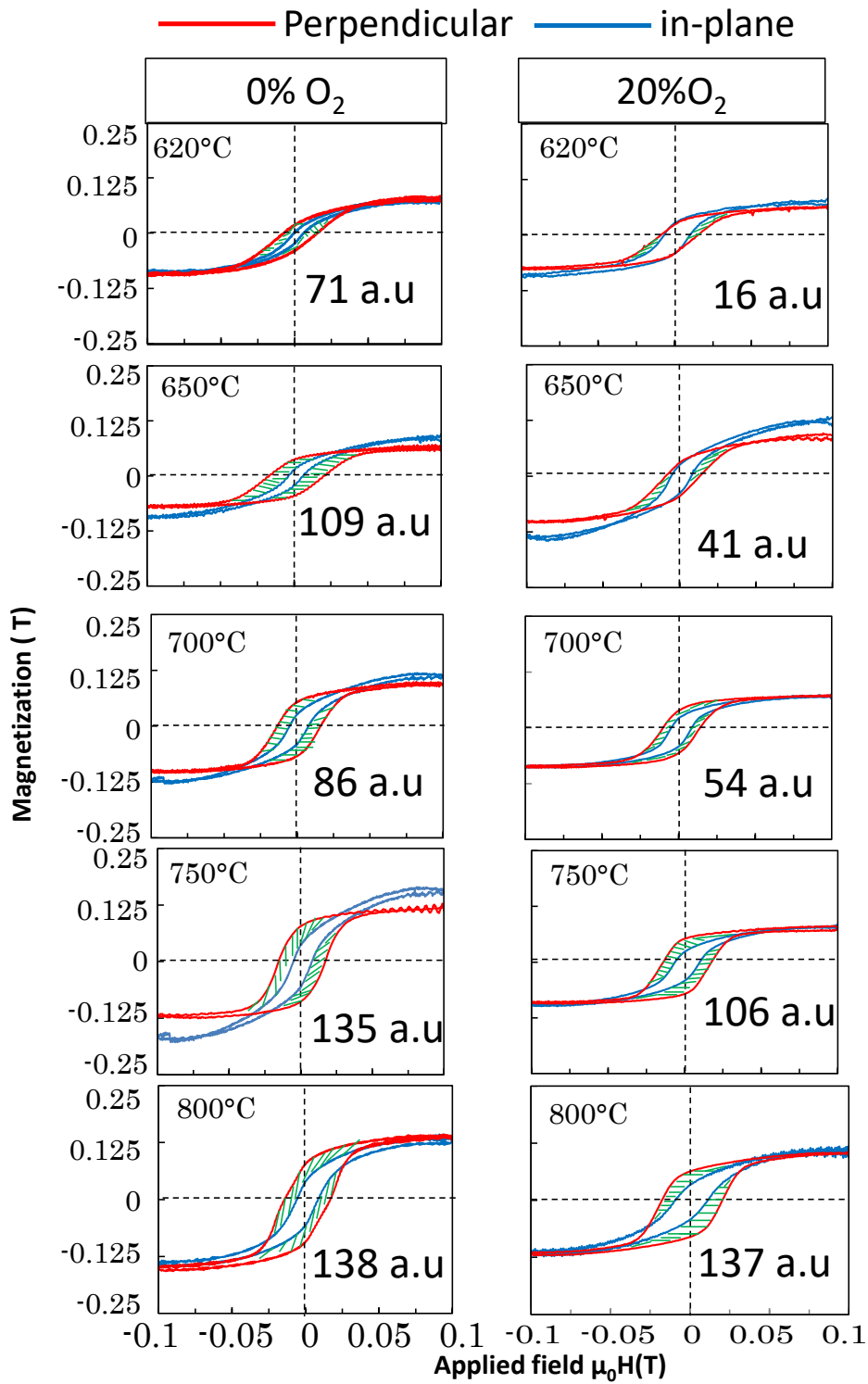
Fig. 4.10 In-plane and perpendicular magnetization curve of the Bi:GdIG samples annealed at 620- 800°C with 20% and 0% O$_2$.
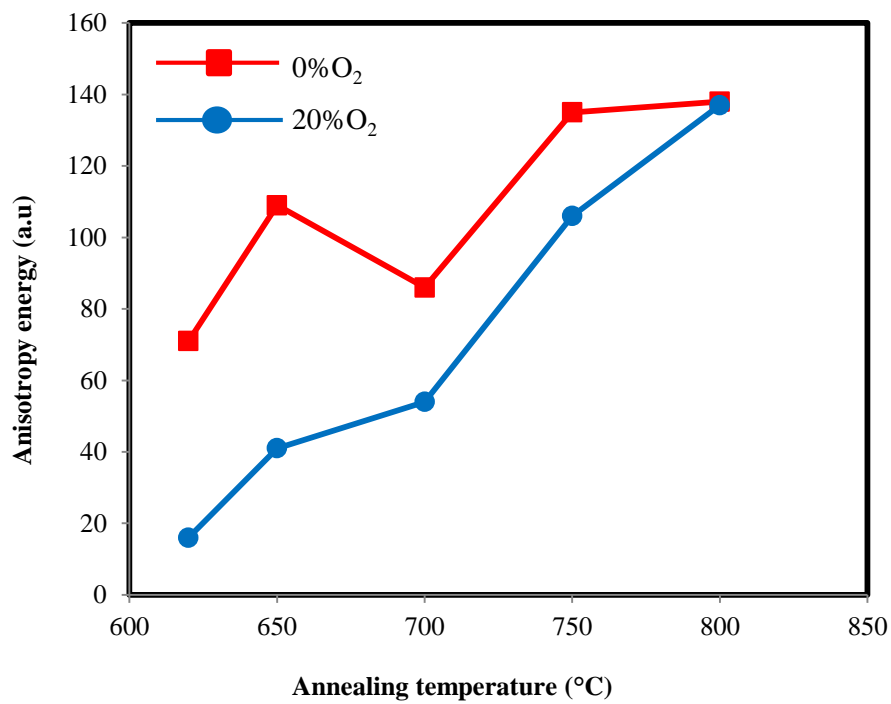
Fig. 4.11 Anisotropy energy of $Bi_1Gd_2Fe_5O_{12}$ at different annealing temperature with annealing gas of $0\%O_2$ and $20\%O_2$.

It was reported that the modulation of the number of 3d electrons caused the change of the magnetic anisotropy in ferromagnetic metal $Fe_{80}Co_{20}$ ultrathin films [4]. It was also reported that the incorporation of O_2 defect in magnetic garnet brings the magnetic anisotropy [5].

Fig. 4.12 Polar-Kerr ellipticity hysteresis curves of a 0.48-nm-thick $Fe_{80}Co_{20}$ thin film on MgO substrate under voltage application of 200 (blue) and _200V (red). The magnetic anisotropy can be control by applying voltage [4].

4.4 Conclusion

We have prepared bismuth substituted gadolinium iron garnet (Bi:GdIG) thin films on (111) GGG substrates by the metal organic decompositio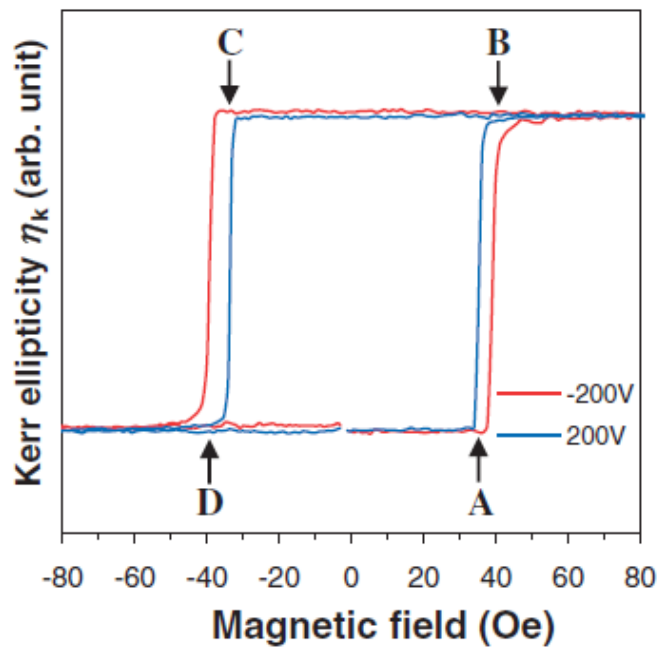n (MOD) method at different annealing temperature (620 – 800℃) and with different annealing gases (20% O_2 and 0% O_2). We characterized the X-ray diffraction (XRD), Faraday effect, optical transmittance and magnetization of the samples. The XRD shows that the Bi:GdIG thin films with high crystalline quality were successfully fabricated. The lattice constant decreased with increasing the final annealing temperature and by changing the annealing gas from 20% O_2 to 0% O_2. The optical transmittance is decreased in the wavelength range of 430 nm and 900 nm, with increasing the final annealing temperature. Faraday rotation increased with increasing final annealing temperature. Magnetization measurements revealed larger perpendicular magnetic anisotropy for the samples annealed at $620 - 650^\circ$C with 0% O_2 and at higher annealing temperature for the samples annealed with 0% O_2 and 20% O_2. The possible reasons of the influence of the annealing conditions on the perpendicular magnetic anisotropy were discussed, including the crystal growth process, and O_2 vacancy defect.

CHAPTER 5

Preparation and Characterization of $Bi_xGd_{3-x}Fe_5O_{12}$ thin films with x = 1 to 2.5 by EMOD method on glass substrate

5.1 Introduction

In this chapter, I discuss on fabrication and characterization of bismuth substituted gadolinium iron garnet thin films ($Bi_xGd_{3-x}Fe_5O_{12}$) with x = 1, 2, and 2.5 on glass substrates by enhanced metal organic decomposition (EMOD) method.

Features of EMOD method is that the solutions can be prepared separately for Bi_2O_3, Gd_2O_3, and Fe_2O_3 so that Bi content x can be selected by changing the mixing ratio of the solutions depending on the target composition. This is a great advantage over conventional MOD method. However there have been no reports on preparation of BiGdIG by EMOD method.

In order to apply Bi:GdIG thin films in MOSLMs [1] and Si / SiO$_2$ based waveguide optical isolators [2-5], it is required that Bi:GdIG thin films are prepared on glass substrates or SiO$_2$ thin films, and it is important to obtain magnetic garnet thin films having large FR and high transparency. However, it is not easy to fabricate Bi:GdIG thin films on glass substrates because of the differences in crystal structure and thermal expansion coefficient between Bi:GdIG and glass substrate. It has been reported that fabrication of Bi substituted rare-earth iron garnet such Bi$_x$Gd$_{3-x}$Fe$_5$O$_{12}$, Bi$_x$Y$_{3-x}$Fe$_5$O$_{12}$, and Bi$_x$Y$_{3-x}$(FeGa)$_5$O$_{12}$ thin films prepared on single crystal gadolinium gallium garnet (GGG) substrates is established because of lattice matching between the garnet and substrate [1-11]. The fabrication of magnetic garnet such as Bi$_{2.5}$Y$_{0.5}$Fe$_5$O$_{12}$ films was reported by using Nd$_2$Bi$_1$Fe$_4$Ga$_1$O$_{12}$ buffer layer on glass substrates by the MOD method, and FR of 13.8 deg./μm at λ = 520 nm was reported [12]. Therefore, fabrication of Bi$_x$Gd$_{3-x}$Fe$_5$O$_{12}$ thin films with various Bi content x and characterization of FR are important, in order to fabricate Bi$_x$Gd$_{3-x}$Fe$_5$O$_{12}$ with high crystalline quality and large FR. In order to investigate the effect of changing the Bi content x and annealing temperature for crystallization on FR of Bi$_x$Gd$_{3-x}$Fe$_5$O$_{12}$ thin films, I fabricated the Bi$_x$Gd$_{3-x}$Fe$_5$O$_{12}$ thin films with x = 1, 2 and 2.5 at different annealing temperatures of 620, 650 and 700°C on glass substrates by the EMOD method. Furthermore, I used the Gd$_3$Fe$_5$O$_{12}$ buffer layer in order to fabricate the Bi$_x$Gd$_{3-x}$Fe$_5$O$_{12}$ thin films with higher bismuth content x = 2.5 for showing larger FR.

X-ray diffraction (XRD), optical transmittance / reflectivity, and Faraday rotation (FR) were measured for characterizations to examine their dependence on annealing temperatures and different amount of Bismuth substitution (x). When Bi$_x$Gd$_{3-x}$Fe$_5$O$_{12}$

thin films were directly prepared on glass substrates, Bi_2O_3 phase were observed by XRD measurements and with increasing Bi content x from 1 to 2, the FR increased from 1.2 to 5.8 deg./μm at the wavelength of 530 nm. FR of $Bi_{2.5}Gd_{0.5}Fe_5O_{12}$ thin films prepared directly on glass substrates were smaller (0.35 deg./μm) than those of $Bi_2Gd_1Fe_5O_{12}$. When $Bi_{2.5}Gd_{0.5}Fe_5O_{12}$ thin films were prepared with annealing temperature of $620^{\circ}C$ with $Gd_3Fe_5O_{12}$ buffer layer on glass substrates, the films showed garnet crystal structure and larger FR, which is 85 % of that of $Bi_{2.5}Gd_{0.5}Fe_5O_{12}$ thin films prepared on (111) $(GdCa)_3(GaMgZr)_5O_{12}$(SGGG) single crystal substrates. These results mean that $Bi_xGd_{3-x}Fe_5O_{12}$ thin films can be prepared on glass substrates with controlled Bi content and FR as high as that prepared on the SGGG substrate by the EMOD method.

5.2 Fabrication and characterization of $Bi_xGd_{3-x}Fe_5O_{12}$ thin films

I fabricated $Bi_xGd_{3-x}Fe_5O_{12}$ thin films with x = 0, 1, 2 and 2.5 at different annealing temperatures of 620, 650 and 700°C on 15 x 15 mm^2 glass substrate, and a $Bi_xGd_{3-x}Fe_5O_{12}$ thin film with x = 2.5 on 12 mm x 12 mm SGGG (111) single crystal substrate and $Gd_3Fe_5O_{12}$ buffer layer / glass substrate by the EMOD method. Table 5.1 shows the summary of the fabricated samples.

The EMOD liquids used in this experiment are SYM-FE05 containing Fe_2O_3 carboxylates, SYM-BI05 containing Bi_2O_3 carboxylates, and SYM-GD01 containing Gd_2O_3 carboxylates by Kojundo Chemical Laboratory so that we could obtain $Bi_xGd_{3-x}Fe_5O_{12}$ thin films with desired Bi content x as shown in Fig. 5.1.

Table 5.1 Summary of $Bi_xGd_{3-x}Fe_5O_{12}$ fabricated samples by EMOD method with various amount of Bi substition x and annealing temperatrue.

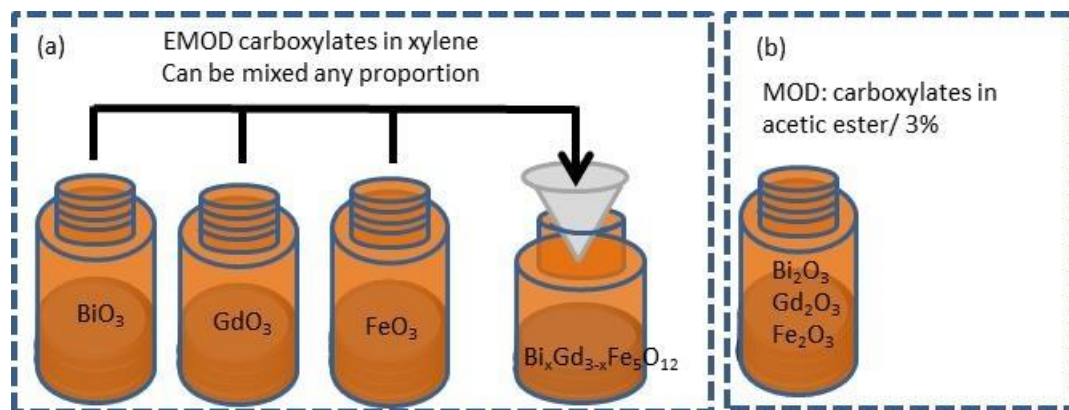| Sample	T_{FA} [$^\circ$ C]	x	substrate
A	650	0	glass
B	620	1	glass
C	650	1	glass
D	700	1	glass
E	620	2	glass
F	650	2	glass
G	700	2	glass
H	620	2.5	glass
I	650	2.5	glass
J	700	2.5	glass
K	620	2.5	GdIG Buffer layer/glass
L	620	2.5	SGGG

Fig. 5.1 (a) EMOD solution can be mixed in any proportion of molar ratio, (b) MOD solution with a fixed molar ratio.

Kojundo Chemical Laboratory Ltd provides their own MOD solutions, as well as EMOD solutions developed by Symetrix Corporation of the United States and Kojundo Chemical Laboratory Ltd [13]. The MOD solution contains 2 –3 kinds of metal oxides

carboxylates such as Bi_2O_3, Gd_2O_3, and Fe_2O_3 carboxylates in acetic ester to prepare $Bi_xGd_{3-x}Fe_5O_{12}$ thin films. Therefore in case of preparation of $Bi_xGd_{3-x}Fe_5O_{12}$ thin films by the MOD method, Bi content x is fixed. On the other hand, the EMOD solution contains one metal oxide carboxylate in xylene and can be mixed with other EMOD solutions containing other metal oxide. Therefore it is possible to prepare the $Bi_xGd_{3-x}Fe_5O_{12}$ thin films in any proportion of Bi content x, which enables greater degree of freedom and more precise control of composition in order to prepare $Bi_xGd_{3-x}Fe_5O_{12}$ thin films. When I prepare the $Bi_xGd_{3-x}Fe_5O_{12}$ thin films with different Bi content x by the EMOD method, the EMOD solutions of Fe_2O_3 carboxylate, Bi_2O_3 carboxylate, and Gd_2O_3 carboxylate are mixed and combined for different Bi content x, which is advantage over the MOD method. The selected components were mixed in the desired stoichiometric ratio of $Bi_xGd_{3-x}Fe_5O_{12}$ with different value of x = 1, 2 and 2.5 and stirred well. The determination procedure of volume for each EMOD solution explained in chapter 3 section 3.3.2. The solution was then filtered by advantec filter paper. The solution was spin-coated in 2 steps process of 500 rpm for 10 s and 2000 rpm for 20 s, followed by drying on a hot plate at 120°C for 10 min and the solvent are evaporated. In order to decompose the organic materials and obtain the amorphous metal oxide films, the samples were pre-annealed at 550°C for 10 min. The thickness by single spin coating step is typically 20 - 30 nm. The conditions for spin coating, drying, and pre-annealing were fixed. I changed the mixing ratio of the SYM-BI05 and SYM-GD01 solutions in order to change the Bi substitution x in $Bi_xGd_{3-x}Fe_5O_{12}$ thin films, and changed the final-annealing temperature. The thickness of the samples slightly changes with the spin coating speed, time and viscosity of the solutions. Spin coating, drying and pre-annealing were repeated for 11 times to obtain an appropriate thickness. Spin

coating, drying and pre-annealing, were repeated 6 times for the $Bi_xGd_{3-x}Fe_5O_{12}$ films on the $Gd_3Fe_5O_{12}$ buffer layer / glass substrate. Also, I prepared a $Bi_xGd_{3-x}Fe_5O_{12}$ film on SGGG (111) single crystal substrate for a reference sample to compare the FR. The amorphous $Bi_xGd_{3-x}Fe_5O_{12}$ films prepared by pre-annealing process were then annealed at 620, 650 and 700 °C for 2 hours for crystallization (final annealing). The pressure during the annealing was atmospheric pressure. Bi:GdIG thin films prepared in this study were characterized by x-ray diffraction (XRD), optical transmittance, optical reflectivity, and FR spectra. All the measurements were done at room temperature. I measured the XRD from the central part of the samples. I estimated the thickness of the samples from the optical reflectivity spectra, and discussed the relationship between crystalline quality and FR by XRD and FR spectra.

5.3 Results and Discussion

Fig. 5.2 shows the optical reflectivity spectra (wavelength λ= 250 -2600 nm) of the $Bi_xGd_{3-x}Fe_5O_{12}$ samples annealed at 620, 650 and 700°C, with the Bi content x=0, 1, 2 and 2.5 on glass substrates. The incident direction of the light was normal to the sample. In order to estimate the thickness of the $Bi_xGd_{3-x}Fe_5O_{12}$ films, I fitted the measured optical reflectivity spectra to reproduce the experimental results by the calculated reflectivity spectra. The detail of the procedure is already described in chapter 3.

The simulated reflectivity spectra showed by dotted lines in Fig. 5.2. The thicknesses were estimated to 170 - 210 nm for the samples with $x = 1$, 200 - 260 nm for the samples with $x = 2$, and 330 - 360 nm for the samples with $x = 2.5$. The viscosity of the solution was increased with increasing the Bi content x. Therefore the film thickness increased with increasing the Bi content x.
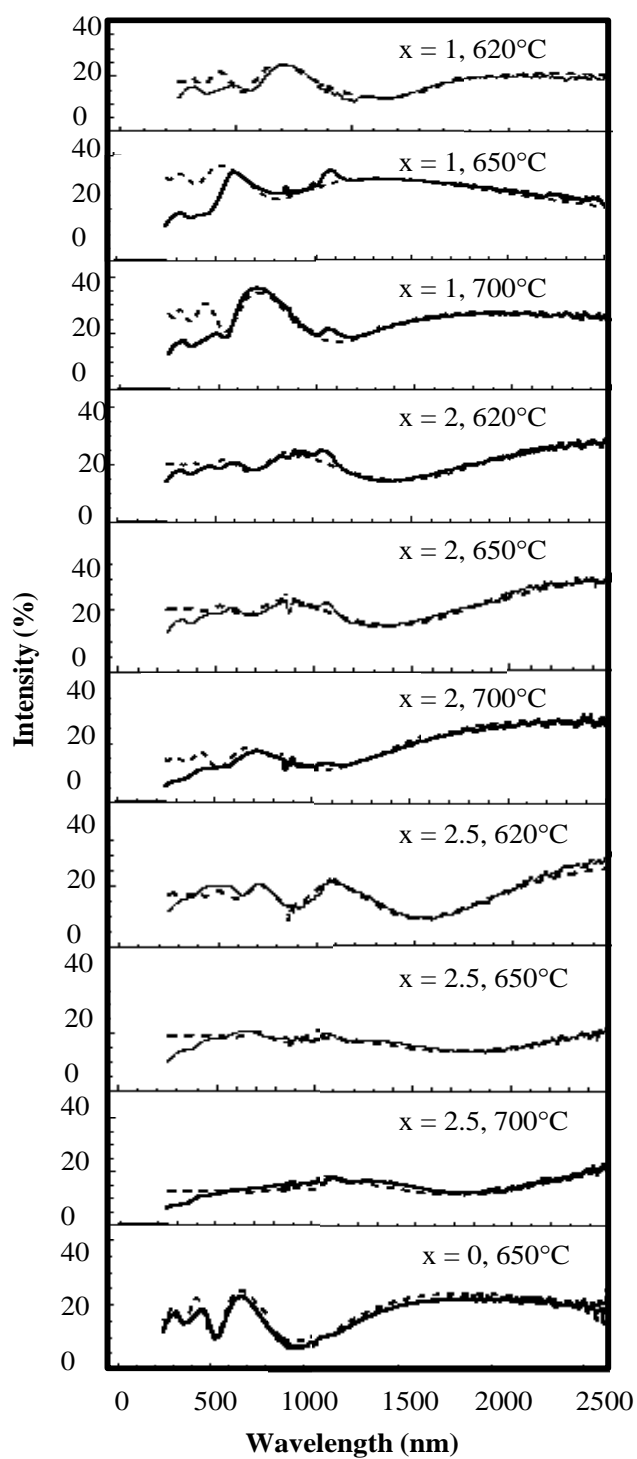
Fig. 5.2 Optical reflectivity spectra (solid lines) of the $Bi_xGd_{3-x}Fe_5O_{12}$ samples annealed at 620, 650 and 700°C, with bismuth content $x = 0$, 1, 2 and 2.5 on glass substrates. The fitted spectra are shown by dashed lines.

Fig. 5.3 shows the XRD spectra of the fabricated samples on glass substrates. The XRD spectra of samples shows some peaks associated with (420) plane of $Bi_xGd_{3-x}Fe_5O_{12}$, (104) plane of Fe_2O_3, (112) plane of Gd_2O_3, (008) plane of ε-Bi_2O_3, (200) plane of BiO_3, (222) plane of β-Fe_2O_3, and (130) plane of ε-Fe_2O_3 phases.

When the Bi_2O_3, Gd_2O_3 and Fe_2O_3 carboxylates are mixed with a molar ratio of 1: 2: 5, and the annealing temperature of 620 – 700 °C directly prepared on the glass substrates, the diffraction signal from Fe_2O_3 is larger than that from $Bi_xGd_{3-x}Fe_5O_{12}$. When the Bi_2O_3, Gd_2O_3 and Fe_2O_3 carboxylates are mixed with a ratio of 2 : 1 : 5 and the annealing temperature of 620 – 650 °C directly prepared on the glass substrates, the diffraction signal from Gd_2O_3 is larger than that from $Bi_xGd_{3-x}Fe_5O_{12}$. When the annealing temperature is 700 °C, the diffraction signal from Bi_2O_3 is increased. When the Bi_2O_3, Gd_2O_3 and Fe_2O_3 carboxylates are mixed with a ratio of 2.5: 0.5: 5 and the annealing temperature of 620 – 700 °C directly prepared on glass substrates, the diffraction signals from Bi_2O_3 and ε-Bi_2O_3 are much more dominant than that from $Bi_xGd_{3-x}Fe_5O_{12}$. The diffraction peak associated with $Bi_xGd_{3-x}Fe_5O_{12}$ were the weakest with x = 2.5 among all the samples without the $Gd_3Fe_5O_{12}$ buffer layer. With increasing the final annealing temperature, the diffraction peak associated with ε-Bi_2O_3 increased. From the XRD spectra of the samples, it is difficult to fabricate Bi:GdIG thin films with high Bi content x = 2.5 directly on glass substrate. In order to solve this problem, I fabricated a gadolinium iron garnet ($Gd_3Fe_5O_{12}$) thin film with the chemical composition of Gd_2O_3:Fe_2O_3 = 3:5 in the mixed solution as a buffer layer for preparation of $Bi_xGd_{3-x}Fe_5O_{12}$ thin films with higher Bi content x of 2.5, with the thickness of 150 nm on the glass substrate at final annealing temperature of 650°C by the EMOD method.

Then I fabricated a $Bi_{2.5}Gd_{0.5}Fe_5O_{12}$ thin film on the $Gd_3Fe_5O_{12}$ buffer layer / glass substrate. The final annealing temperature for $Bi_{2.5}Gd_{0.5}Fe_5O_{12}$ thin film was set at 620°C instead of the annealing temperature of 650°C as shown in Table.5.1. This is because when the final annealing temperature of the $Bi_{2.5}Gd_{0.5}Fe_5O_{12}$ film is the same or higher than the final annealing temperature for the $Gd_3Fe_5O_{12}$ buffer layer/glass sub., the part of crystal structure of the $Gd_3Fe_5O_{12}$ buffer layer can be destroyed [17]. Therefore, I set the final annealing temperature at 620°C for the $Bi_{2.5}Gd_{0.5}Fe_5O_{12}$ film on the $Gd_3Fe_5O_{12}$ buffer layer/glass sub. I mixed the Bi_2O_3, Gd_2O_3 and Fe_2O_3 carboxylates with a ratio of 2.5: 0.5: 5 and annealed at 620 °C with the $Gd_3Fe_5O_{12}$ buffer layer on glass substrate. Fig.5.3 shows the X-ray diffraction of all the samples of $Bi_xGd_{3-x}Fe_5O_{12}$ with and without buffer layer. For the $Bi_{2.5}Gd_{0.5}Fe_5O_{12}$ with $Gd_3Fe_5O_{12}$ buffer layer the diffraction signal from $Bi_xGd_{3-x}Fe_5O_{12}$ is the most dominant and the formation of other phases such as ε-Bi_2O_3, BiO_3 and Gd_2O_3 are suppressed. The diffraction peak associated with β-Fe_2O_3 at the right side of the Bi:GdIG diffraction peak is associated with the $Gd_3Fe_5O_{12}$ buffer layer. From Fig.5.3, it was confirmed that the $Bi_{2.5}Gd_{0.5}Fe_5O_{12}$ thin film having garnet crystal structure was prepared with the buffer layer on glass substrate by the EMOD method.

Summary of Fig.5.3:

a) x = 0 (GdIG buffer layer) → Fe_2O_3 and small amount of $Gd_3Fe_5O_{12}$ are dominant.

b) x = 1 → Fe_2O_3 is dominant.

c) x = 2 → Gd_2O_3 and ε-Bi_2O_3 are dominant.

d) x = 2.5 (without buffer layer) → ε-Bi_2O_3, BiO_3 and Fe_2O_3 are dominant, also with increasing T_{FA}, Bi_2O_3 is increased.

➢ In b), c), and d) small amount of Bi:GdIG is observed.

e) x = 2.5 (with buffer layer) → Bi:GdIG is dominant.

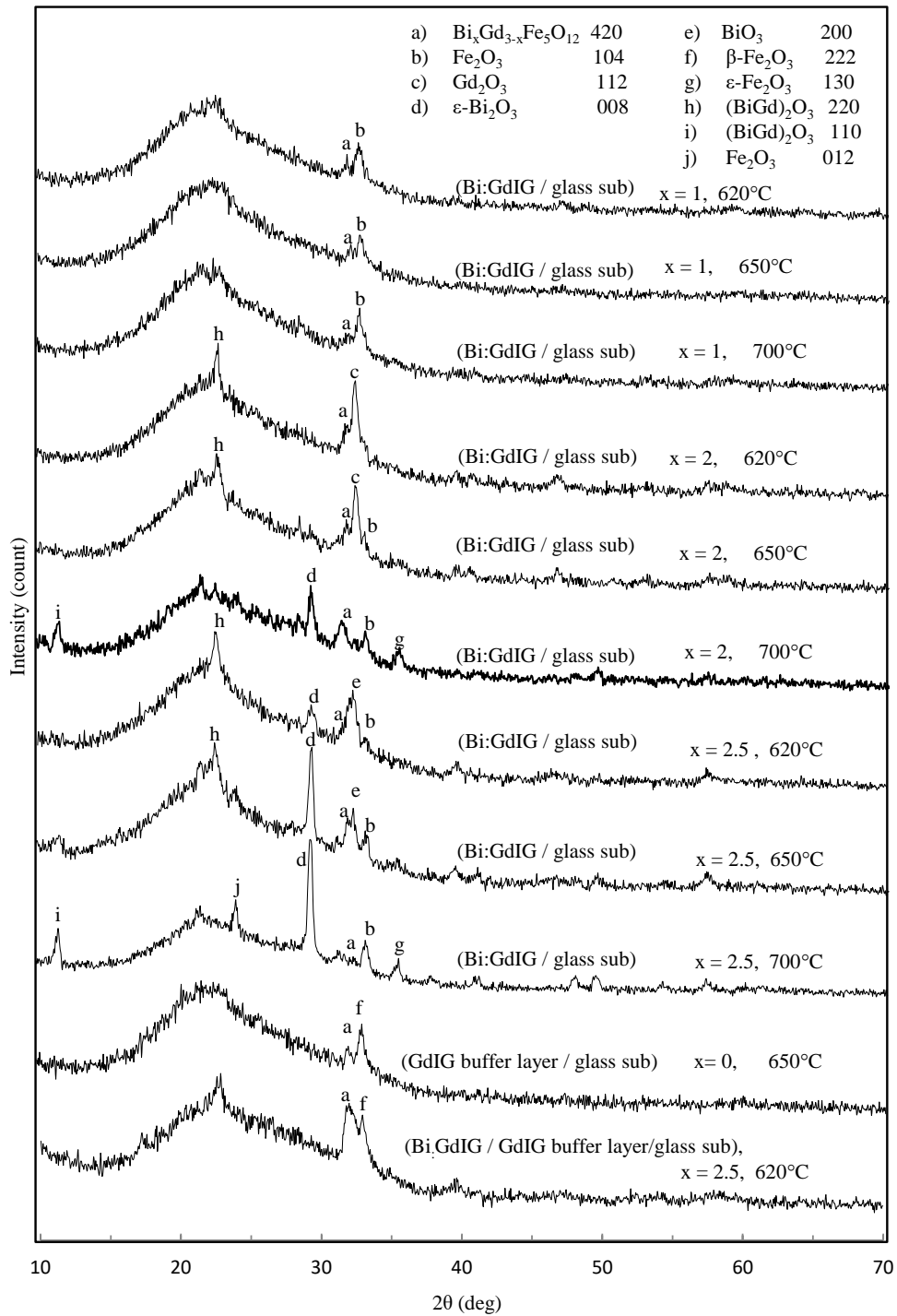|					
a)	$Bi_xGd_{3-x}Fe_5O_{12}$	420	e)	BiO_3	200
b)	Fe_2O_3	104	f)	β-Fe_2O_3	222
c)	Gd_2O_3	112	g)	ϵ-Fe_2O_3	130
d)	ϵ-Bi_2O_3	008	h)	$(BiGd)_2O_3$	220
			i)	$(BiGd)_2O_3$	110
			j)	Fe_2O_3	012

Fig. 5.3 X-ray diffraction of the $Bi_xGd_{3-x}Fe_5O_{12}$ thin films on glass substrate at annealing temperature of 620, 650 and 700°C with $x = 0$, 1, 2 and 2.5 on glass substrates and $Bi_{2.5}Gd_{0.5}Fe_5O_{12}$ on $Gd_3Fe_5O_{12}$ buffer layer/glass substrate.

Fig. 5.4 shows the XRD of the $Bi_{2.5}Gd_{0.5}Fe_5O_{12}$ thin film prepared by the EMOD method on (111) SGGG single crystal substrate. 444 and 888 diffraction peaks are clearly observed and other peaks associated with polycrystalline or impurity phases were not observed. The lattice constant a was calculated to 1.2587 nm. It was reported that the lattice constant of $Bi_{2.5}Gd_{0.5}Fe_5O_{12}$ samples prepared by liquid phase epitaxy (LPE) was 1.259 nm [18], and comparable to that of our $Bi_{2.5}Gd_{0.5}Fe_5O_{12}$ thins films on (111) SGGG substrate. By comparing the lattice constant of the two materials and the results of Fig.5.4, I estimated the composition of our single crystal film by the EMOD method to $Bi_{2.5}Gd_{0.5}Fe_5O_{12}$. Also the diffraction peaks and angles associated with Bi_2O_3, Gd_2O_3, Fe_2O_3, GdIG and BiGdIG of the polycrystalline samples on the glass substrates were confirmed by comparing the lattice spacing d measured by the XRD to the powder diffraction files of international center for diffraction data (ICDD) [19]. Therefore, I estimated the fabricated crystal structure by the EMOD method to the garnet structure.
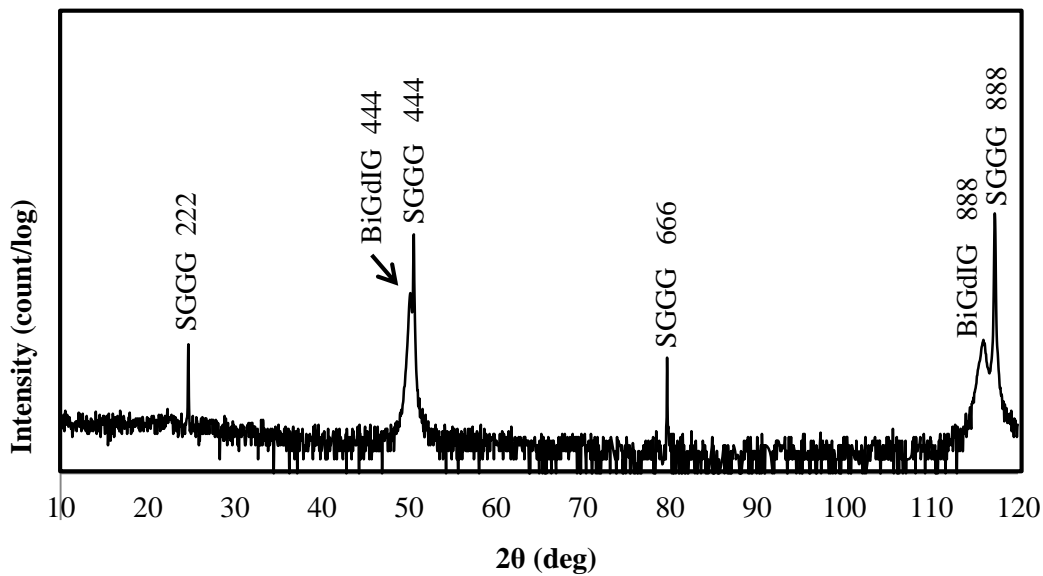
Fig. 5.4 X-ray diffraction of the $Bi_{2.5}Gd_{0.5}Fe_5O_{12}$ thin film annealed at 620℃ on SGGG (111) single crystal substrate. Please note that the vertical axis is in logarithmic scale.
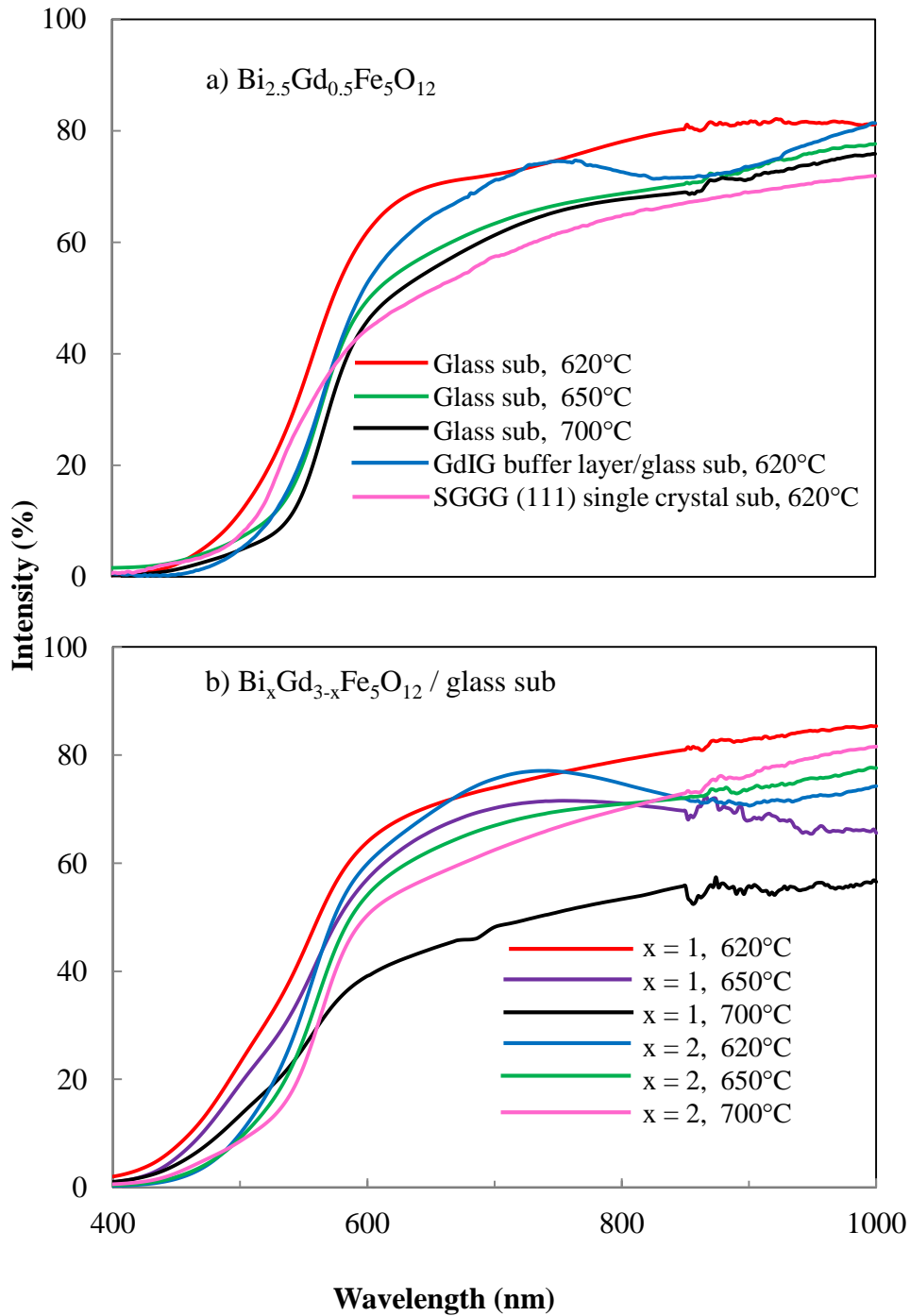
Fig. 5.5 Optical transmittance spectra of the Bi:GdIG samples annealed at 620, 650 and 700 °C, with the bismuth content of a) x= 2.5 on glass, GdIG buffer layer / glass and SGGG (111) single crystal substrates, b) x= 1 and 2 on glass substrates.

Fig. 5.5 shows the optical transmittance spectra of the $Bi_xGd_{3-x}Fe_5O_{12}$ thin films on the glass substrates with / without $Gd_3Fe_5O_{12}$ buffer layer and on glass and (111) SGGG single crystal substrate. The $Bi_{2.5}Gd_{0.5}Fe_5O_{12}$ on the $Gd_3Fe_5O_{12}$ buffer / glass sub has higher transparency in visible and near infrared region, than the $Bi_{2.5}Gd_{0.5}Fe_5O_{12}$ film on (111) SGGG substrate.

Fig. 5.6 shows the FR spectra of the fabricated $Bi_xGd_{3-x}Fe_5O_{12}$ thin films crystallized at 620, 650, and 700 °C with x = 1, 2 and 2.5 on glass substrates. The magnetic field of 1 T was applied perpendicular to the samples in order to fully magnetize the samples.

The samples annealed at 650°C showed larger FR (negative) than the other samples annealed at 620 and 700 °C. Therefore the annealing temperature of 650°C is the optimum condition for crystallization of the BiGdIG thin films on the glass substrate by the EMOD method. The FR of Bi:GdIG increased with increasing x to 2, and decreased in the sample with higher Bi content of x=2.5.
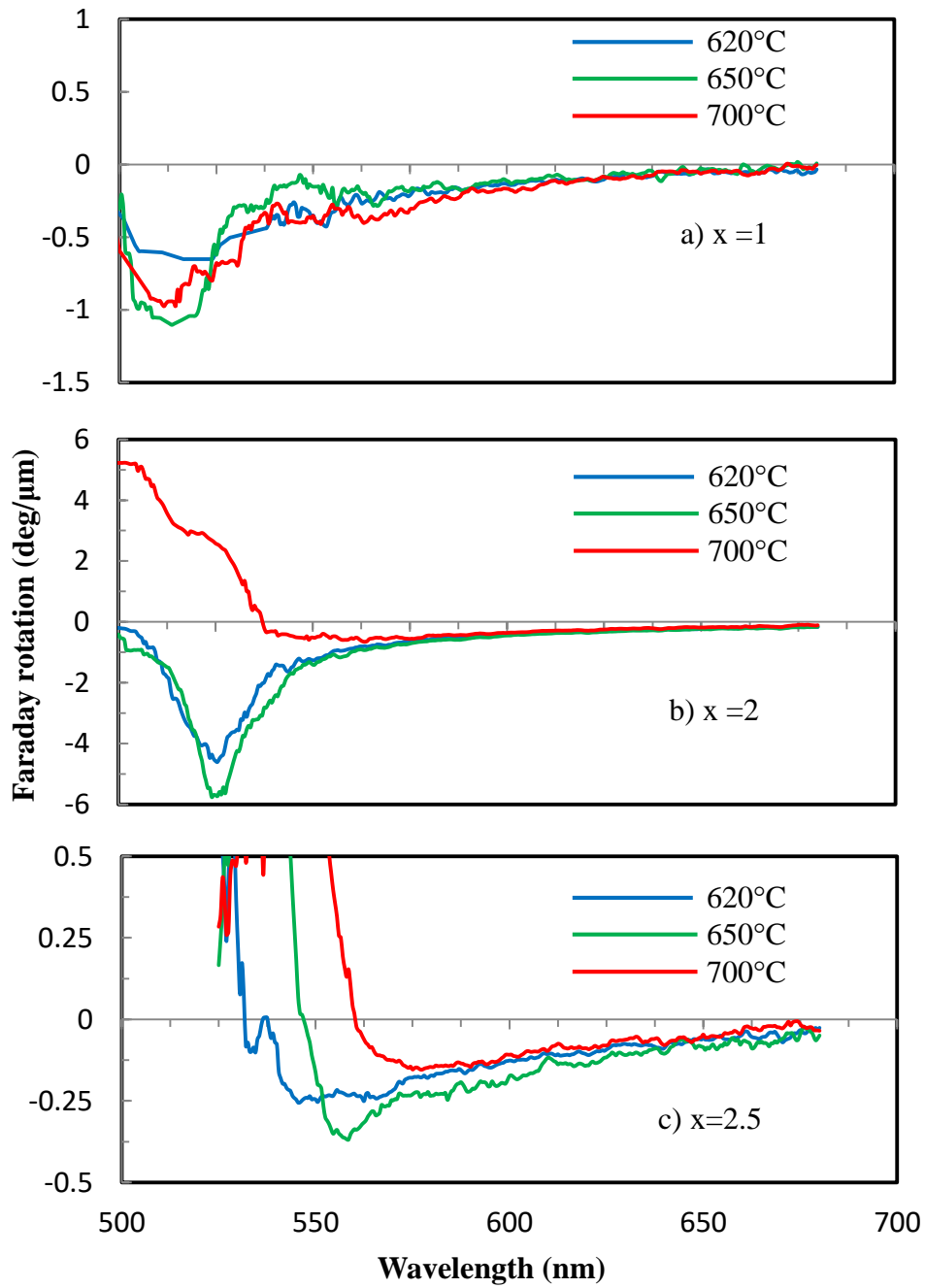
Fig. 5.6 Faraday rotation spectra of the $Bi_xGd_{3-x}Fe_5O_{12}$ samples with different annealing temperatures and bismuth content (a) x= 1, (b) x= 2 and (c) x= 2.5.

Fig. 5.7 shows the FR spectra of the $Bi_{2.5}Gd_{0.5}Fe_5O_{12}$ thin films on the GdIG buffer layer / glass substrate and SGGG (111) single crystal substrate. $Bi_{2.5}Gd_{0.5}Fe_5O_{12}$ thin film on the GdIG buffer layer / glass substrate showed 27.5 deg./µm at the wavelength of 533 nm, which is 55 times larger than $Bi_{2.5}Gd_{0.5}Fe_5O_{12}$ without the GdIG buffer layer in Fig. 5.6 (c). This is because the $Bi_{2.5}Gd_{0.5}Fe_5O_{12}$ thin films with the GdIG buffer layer showed the largest diffraction signal from the $Bi_xGd_{3-x}Fe_5O_{12}$ having garnet structure as shown in Fig. 5.3. On the other hand, the samples without garnet structure including other phases such as Bi_2O_3 and Gd_2O_3 showed little FR, as shown in Fig. 5.3. The presences of the garnet phase lead to larger FR.
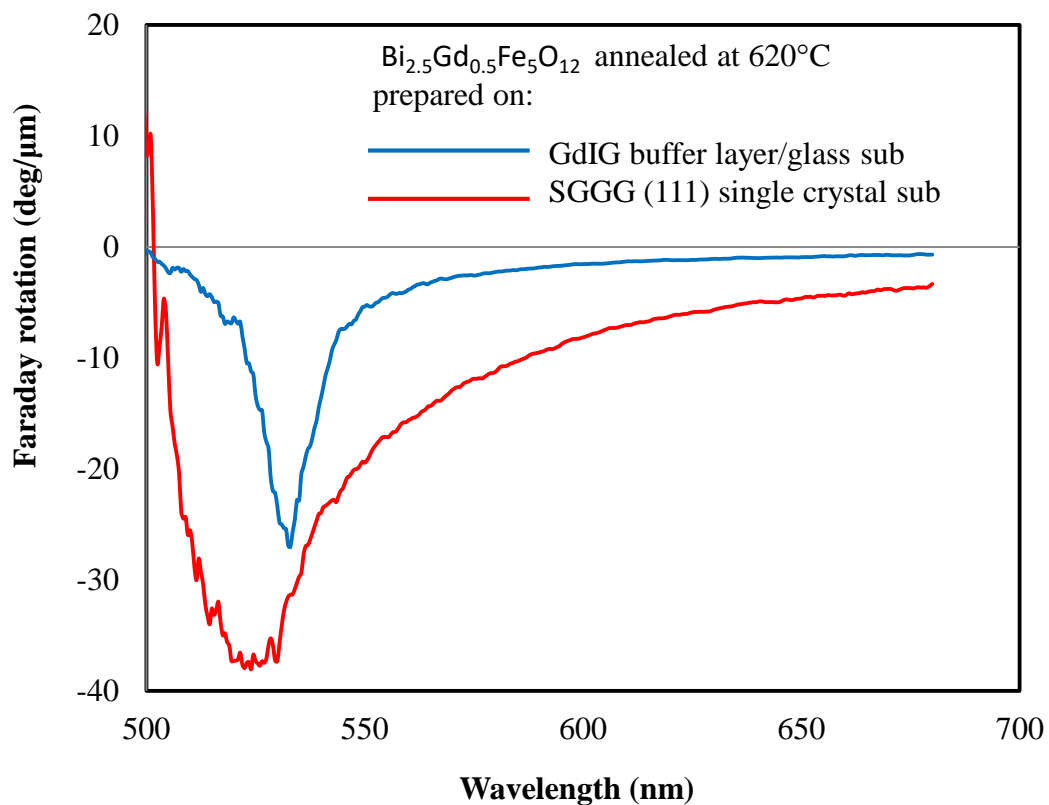

Fig. 5.7 Faraday rotation spectra of the $Bi_{2.5}Gd_{0.5}Fe_5O_{12}$ samples annealed at 620°C with the bismuth content $x= 2.5$ on gadolinium iron garnet buffer layer / glass sub and (111) SGGG single crystal substrate.

Maximum FR (negative) angle of the $Bi_{2.5}Gd_{0.5}Fe_5O_{12}$ thin films on SGGG substrate is 32.5 deg./µm at the wavelength of 533 nm. The maximum FR of the $Bi_{2.5}Gd_{0.5}Fe_5O_{12}$ thin films on the GdIG buffer layer / glass substrate is $(27.5/32.5) \times 100 = 85\%$ of that on (111) SGGG single crystal substrate. It was reported that $Bi_{2.5}Gd_{0.5}Fe_5O_{12}$ films on $Nd_2Bi_1Fe_4Ga_1O_{12}$ buffer layers on a glass substrate by the MOD method showed FR of 13.8 deg./µm at λ = 520 nm, which is half of the FR of our $Bi_{2.5}Gd_{0.5}Fe_5O_{12}$ thin films on the $Gd_3Fe_5O_{12}$ buffer layer / on glass substrate as shown in the magnetic field dependence of the Faraday rotation in Fig. 5.8 [12]. Our sample $Bi_{2.5}Gd_{0.5}Fe_5O_{12}$ with $Gd_3Fe_5O_{12}$ buffer layer on glass substrate by the EMOD method leads to higher FR. The reason for this is probably that our buffer layer does not contain Bi, so they work as good buffer layers.
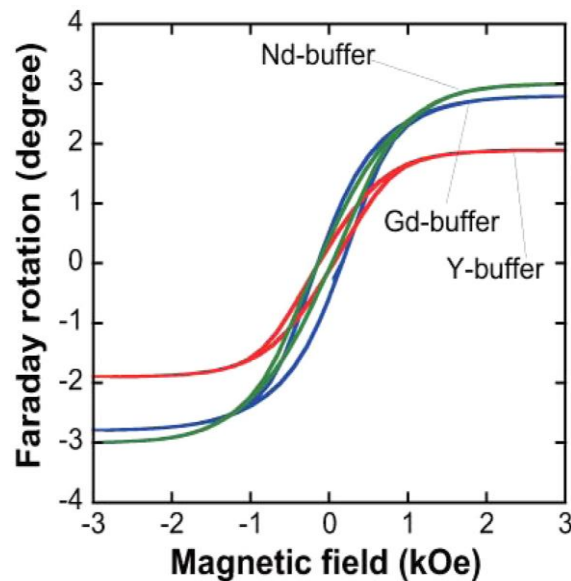
Fig. 5.8 Reported magnetic field dependences of the Faraday rotation of $Bi_{2.5}$:YIG films at the wavelength of 520nm, prepared on $Y_2Bi_1Fe_4Ga_1O_{12}$, $Gd_2Bi_1Fe_4Ga_1O_{12}$ and $Nd_2Bi_1Fe_4Ga_1O_{12}$ buffer layers [12].

Fig. 5.9 shows the magnetic field dependence of the Faraday rotation of $Bi_xGd_{3-x}Fe_5O_{12}$ on glass substrate with x = 1, 2 and 2.5 at different annealing temperature of 620, 650, 700° C.
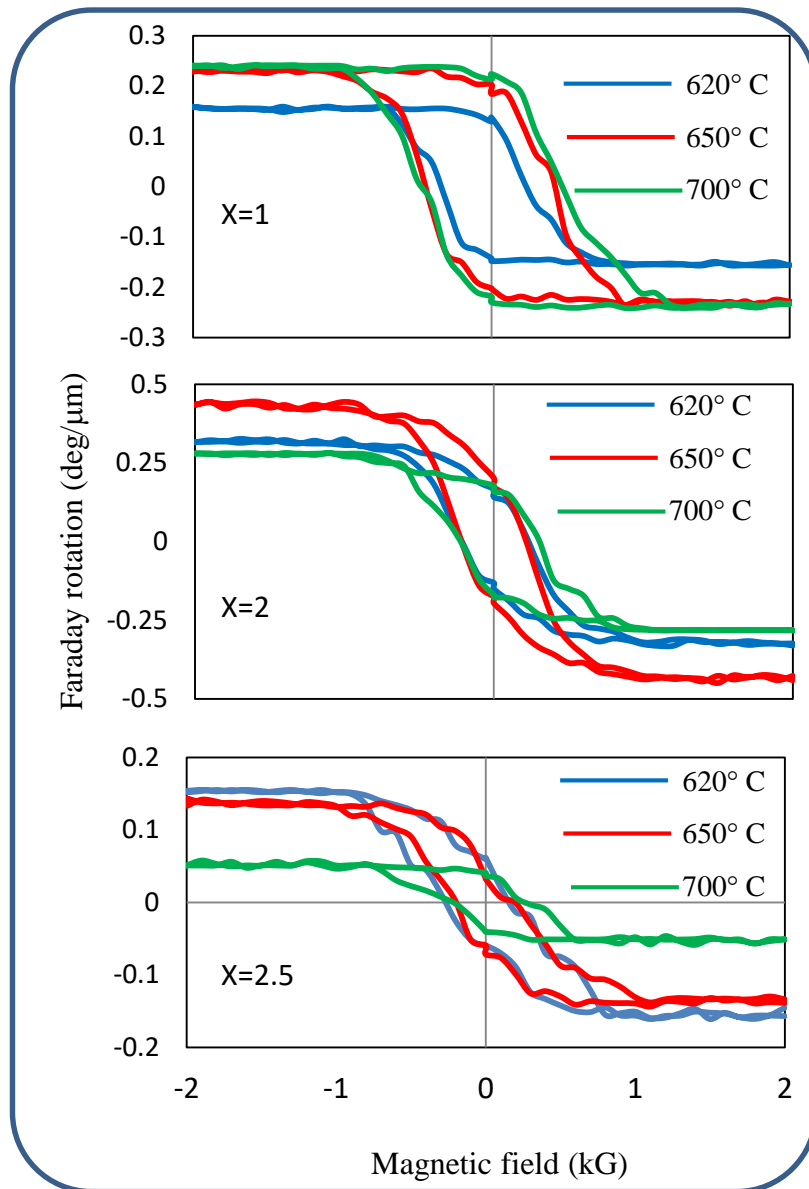
Fig. 5.9 Magnetic field dependences of the Faraday rotation of $Bi_xGd_{3-x}Fe_5O_{12}$ thin films at the wavelength of 600 nm, prepared on glass substrates.

Fig. 5.10 shows magnetic field dependence of the Faraday rotation on $Bi_{2.5}Gd_{0.5}Fe_5O_{12}$ thin films at the wavelength of 600 nm prepared on glass substrate with $Gd_3Fe_5O_{12}$ buffer layer.
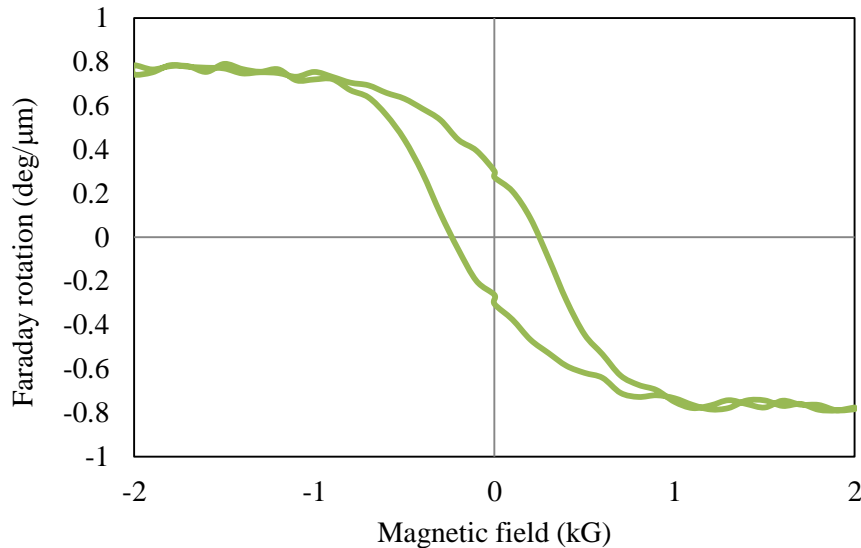
Fig. 5.10 Magnetic field dependences of the Faraday rotation of $Bi_{2.5}Gd_{0.5}Fe_5O_{12}$ thin films at the wavelength of 600 nm, prepared on glass substrate with $Gd_3Fe_5O_{12}$ buffer layer.

Fig. 5.11 shows the images of $Bi_xGd_{3-x}Fe_5O_{12}$ samples with x = 1, 2, and 2.5 under different annealing temperature 620 – 700°C by the EMOD method without $Gd_3Fe_5O_{12}$ buffer layer on glass substrate taken by a digital camera. The main problem of the EMOD method is that the surfaces of these samples are slightly hazy and some precipitates are formed. With increasing the annealing temperature or increasing the amount of Bi (*x*), the surface of the sample become hazier.

Fig. 5.12 shows the optical microscopic images of $Bi_xGd_{3-x}Fe_5O_{12}$ samples with x = 1, 2, and 2.5 under different annealing temperature 620 – 700°C by the EMOD method without $Gd_3Fe_5O_{12}$ buffer layer on glass substrate.
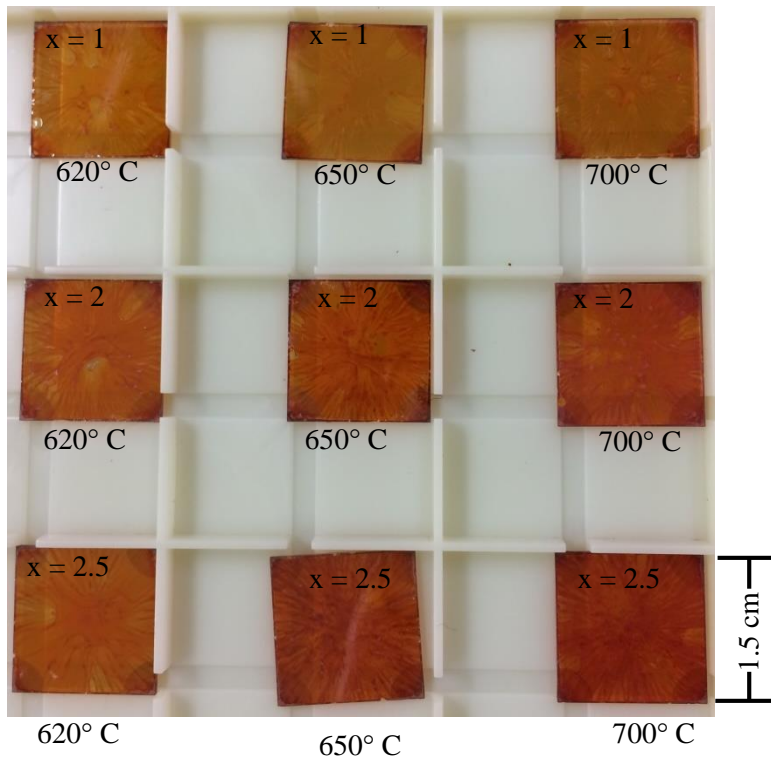
Fig. 5.11 Image of $Bi_xGd_{3-x}Fe_5O_{12}$ on glass substrate taken by digital camera.
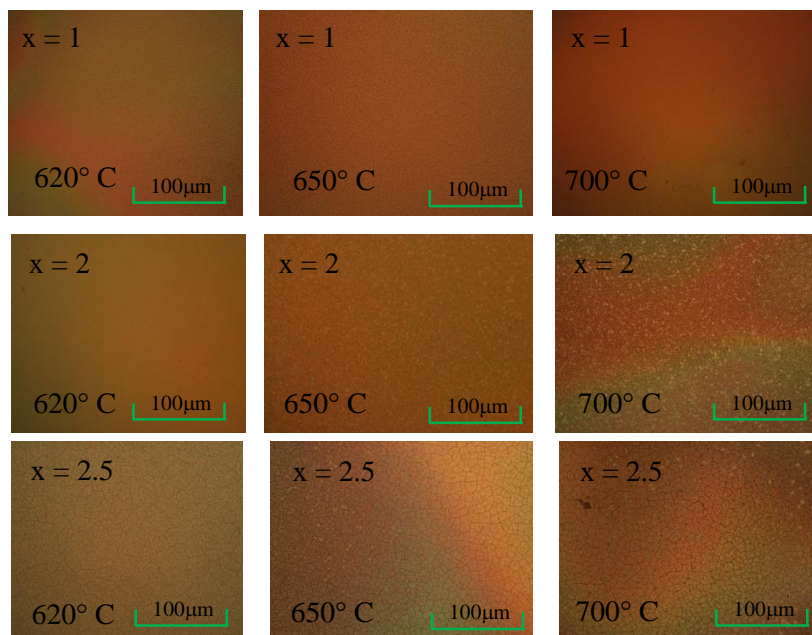
Fig. 5.12. Optical microscopic image of $Bi_xGd_{3-x}Fe_5O_{12}$ thin films with different amount of Bi substitution (x) under different annealing temperature (620-700° C) on glass substrate.

Fig. 5.13 shows the images taken by digital camera of $Bi_{2.5}Gd_{0.5}Fe_5O_{12}$ thin films on (111) SGGG substrate and on glass substrate using $Gd_3Fe_5O_{12}$ buffer layer. The surfaces of the samples are slightly hazy.

(a)   (b)
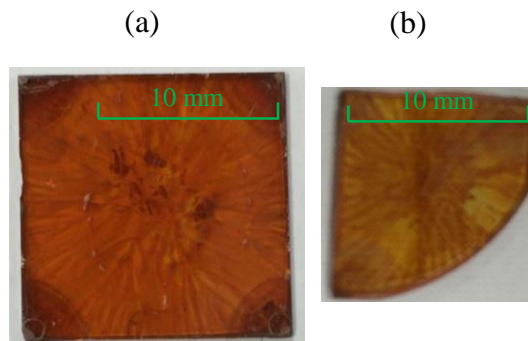
Fig. 5.13 Images taken by digital camera of $Bi_{2.5}Gd_{0.5}Fe_5O_{12}$ thin films (a) on glass substrate using $Gd_3Fe_5O_{12}$ buffer layer (b) on (111) SGGG substrate.

5.4. Conclusion

I have prepared $Bi_xGd_{3-x}Fe_5O_{12}$ thin films on glass substrates, with and without $Gd_3Fe_5O_{12}$ buffer layer on glass substrates and (111) SGGG single crystal substrate by the EMOD method. I characterized the XRD, FR and optical transmittance spectra of the samples. The optimum condition (annealing temperature) for crystallization of $Bi_xGd_{3-x}Fe_5O_{12}$ on the glass substrate is 650° C from FR measurement. From the XRD spectra, the $Bi_{2.5}Gd_{0.5}Fe_5O_{12}$ samples on the $Gd_3Fe_5O_{12}$ buffer layer were successfully fabricated on the glass substrates without forming Bi_2O_3 and Gd_2O_3 phases, which are observed in samples without $Gd_3Fe_5O_{12}$ buffer layer. Furthermore, larger Faraday rotation (27.9deg./μm at $\lambda = 533$ nm) was obtained on the $Bi_{2.5}Gd_{0.5}Fe_5O_{12}$ sample with the $Gd_3Fe_5O_{12}$ buffer layer, which is 55 time larger than $Bi_{2.5}Gd_{0.5}Fe_5O_{12}$ without $Gd_3Fe_5O_{12}$ buffer layer in Fig.5.6, and the Faraday rotation is 85% of that prepared on (111) SGGG single crystal substrate. It is important to suppress the formation of the Bi_2O_3 and Gd_2O_3 phases by the $Gd_3Fe_5O_{12}$ buffer layer in order to prepare $Bi_xGd_{3-x}Fe_5O_{12}$ thin films having higher Bi content *x* and FR, from the XRD spectra and measurement of the Faraday rotation. These findings are important to realize $Bi_xGd_{3-x}Fe_5O_{12}$ thin films having large Faraday rotation with perpendicular magnetic anisotropy for future applications to MOSLMs and optical isolators on the glass substrates.

CHAPTER 6

Preparation of $Bi_2Gd_1Fe_5O_{12}$ thin films using $Gd_3Fe_5O_{12}$ buffer layer on glass substrates by MOD method

6.1. Introduction

In this chapter, I will explain and discuss on fabrication and characterization of $Bi_2Gd_1Fe_5O_{12}$ thin films on glass substrates with the $Gd_3Fe_5O_{12}$ buffer layer by the metal organic decomposition (MOD) method.

In chapter 5, I fabricated $Bi_{2.5}Gd_{0.5}Fe_5O_{12}$ thin film on glass substrates by using $Gd_3Fe_5O_{12}$ buffer layer. However, the surface of the samples depends on the mixed EMOD solution. There is a tendency that with increasing the Bi content, the surface of the sample becomes slightly hazy. Therefore I thought that $Bi_xGd_{3-x}Fe_5O_{12}$ thin films having large FR and good surface morphology are necessary, so that I applied the idea of buffer layer to MOD method.

I obtained FR of 27.5 deg./μm at the wavelength $\lambda = 533$ nm in $Bi_{2.5}Gd_{0.5}Fe_5O_{12}$ samples with $Gd_3Fe_5O_{12}$ buffer layer by using EMOD method. So far, the fabrication conditions of the $Gd_3Fe_5O_{12}$ buffer layer; especially, the thickness of the $Gd_3Fe_5O_{12}$ buffer layer and crystallization temperature have not been fully optimized. When the buffer layer thickness is small, the crystallization of the Bi:GdIG thin films is not enough to show large FR. On the other hand, when the buffer layer thickness is large, magneto-optical contribution to the optical waveguide becomes small, and the optical transparency becomes small. Therefore, it is necessary to realize Bi:GdIG thin films showing large FR by using the buffer layer with minimum thickness. In this chapter I discuss on optimization of the thickness and annealing temperature for crystallization of the $Gd_3Fe_5O_{12}$ buffer layer in order to maximize the FR of the $Bi_2Gd_1Fe_5O_{12}$ thin films on glass substrates. I fixed the thickness $d_{Bi:GdIG}$ and fabrication conditions for Bi:GdIG thin films ($d_{Bi:GdIG}$ =115 nm, and annealed at 620°C for 2 hours under air at atmospheric pressure). I changed the GdIG buffer layer thickness from 0 to 880 nm, by increasing the spin-coating times of the GdIG layer (0 to 8 times). With fixed annealing condition of 650° C for 2 hours.

For comparison, I prepared a Bi:GdIG single crystal film on (111) $(GdCa)_3(GaMgZr)_5O_{12}$ (SGGG) single crystal substrate. The film thicknesses of all layers were estimated from the measured optical reflectivity spectra. I discuss the crystallization process and relationship between the crystalline quality and FR among various preparation conditions for $Gd_3Fe_5O_{12}$ buffer layer. I compared the FR and crystalline properties by X-ray diffraction (XRD). I found an optimum thickness of the $Gd_3Fe_5O_{12}$ buffer layer and annealing temperature for crystallization giving the

maximum Faraday rotation. The optimum sample showed Faraday rotation of as high as 36.3 deg./μm at the wavelength $\lambda = 500$ nm, which is 23 times larger than the sample without the $Gd_3Fe_5O_{12}$ buffer layer, and as high as 90.1 % of the single crystalline $Bi_2Gd_1Fe_5O_{12}$ thin films on an (111) SGGG single crystal substrate. These results are promising for applications in optical waveguide isolators and magneto-optic spatial light modulators.

6.2 Fabrication of GdIG and Bi:GdIG thin films

First, I fabricated the $Gd_3Fe_5O_{12}$ thin films on 15 mm x 15 mm glass substrates by the MOD method in order to investigate the crystalline quality of the $Gd_3Fe_5O_{12}$ films as the buffer layer. I prepared the $Gd_3Fe_5O_{12}$ thin films by changing the spin-coating time in the range of 2, 3, 4, 6, and 8 at fixed final-annealing temperature (T_{FA}) of 650°C. Then I changed the annealing temperature in the range of 620, 650, 700, 750 °C with fixed spin-coating time of 3. Then I fabricated $Bi_2Gd_1Fe_5O_{12}$ thin film with the $Gd_3Fe_5O_{12}$ buffer layer. I also fabricated the $Bi_2Gd_1Fe_5O_{12}$ thin films directly on a glass substrate without buffer layer. The MOD liquids used in this experiment consists of solutions made from Bi_2O_3, Gd_2O_3, and Fe_2O_3 carboxylates in acetic ester with chemical composition ratio of $Bi_2O_3:Gd_2O_3:Fe_2O_3 = 2:1:5$ for $Bi_2Gd_1Fe_5O_{12}$ main layer, and 0:3:5 for $Gd_3Fe_5O_{12}$ buffer layer by Kojundo Chemical Laboratory. I fixed the fabrication conditions for the $Bi_2Gd_1Fe_5O_{12}$ main layer. The fabrication procedure was as follows. Two steps spin-coating process was done with 500 rpm for 10 s and 2000 rpm for 20 s, followed by drying on a hot plate at 120 °C for 10 min, so that the solvent are dissolved. In order to decompose the organic materials and obtain the amorphous metal oxide films, the samples were pre-annealed at 550 °C for 10 min. The conditions for spin coating, drying, and pre-annealing were fixed for all the samples. The $Gd_3Fe_5O_{12}$ buffer layers were then annealed at T_{FA} = 620 - 750 °C for 2 hours (final annealing). I fixed the spin-coating time and final annealing conditions for $Bi_2Gd_1Fe_5O_{12}$ thin films to 6 and 620°C for 2 hours. For comparison, I prepared a $Bi_2Gd_1Fe_5O_{12}$ single crystal film without the $Gd_3Fe_5O_{12}$ buffer layer on a (111) SGGG single crystal substrate at annealing temperature of 620 °C for 2 hours. All the samples were fabricated under air at atmospheric pressure. Table 6.1 shows the summary of the samples for this study.

Table 6.1 The summary of the fabrication conditions for $Gd_3Fe_5O_{12}$ and $Bi_2Gd_1Fe_5O_{12}$ layers in this study.

Sample	Main Layer	Spin coating time	T_{FA} [°C]	Substrate	Buffer layer
B'	$Gd_3Fe_5O_{12}$	2	650	glass	-
C'	$Gd_3Fe_5O_{12}$	3	650	glass	-
D'	$Gd_3Fe_5O_{12}$	4	650	glass	-
E'	$Gd_3Fe_5O_{12}$	6	650	glass	-
F'	$Gd_3Fe_5O_{12}$	8	650	glass	-
A	$Bi_2Gd_1Fe_5O_{12}$	6	620	glass	-
B	$Bi_2Gd_1Fe_5O_{12}$	6	620	glass	B'
C	$Bi_2Gd_1Fe_5O_{12}$	6	620	glass	C'
D	$Bi_2Gd_1Fe_5O_{12}$	6	620	glass	D'
E	$Bi_2Gd_1Fe_5O_{12}$	6	620	glass	E'
F	$Bi_2Gd_1Fe_5O_{12}$	6	620	glass	F'
G'	$Gd_3Fe_5O_{12}$	3	620	glass	-
H'	$Gd_3Fe_5O_{12}$	3	700	glass	-
I'	$Gd_3Fe_5O_{12}$	3	750	glass	-
G	$Bi_2Gd_1Fe_5O_{12}$	6	620	glass	G'
H	$Bi_2Gd_1Fe_5O_{12}$	6	620	glass	H'
I	$Bi_2Gd_1Fe_5O_{12}$	6	620	glass	I'
J	$Bi_2Gd_1Fe_5O_{12}$	6	620	SGGG	-

6.3 Characterization

First I measured the optical reflectivity spectra of the $Gd_3Fe_5O_{12}$ thin films on glass substrates (B'-F') and $Bi_2Gd_1Fe_5O_{12}$ thin films without the $Gd_3Fe_5O_{12}$ buffer layer on a glass substrate (A) and SGGG substrate (J) in order to estimate the thickness of these films. The measurement wavelength range is from 250 to 2600 nm. The direction of the incident light was normal to the sample. Fig. 6.1 shows the optical reflectivity spectra of these samples. I fitted the measured optical reflectivity spectra by the calculated reflectivity spectra. I calculated the reflectivity spectra by considering the multiple reflections inside the films by interfaces between air / film and film / substrate [7 - 9]. Detail of the estimation process was described in chapter 3. The simulated reflectivity spectra are shown by dotted lines in Fig.6.1. The thicknesses were estimated to 115 nm, and 105 nm for Sample A and J ($Bi_2Gd_1Fe_5O_{12}$ thin films without the $Gd_3Fe_5O_{12}$ buffer layer).

The thicknesses are estimated to 133, 286, 320, 533, and 729 nm for Sample B'-F' respectively, and summarized in Fig. 6.2. The thickness obtained by single spin-coating process was estimated to 19.2 and 17.5 nm for Sample A and J where the MOD solution of $Bi_2Gd_1Fe_5O_{12}$ films was used.
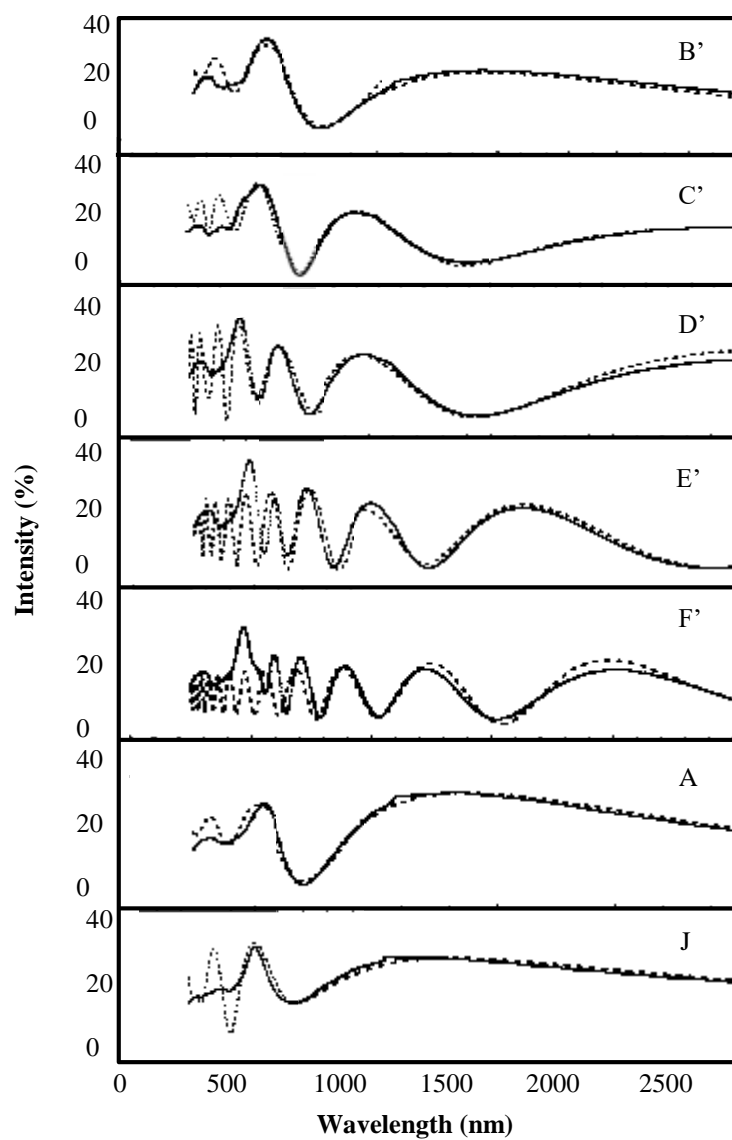
Fig. 6.1 Optical reflectivity spectra (solid lines) of the $Gd_3Fe_5O_{12}$ thin films (B'-F') on glass substrates, $Bi_2Gd_1Fe_5O_{12}$ thin films without the $Gd_3Fe_5O_{12}$ buffer layer on glass substrate (A) and SGGG substrate (J). The fitted spectra are shown by dashed lines.

136
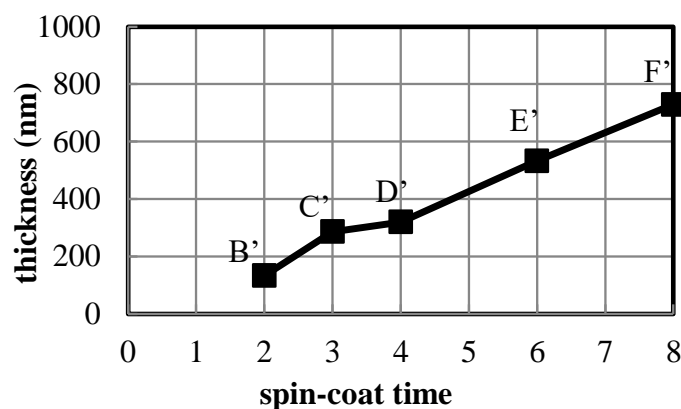
Fig. 6.2 Estimated thicknesses of the $Gd_3Fe_5O_{12}$ layers as a function of
the spin-coating time.

On the other hand, the average thickness obtained by single spin-coating process
was estimated to 84.4 nm for B'-F', where the MOD solution of the $Gd_3Fe_5O_{12}$ was
used. This is because viscosity of the MOD solution for the $Gd_3Fe_5O_{12}$ was higher than
that for the $Bi_2Gd_1Fe_5O_{12}$ films. I measured the x-ray diffraction (XRD) of all the
samples. Figs. 6.3 and 6.4 show the XRD of the $Gd_3Fe_5O_{12}$ thin films (B'-I') and
$Bi_2Gd_1Fe_5O_{12}$ thin films (A-I). The symbols a, b, and c in Figs.6.3, and 6.4 correspond
to the diffraction angles from (420), (422), (400) planes of $Bi_2Gd_1Fe_5O_{12}$ phases. The
symbols d, and d' correspond to (420), (422), planes of $Gd_3Fe_5O_{12}$ phase. The symbols
e, f, and h correspond to (112) plane of Gd_2O_3 phase, (104) planes of β-Fe_2O_3 and α-
Fe_2O_3 phases.
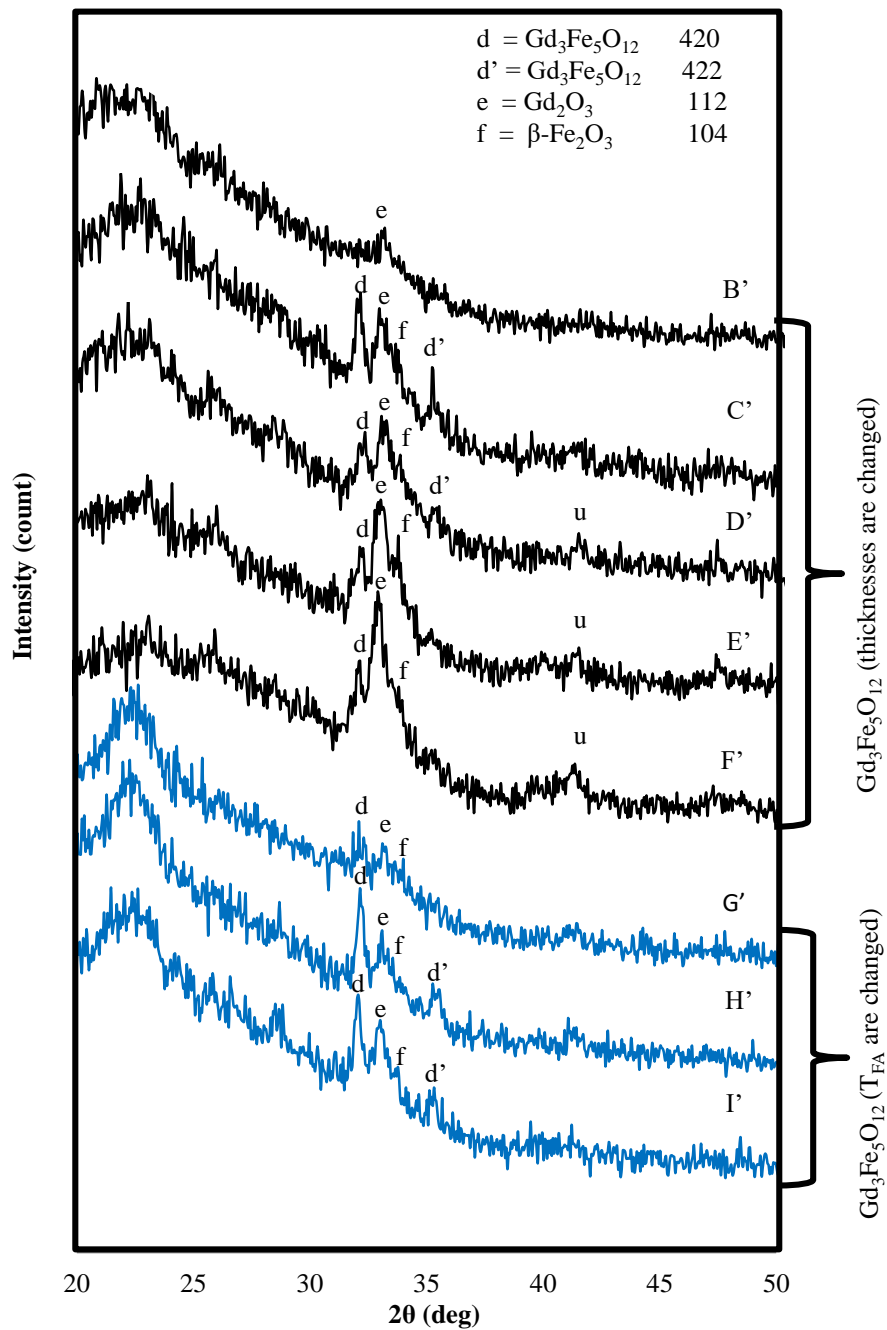
Fig. 6.3 X-ray diffraction of the $Gd_3Fe_5O_{12}$ thin films (Samples B'-I') on glass substrate.
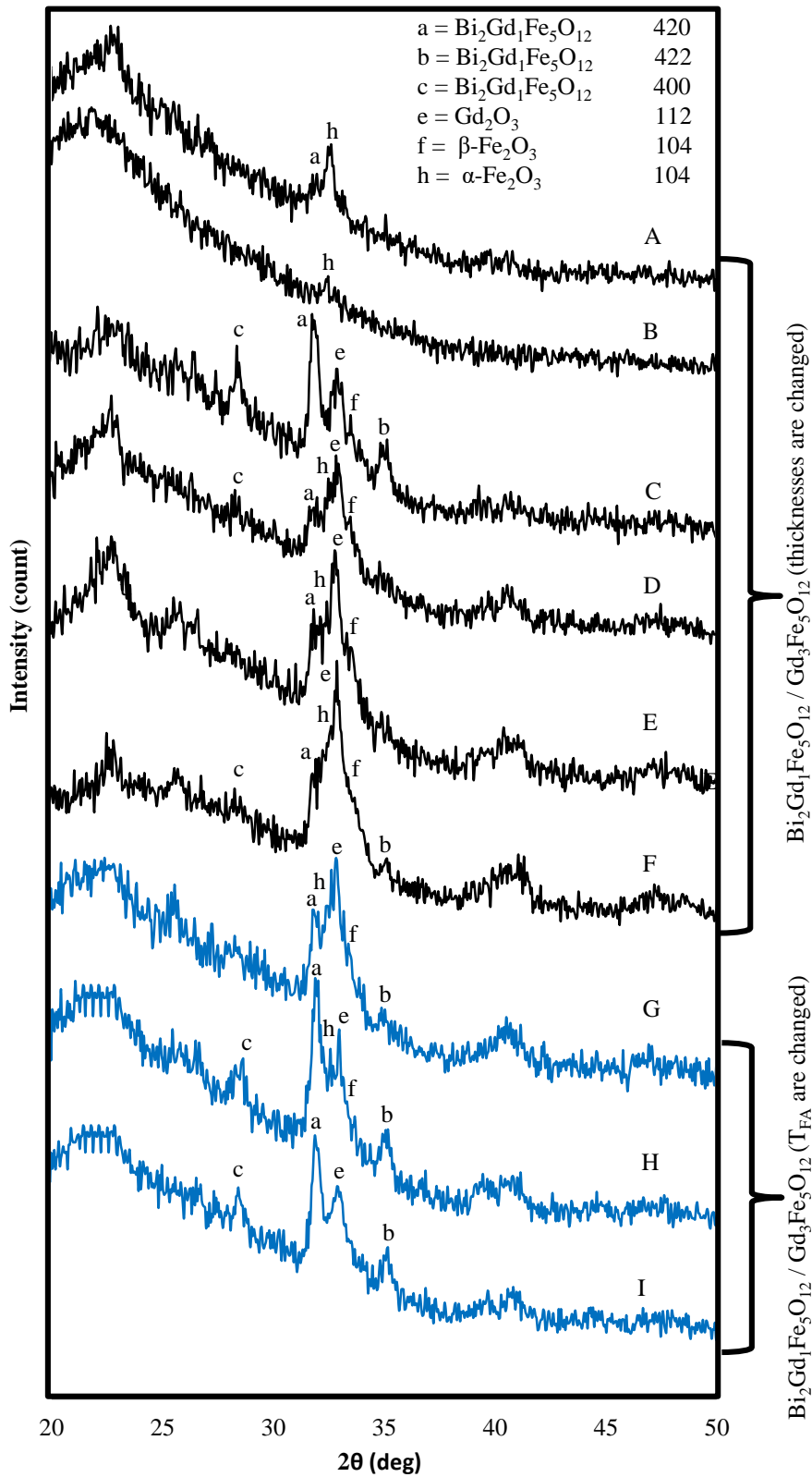
Fig. 6.4 X-ray diffraction of the $Bi_2Gd_1Fe_5O_{12}$ thin films (Samples A-I) on glass substrates with and without the $Gd_3Fe_5O_{12}$ buffer layer.

These identifications are based on the powder diffraction file of international center for diffraction data (ICDD). It was reported that the lattice constant of $Bi_2Gd_1Fe_5O_{12}$ samples prepared by liquid phase epitaxy (LPE) was 1.2565 nm [25]. I assumed the lattice constant of 1.2565 nm to identify the lattice spacing of the $Bi_2Gd_1Fe_5O_{12}$. The XRD of the $Gd_3Fe_5O_{12}$ thin films in Fig. 6.3 shows several peaks associated with (420) and (422) planes of $Gd_3Fe_5O_{12}$, (112) plane of Gd_2O_3, (104) plane of β-Fe_2O_3. I found that the $Gd_3Fe_5O_{12}$ phase are not fabricated and small amount of the Gd_2O_3 is observed in Sample B' with spin-coating times of 2. When the spin-coating times is 3 (C'), the $Gd_3Fe_5O_{12}$ phase are the most dominant among the samples B'-F' with different spin-coating time and fixed final-annealing temperature of 650 ℃.

When the spin-coating time is larger than 4, the ratio of the $Gd_3Fe_5O_{12}$ phase on the Gd_2O_3 phase became smaller. On the other hand the samples H' and I' annealed at 700 and 750 ℃ showed larger signal from the $Gd_3Fe_5O_{12}$ phase than Sample C' and G' annealed at lower temperature of 650 and 620 ℃. Therefore optimum samples are H' and I'. From Fig.6.4, the diffraction peak associated with $Bi_2Gd_1Fe_5O_{12}$ was the weakest in Sample A without the $Gd_3Fe_5O_{12}$ buffer layer among A-I except for B having the thinnest $Gd_3Fe_5O_{12}$ buffer layer. The diffraction peak associated with the $Bi_2Gd_1Fe_5O_{12}$ was not observed in B. This is because the amorphous $Gd_3Fe_5O_{12}$ layer did not work as a buffer layer as shown in B' in Fig.6.3. The diffraction signals from the $Bi_2Gd_1Fe_5O_{12}$, Gd_2O_3, α-Fe_2O_3 and β-Fe_2O_3 were observed in Samples C-I. When the spin-coating time for the $Gd_3Fe_5O_{12}$ buffer layer was 3, the diffraction signal from $Bi_2Gd_1Fe_5O_{12}$ was the largest and signal from Gd_2O_3 was the smallest among samples with different spin-coating time of the $Gd_3Fe_5O_{12}$ buffer layer (B - F). The samples G showed the smallest signal from the $Bi_2Gd_1Fe_5O_{12}$ phase and largest signal from the

Gd$_2$O$_3$, α-Fe$_2$O$_3$ and β-Fe$_2$O$_3$ phases among the samples C, G, H, and I with the same Gd$_3$Fe$_5$O$_{12}$ buffer layer thickness and different annealing temperature of 620 -750 $^{\circ}$C. The sample C, H, and I showed the larger diffraction signal from Bi$_2$Gd$_1$Fe$_5$O$_{12}$ among samples A - I. The diffraction signals from α-Fe$_2$O$_3$ and β-Fe$_2$O$_3$ were not observed in sample I. Therefore, sample I is the optimum condition to prepare Bi$_2$Gd$_1$Fe$_5$O$_{12}$ thin film on a glass substrate.
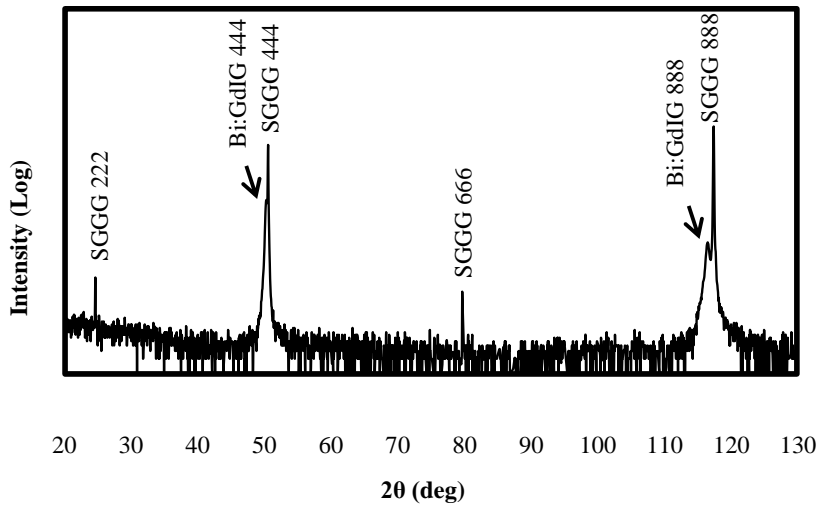
Fig. 6.5 X-ray diffraction spectra of the Bi$_2$Gd$_1$Fe$_5$O$_{12}$ thin film (J) on (111) SGGG substrate. Please note that the vertical axis logarithmic scale.

Fig. 6.5 shows the XRD spectra of the Bi$_2$Gd$_1$Fe$_5$O$_{12}$ film on an SGGG single crystal substrate. The diffraction peaks from (444) and (888) planes are clearly observed and other peaks associated with polycrystalline or impurity phases were not observed. The lattice constant d was calculated to 1.256 nm, which agreed with the reported lattice constant of Bi$_2$Gd$_1$Fe$_5$O$_{12}$ film [25].

Fig. 6.6 shows the optical transmittance spectra of Sample A-I on glass substrates and Sample J on an SGGG substrate. With increasing the Gd$_3$Fe$_5$O$_{12}$ buffer layer

thickness, the transparency became lower in the wavelength region below $\lambda < 600$ nm. Transparency was unchanged upon increasing the annealing temperature in $\lambda < 600$ nm.
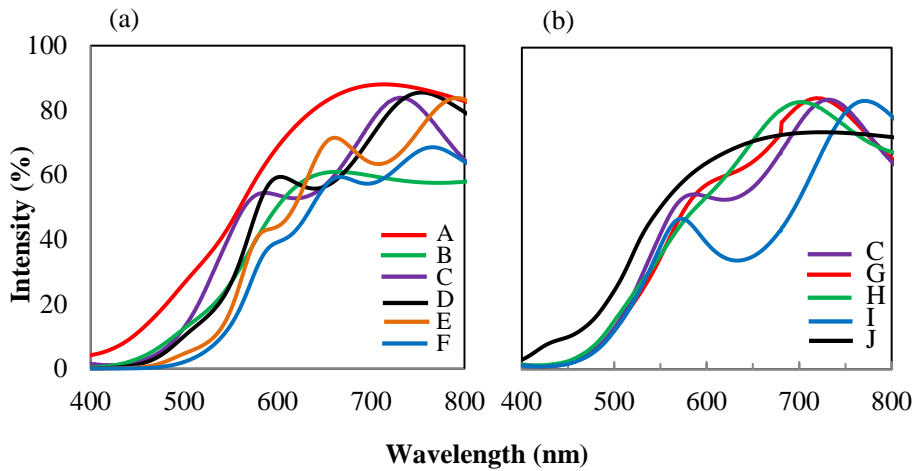
Fig. 6.6 Optical transmittance spectra of the $Bi_2Gd_1Fe_5O_{12}$ thin films with (a) different $Gd_3Fe_5O_{12}$ buffer layer thicknesses (A - F) and (b) different annealing temperature including Sample J on SGGG substrate.

Fig. 6.7 shows the FR spectra of all the $Bi_2Gd_1Fe_5O_{12}$ samples. Fig. 6.7 (c), and 6.7 (d) showed a summary of the maximum FR as a function of the spin-coating time for the $Gd_3Fe_5O_{12}$ buffer layer annealed at 650 °C, and annealing temperature of the $Gd_3Fe_5O_{12}$ buffer layer. From Figs. 6.7 (a) and 6.7 (c), I found that optimum spin-coating time giving the largest FR was 3 (C) and the maximum FR decreased when the spin-coating time is larger than 4. From Figs. 6.7 (b) and 6.7 (d), I found that maximum FR increased with increasing the annealing temperature of the $Gd_3Fe_5O_{12}$ buffer layer. The optimum annealing temperature giving maximum FR is 750 °C, and the maximum FR is 4.17 deg (36.3 deg./μm) at the wavelength $\lambda = 500$ nm, which is 23 times larger than that of FR of the sample without the $Gd_3Fe_5O_{12}$ buffer (Sample A), and 90.1 % of

the FR of single crystal $Bi_2Gd_1Fe_5O_{12}$ film on an SGGG substrate (4.23 deg. and 40.3 deg./µm for Sample J).

Let us discuss the reason why the FR of the $Bi_2Gd_1Fe_5O_{12}$ films was changed by the spin-coating time (thickness) for the $Gd_3Fe_5O_{12}$ buffer layer. As we can see from the XRD characterizations of Figs. 6.3 and 6.4, when the spin-coating time is 2, the $Gd_3Fe_5O_{12}$ layer is amorphous, and does not work as the buffer layer and the $Bi_2Gd_1Fe_5O_{12}$ layer was not crystallized, leading to little FR. I found that when the spin-coating time is larger than 4, the (420) plane of the $Gd_3Fe_5O_{12}$ phase is decreased and the Gd_2O_3 phase becomes more dominant, leading to lower FR. The diffracted intensity ratio of the (420) plane of the $Gd_3Fe_5O_{12}$ phase on the other oxide phases (especially Gd_2O_3) in the buffer layer is very important for obtaining large FR in the $Bi_2Gd_1Fe_5O_{12}$ film on glass substrates. With increasing the spin-coating time from 3 to 8, the ratio became smaller meaning that the amount of Gd_2O_3 phase increased when the buffer layer is too thick. Thick buffer layer reduces the optical transparency in the wavelength range showing maximum FR. Therefore, the optimum $Gd_3Fe_5O_{12}$ buffer layer thickness is 286 nm in this study for obtaining the $Bi_2Gd_1Fe_5O_{12}$ film on glass substrate giving the largest FR with minimum absorption.
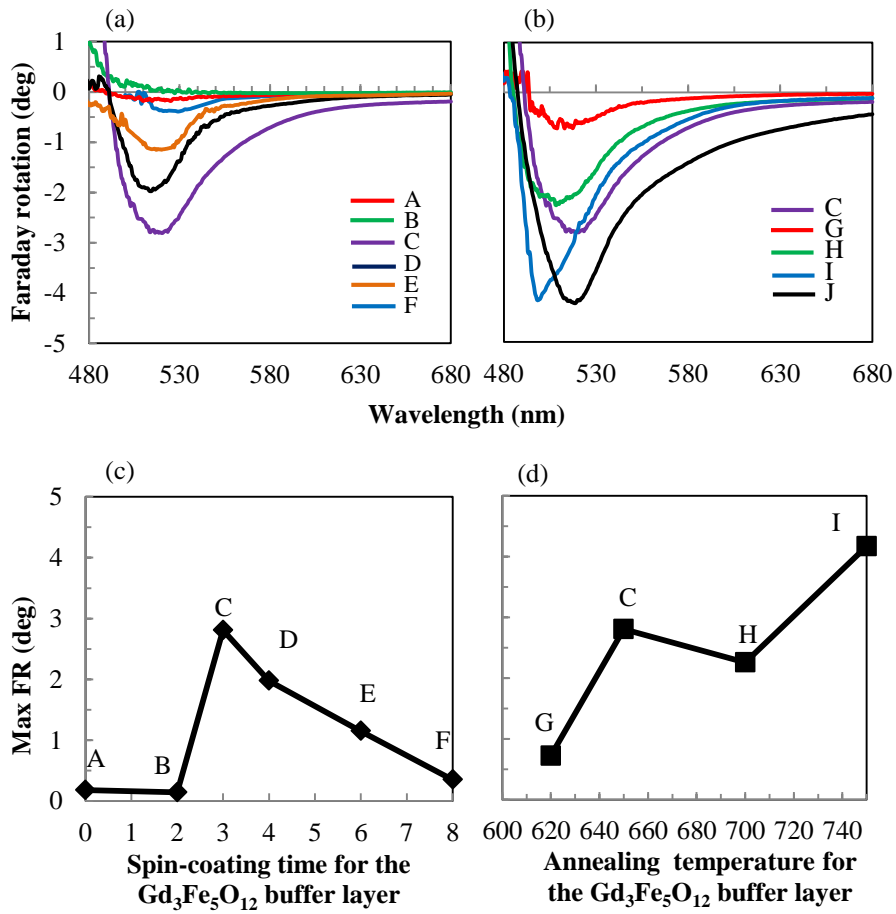
Fig. 6.7 Faraday rotation spectra of the $Bi_2Gd_1Fe_5O_{12}$ thin films with (a) different $Gd_3Fe_5O_{12}$ buffer layer thicknesses (A - F) and (b) different annealing temperature including Sample J on SGGG substrate. Magnetic field of 10 kG was applied perpendicular to the sample plane. Maximum FR of Samples A-F and C, G-I are summarized in (c) and (d).

I also found that the $Gd_3Fe_5O_{12}$ layer is not crystallized and does not work as buffer layer when the annealing temperature is 620 °C (G'), leading to smaller FR of the $Bi_2Gd_1Fe_5O_{12}$ layer (G) than the other samples (C, H, I) annealed at higher temperature. Sample I annealed at 750 °C showed the largest FR among the samples (C, G-I) whose annealing temperature for the $Gd_3Fe_5O_{12}$ buffer layer is changed. In Sample I, the diffraction signals from (420) plane of the $Bi_2Gd_1Fe_5O_{12}$ phase is the largest and the signals from α-Fe_2O_3 and β-Fe_2O_3 phase were not observed. The diffracted intensity from the Gd_2O_3 phase is the same between Sample I' and I, meaning that the diffracted signal from the Gd_2O_3 phase is from the $Gd_3Fe_5O_{12}$ buffer layer (not the $Bi_2Gd_1Fe_5O_{12}$ layer). On the other hand, diffracted signals from α-Fe_2O_3 and β-Fe_2O_3 phase were observed in Sample C, G, and H. α and β-Fe_2O_3 phases were suppressed by increasing the annealing temperature of the buffer layer. Also, growing of the Gd_2O_3 phase was suppressed in the $Bi_2Gd_1Fe_5O_{12}$ layer whose buffer layer is annealed at 750 °C (Sample I). Therefore, the optimum annealing temperature for the $Gd_3Fe_5O_{12}$ buffer layer is 750 °C for obtaining the $Bi_2Gd_1Fe_5O_{12}$ film on glass substrate giving the largest FR and best crystalline quality, as shown in FR data of Fig. 6.7.

Under the optimum preparation condition, I obtained the largest FR of 36.3 deg./μm at the wavelength λ = 500 nm. The obtained FR is 1.3 time larger than that of the $Bi_{2.5}Gd_{0.5}Fe_5O_{12}$ thin film (27.5 deg./μm), which I previously fabricated by the EMOD method in chapter 5 [22].

Fig. 6.8 shows the magnetic field dependence FR of $Bi_2Gd_1Fe_5O_{12}$ (samples A – H) and J at the wavelength λ = 525 nm, sample I at the wavelength of λ = 500 nm.
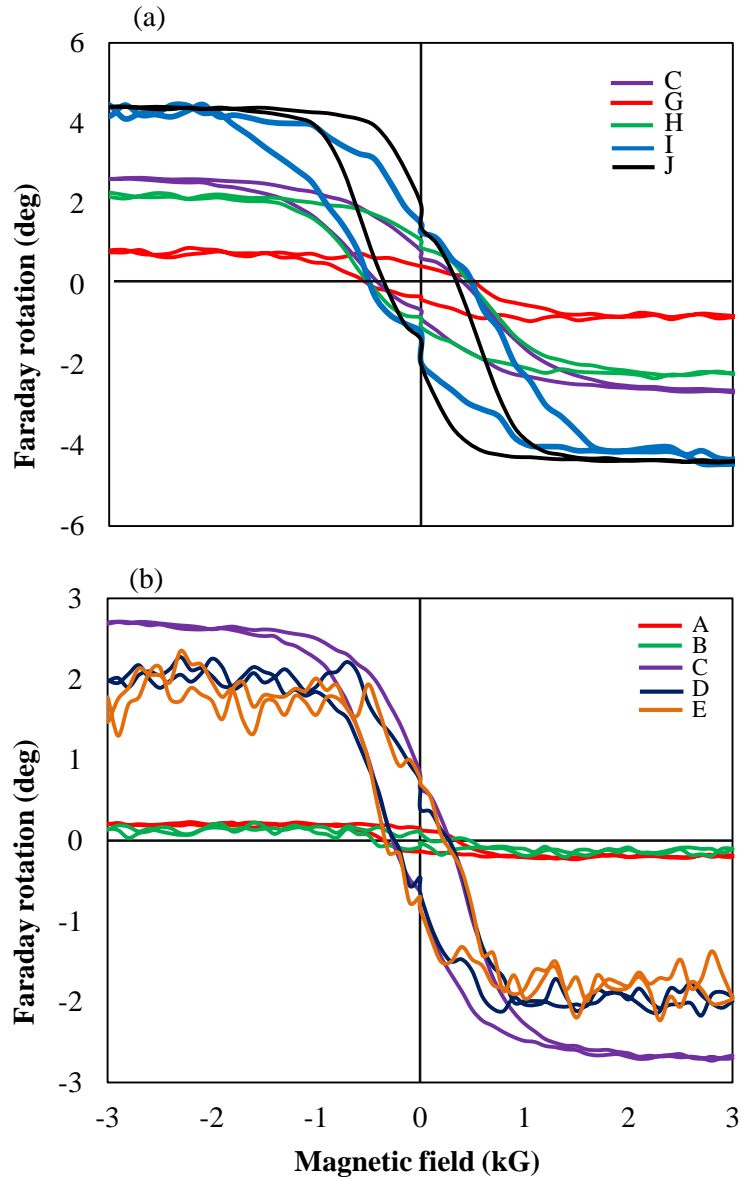
Fig. 6.8 Magnetic field dependence of the FR of the $Bi_2Gd_1Fe_5O_{12}$ thin films prepared on glass substrates using $Gd_3Fe_5O_{12}$ buffer layers.

Fig. 6.9 shows the images of samples $Bi_2Gd_1Fe_5O_{12}$ (A –I) taken by digital camera.

The surface of the samples is cleaner than the samples fabricated by EMOD method (chapter 5).

Fig. 6.10 shows the optical microscopic image of surface of the samples B – I.
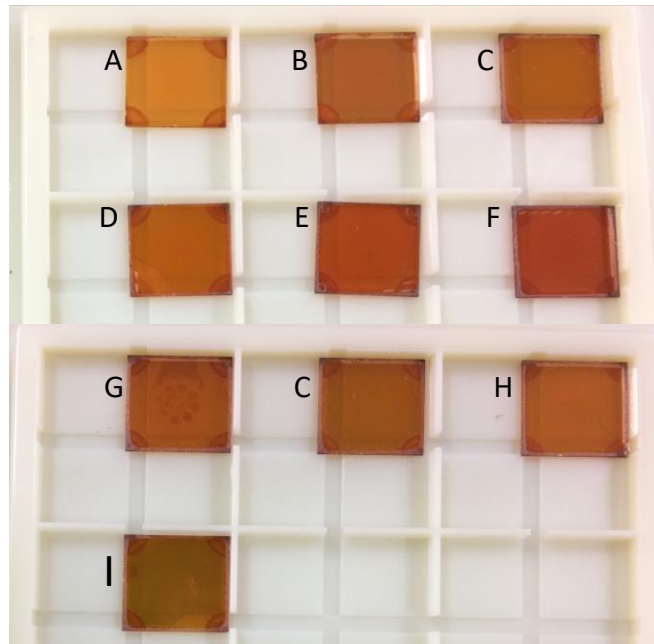
Fig. 6.9 The image of $Bi_2Gd_1Fe_5O_{12}$ thin films taken by digital camera using $Gd_3Fe_5O_{12}$ buffer layer samples A – I. The size of samples are 1.5 cm^2.
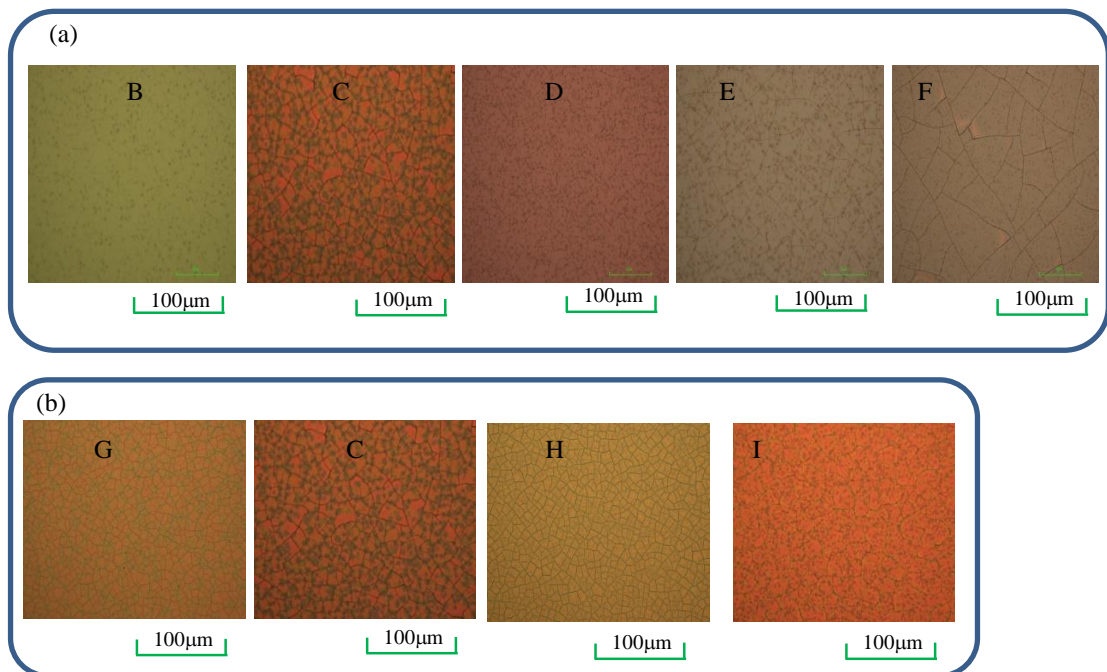
Fig. 6.10 Optical microscopic image of $Bi_2Gd_1Fe_5O_{12}$ thin films using $Gd_3Fe_5O_{12}$ buffer layer (a) samples B – F (spin-coating time in the range of 2, 3, 4, 6, and 8 at fixed T_{FA} of 650°C), (b) samples G – I (T_{FA} in the range of 620, 650, 700, 750° C with fixed spin-coating time of 3).

The main factor to determine the thickness and surface morphology of the Bi:GdIG thin films is the viscosities of the solutions. The viscosities of the solutions depend on their compositions in the MOD and EMOD methods. The thicknesses of samples per spin coating increased with increasing the amount of Bi in $Bi_xGd_{x-3}Fe_5O_{12}$ by EMOD method, because the viscosity of EMOD solution increased with increasing the amount of Bi content. On the other hand, the average thickness obtained by single spin-coating process was estimated to 84.4 nm for $Gd_3Fe_5O_{12}$ and 19.2 for $Bi_2Gd_1Fe_5O_{12}$ by MOD. This is because viscosity of the MOD solution decreased with increasing the amount of Bi content. The viscosity of MOD solution is 6.2 times larger than that of EMOD solution for $Gd_3Fe_5O_{12}$ and the viscosity of MOD and EMOD solution is almost similar for $Bi_2Gd_1Fe_5O_{12}$. The lower viscosity in a solution enables to control the thickness of the sample more precisely, and decompose the organic material properly for obtaining amorphous oxide films and cleaner surface morphology. With increasing the viscosity of the sample the surface morphology of the sample become worse.

Table 6.2 shows the summary of the estimated thicknesses per spin-coating and surface morphology of $Bi_xGd_{x-3}Fe_5O_{12}$ with $x = 0$, 1, 2, and 2.5 prepared by EMOD and MOD method on glass substrate.

Table 6.2 Comparison of thickness per spin-coating and surface morphology of $Bi_xGd_{3-x}Fe_5O_{12}$ thin films by EMOD and MOD method.

sample	Thickness /spin-coating (nm) and Surface morphology By EMOD		Thickness / spin-coating (nm) and Surface morphology By MOD	
$Gd_3Fe_5O_{12}$	13.64	slightly hazy	84.4	normal
$Bi_1Gd_2Fe_5O_{12}$	17.27	hazy	31.7	good
$Bi_2Gd_1Fe5O_{12}$	20.9	moor hazy	19.17	good
$Bi_{2.5}Gd_{0.5}Fe_5O_{12}$	31.36	very hazy		

6.4 Conclusions

I fabricated the $Bi_2Gd_1Fe_5O_{12}$ thin films with the $Gd_3Fe_5O_{12}$ buffer layer on glass substrates by the MOD method. Prior to the fabrication of the $Bi_2Gd_1Fe_5O_{12}$ thin films, I fabricated the single $Gd_3Fe_5O_{12}$ layers whose thicknesses were changed by the spin-coating times under various annealing temperatures. I measured the optical reflectivity spectra and estimated the thicknesses of the $Gd_3Fe_5O_{12}$ layers. I measured the X-ray diffraction of the samples, and clarified the relationship among the $Gd_3Fe_5O_{12}$ layer thickness, the crystalline orientation, and the amount of other oxide phases. Then I fabricated 115 nm-thick $Bi_2Gd_1Fe_5O_{12}$ thin films with the $Gd_3Fe_5O_{12}$ buffer layer whose thicknesses and annealing temperature were changed. I characterized the X-ray diffraction, and Faraday rotation spectra of the samples. The $Bi_2Gd_1Fe_5O_{12}$ thin films with 286 nm-thick $Gd_3Fe_5O_{12}$ buffer layer annealed at 750°C showed maximum Faraday rotation of 36.3 deg./μm at the wavelength $\lambda = 500$ nm. I investigated the influence of the preparation conditions of the buffer layer on the crystallization process, and discussed the relationship between the crystalline orientation of the $Gd_3Fe_5O_{12}$ / $Bi_2Gd_1Fe_5O_{12}$ layers and the Faraday rotation. Appearance of (420) plane of the $Bi_2Gd_1Fe_5O_{12}$ phase, and disappearance of the other oxides such as Gd_2O_3, α-Fe_2O_3 and β-Fe_2O_3 phases are the key for obtaining larger Faraday rotation. The largest Faraday rotation of 36.3 deg./μm is 23 times larger than the sample without the $Gd_3Fe_5O_{12}$ buffer layer, and as high as 90.1 % of the single crystalline $Bi_2Gd_1Fe_5O_{12}$ thin films on an SGGG substrate (40.3 deg./μm). These findings are promising for application to optical waveguide devices such as optical isolators and circulators, and MOSLMs on glass substrates.

CHAPTER 7

Conclusion

This thesis has presented a comprehensive investigation of the preparation and characterization of bismuth-substituted gadolinium iron garnet ($Bi_xGd_{3-x}Fe_5O_{12}$) thin films for application to various magneto optical devices such as waveguide optical isolators and circulators, and magneto optic spatial light modulators (MOSLMs).

Various fabrication processes and characterization have been discussed and compared. A comprehensive study has been conducted on overview of the theories and reported works related to the rare-earth iron garnets, particularly bismuth substituted iron garnet. There are many reports about fabrication methods and characterization of Bi substituted rare-earth iron garnet thin films.

In order to apply Bi substituted rare-earth iron garnet to magneto optical devices we need magnetic garnet thin film having perpendicular magnetic anisotropy and large Faraday rotation. Bi substituted gadolinium iron garnet is one of the materials to satisfy

these requirements. Also it is important to investigate the influence of the fabrication conditions on the magnetic anisotropy.

I fabricated bismuth substituted gadolinium iron garnet (Bi:GdIG) thin films on GGG, SGGG and glass substrates by MOD and EMOD method. Some of them were prepared on GdIG buffer layer glass substrate. I characterized the X-ray diffraction (XRD), Faraday effect, optical transmittance/reflectance and magnetization of the samples.

First I estimated the thicknesses of samples because MOD method is based on spin coating and annealing, so that the estimation of the thickness is important.

I explained the relationship among the magneto optical properties, crystallites of $Bi_xGd_{3-x}Fe_5O_{12}$ thin films and their thickness, annealing temperature, annealing gas (with and without O_2), and amount of Bi substitution (x).

Summary of the results achieved

It has been reported that the preparation of the Bi substituted rare-earth iron garnet thin films on single crystal gadolinium gallium garnet (GGG) is established because lattice matching between the fabricated garnet thin film and substrate made the fabrication easy. However there have been no reports about the influence of the O_2 gas on deficiency in $Bi_1Gd_2Fe_5O_{12}$ thin film in the annealing process and their magneto-optical property, and magnetic anisotropy by MOD method. I have prepared $Bi_1Gd_2Fe_5O_{12}$ thin films on GGG substrates by MOD method at different annealing temperature (620–800°C) and with different annealing gases (80% N_2+20% O_2 and 100% N_2 + 0% O_2) in order to investigate the influence on the magnetic anisotropy and

FR of the $Bi_1Gd_2Fe_5O_{12}$ thin films by changing annealing gas and annealing temperature.

1- The XRD, FR and magnetization measurements shows that Bi:GdIG thin films with large FR (13.68deg./μm) and high crystalline quality were successfully fabricated, and larger perpendicular magnetic anisotropy obtained for the samples annealed at $620 - 700°C$ with $100\%N_2 + 0\%O_2$ and for the samples annealed at $750 \sim 800$ °C with $100\%N_2 + 0\%O_2$, and $80\%N_2+20\%O_2$ annealing gas. The amount of the compressive strain and the dislocation defects at the interface between the Bi:GdIG film and GGG substrates are smaller for the samples annealed at higher temperature of $750 \sim 800$ °C with 20% O_2 and those annealed without O_2. Samples annealed without O_2 crystallized at lower temperature than those annealed with $20\%O_2$.

We could change the magnetic anisotropy by changing the annealing gas during the annealing process of the MOD method. This is our new findings.

Preparation of Bi:GdIG on GGG substrate is easy, however, the GGG substrate is more expensive than glass substrate. It has been known that preparation of Bi:GdIG thin films on glass substrates is not as easy as that on GGG substrates, because of the differences in crystal structure and thermal expansion coefficient between Bi:GdIG and glass substrate.

In order to fabricate $Bi_xGd_{3-x}Fe_5O_{12}$ thin films with various amount of Bi content x and obtain large FR on glass substrate, I used EMOD method instead of conventional MOD method, because the solutions of Gd_2O_3, Fe_2O_3, Bi_2O_3 can be prepared separately and mixed in any proportion of Gd_2O_3/Bi_2O_3 that offering wider choices in research.

The proportion of Gd_2O_3/Bi_2O_3 is fixed in MOD solution. I also used the $Gd_3Fe_5O_{12}$ buffer layer instead of direct fabrication on glass substrate.

2- The FR spectra shows that $x = 2$ and annealing temperature of 650 °C is the optimum condition for crystallization of $Bi_xGd_{3-x}Fe_5O_{12}$ thin films without $Gd_3Fe_5O_{12}$ buffer layer on the glass substrate.

3- The $Bi_{2.5}Gd_{0.5}Fe_5O_{12}$ samples with $Gd_3Fe_5O_{12}$ buffer layer on glass substrate successfully fabricated, and larger Faraday rotation (27.9 deg./µm at $\lambda = 533$ nm) was obtained. The Faraday rotation is 85% of single crystal $Bi_{2.5}Gd_{0.5}Fe_5O_{12}$ sample on single crystal (111) SGGG substrate.

4- However, the surface of the fabricated samples depends on the mixed EMOD solution. With increasing the Bi content, the surface of the sample becomes slightly hazy.

This result showed that using of $Gd_3Fe_5O_{12}$ buffer layer is useful to realize the $Bi_xGd_{3-x}Fe_5O_{12}$ thin films having large FR. Therefore I optimized the fabrication condition (crystallization temperature and thickness) for the $Gd_3F_5O_{12}$ buffer layer.

In order to realize the $Bi_xGd_{3-x}Fe_5O_{12}$ thin films having good surface morphology I applied the idea of buffer layer to MOD method.

I fabricated the $Gd_3Fe_5O_{12}$ layers whose thicknesses were changed by the spin-coating times under various annealing temperatures. Then I fabricated 115 nm-thick $Bi_2Gd_1Fe_5O_{12}$ thin films with fixed annealing temperature of 620 °C on the $Gd_3Fe_5O_{12}$ buffer layers.

5- The $Bi_2Gd_1Fe_5O_{12}$ thin films with 286 nm-thick $Gd_3Fe_5O_{12}$ buffer layer annealed at 750 °C showed maximum Faraday rotation of 36.3 deg./µm at the wavelength λ = 500 nm, which is 23 times larger than sample without the $Gd_3Fe_5O_{12}$ buffer layer, and as high as 90.1 % of the single crystalline $Bi_2Gd_1Fe_5O_{12}$ thin films on an SGGG substrate (40.3 deg./µm).

6- The surface of the samples was cleaner than those prepared by EMOD method.

Investigation of the influence of the GdIG buffer layer thickness and annealing temperature on the amount of the Faraday rotation of $Bi_xGd_{3-x}Fe_5O_{12}$ main layer is our new finding.

Thinner buffer layer is desired for magneto optical device applications, however, this is future task, for example thin buffer layer annealed at higher temperature or higher spin-coating speed.

These findings are promising for application to optical waveguide devices such as optical isolators and circulators, and MOSLMs on glass substrates.

Appendix:

Metal organic decomposition (MOD) method is a method for preparation of thin film on glass and other substrates. The procedure of the MOD process and its feature are discussed in detail in chapter 3. In this appendix I will discuss on difficulties of preparation of thin films by the MOD and EMOD method.

The viscosity of MOD solution is depending on composition of the solution, and the difference in viscosity lead to variety of thickness between different samples; therefore it is difficult to make different sample with same thickness. In some composition ($Gd_3Fe_5O_{12}$ and $Y_3Fe_5O_{12}$) the viscosity of the solutions are high, leading to following difficulties,

1- Difficult to control the thickness of the sample in small range (d < 10 nm thick film)

2- It is difficult to prepare a thin film with flat and homogeneous surface with sticky solution.

3- The thicker thickness per spin-coating makes it difficult to be decomposed, and to provide amorphous oxides during decomposition.

4- The most important problem of MOD is that some time we cannot have pure composition of the solution; making them difficult to prepare a thin film with desired composition.

The Fig. 2 (a) and (b) show the XRD spectra of $Gd_3Fe_5O_{12}$ thin film prepared by MOD method at annealing temperature of 700°C on glass substrate, using one type of MOD solution (Lot A, No. 3806151, Gd_2O_3:Fe_5O_3 = 3:5 in acetic ester) The Fig. 2 (a) shows the large phase of $Gd_3Fe_5O_{12}$ by MOD solution, Lot A . Fig. 2 (b) shows the smaller

phase of $Gd_3Fe_5O_{12}$ by MOD solution (Lot B, No. 4169041, $Gd_2O_3:Fe_5O_3$ = 3:5 in acetic ester) than that by Lot A. One of the possible reasons is that the composition of the MOD solutions are not the same between two $Gd_3Fe_5O_{12}$ MOD solutions (Lot A and B). Therefore it is necessary to test the film preparation with checking the appearance of the film and crystalline orientation especially first usage.
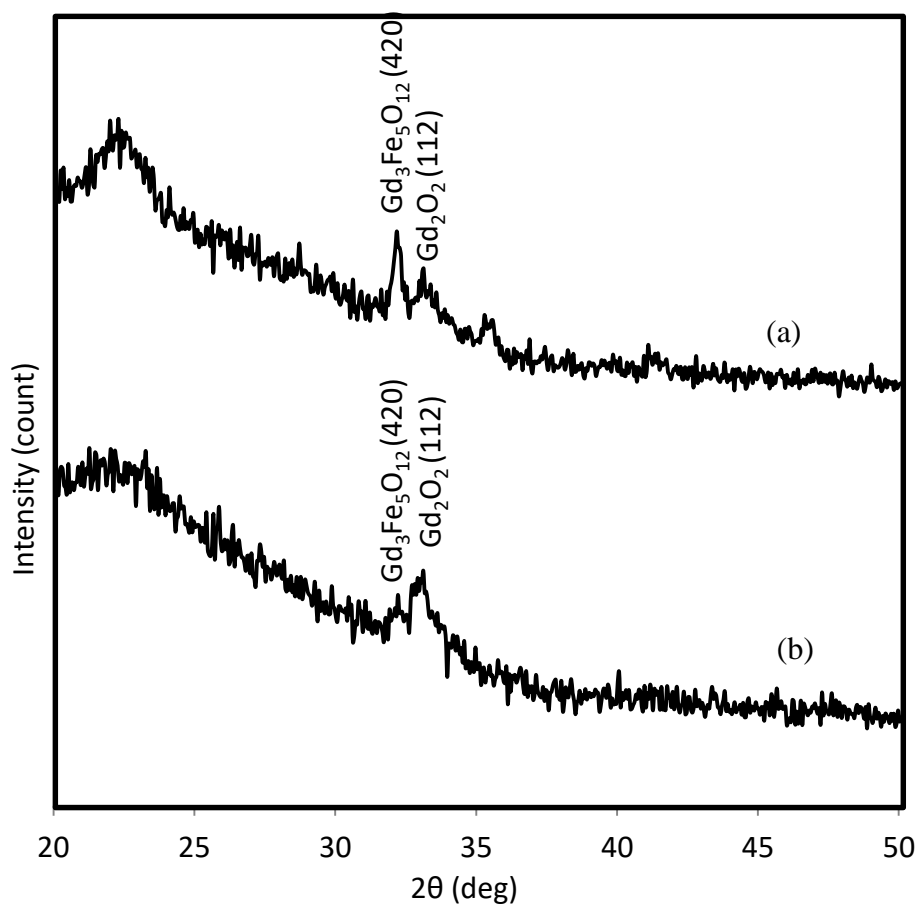
Fig. 2 XRD spectra of $Gd_3Fe_5O_{12}$ on glass substrate by MOD method, (a) Lot A (b) Lot B.

The MOD solution contains 2-3 types of metal oxides carboxylates such as Fe_2O_3, Bi_2O_3 and R_2O_3 (R = rare-earth metal) carboxylates in acetic ester to prepare

$Bi_xR_{3-x}Fe_5O_{12}$ thin films. The Bi content x is fixed and we cannot change the value of x to control the composition of the films.

The EMOD (Enhanced Metal Organic Decomposition) materials offered by Symetrix Corporation of America can be mixed and combined in a variety of different compounds. Since coating materials are solutions, coating materials containing different elements can be prepared and mixed in any proportion of choice.

The EMOD solution also depends on the combinations mixed. In some composition (Example: YIG), the viscosity was increased, which made it difficult to fabricate the YIG on glass substrate by EMOD method. The surface of the sample become milky and hazy, some smudge and precipitates were formed. Therefore the EMOD solution also depends on the combinations of mixed material. Some combinations are unsuitable for some applications.

Fig. 3 shows the picture of (a) YIG and (b) GdIG fabricated by EMOD method on glass substrate. The surface of the YIG sample is milky and the surface of GdIG sample is hazy.
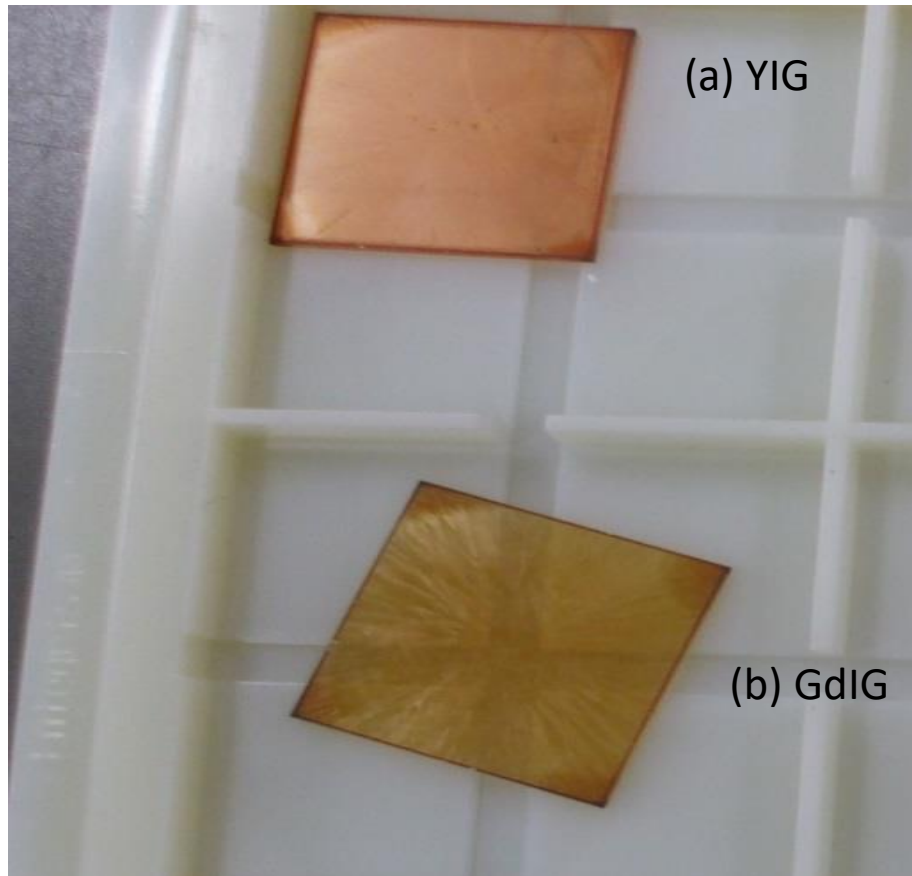
Fig. 3 Images of (a) YIG and (b) GdIG on glass substrate fabricated by EMOD method taken by digital camera.

List of journals publication

1. D. A. Wahid, T. Hattori, J. Sato, and H. Shimizu, "Preparation and characterization of Bi substituted gadolinium iron garnet films by metal organic decomposition and their dependence on annealing gases,": J. Magn. Soc. Jpn, **39** (2015) pp. 100-106. (DOI: 10.3379/msjmag.1504R007).

2. D. A. Wahid, J. Sato, M. Hosoda, and H. Shimizu, "Preparation and characterization of Bi substituted gadolinium iron garnet $Bi_xGd_{3-x}Fe_5O_{12}$ films with x=1 to 2.5 by Enhanced Metal Organic Decomposition method,": J. Magn. Soc. Jpn, **40** (2016) pp. 107-114. (DOI: 10.3379/msjmag. 1605R007).

3. D. A. Wahid, T. Morioka, and H. Shimizu, "Preparation of $Bi_2Gd_1Fe_5O_{12}$ magnetic garnet films showing Faraday rotation of 36.3 deg./mm on glass substrates by metal organic decomposition method," IEICE. Electronics Express, **13** (2016) Page 20161011 (1-12). (DOI: 10.1587/elex.13.20161011)

International conferences

1. D. A. Wahid, T. Hattori, J. Sato, and H. Shimizu, "Magneto-optic effect and magnetic anisotropy of Bi:YIG thin films prepared by metal organic decomposition method," Magnetics and optics research international symposium (MORIS 2013), Omiya sonic city, Saitama, Japan, December 3 (2013), We-P-03.

2. D. A. Wahid, J. Sato, M. Hosoda and H. Shimizu, "Preparation and Characterization of Bi substituted gadolinium iron garnet with high Bi substitution on glass substrates by Enhanced Metal Organic Decomposition

method," The 18th International conference on crystal growth and epitaxy ICCGE-18, Nagoya, Japan, August 11 (2016), ThP-T05-2.

Domestic Conferences

1. D. A. Wahid, T. Hattori, J. Sato, and H. Shimizu, "Preparation of $Bi_2YFe_5O_{12}$ and $Bi_1Gd_2Fe_5O_{12}$ magnetic garnet thin films by Metal Organic Decomposition method on GGG and glass substrate," Digests of the 38th annual conference on magnetics in Japan 2014, Keio University, Kanagawa, Japan, September 4 (2014), 4pE-2.

2. D. A. Wahid, J. Sato, M. Hosoda and H. Shimizu, "Preparation and Characterization of Bi substituted gadolinium iron garnet $Bi_xGd_{3-x}Fe_5O_{12}$ films with x = 1 to 2.5 by Enhanced Metal Organic Decomposition method," The 63rd JSAP Spring Meeting, 2016, Tokyo Inst. Of Tech. Ookayama Campus Japan, March 21 (2016), 21p-P16-5.

3. D. A. Wahid, T. Morioka, and H. Shimizu, "Preparation and Characterization of Bi substituted gadolinium iron garnet (Bi:GdIG) on glass substrates by MOD method with GdIG buffer layer," The 77th JSAP Autumn Meeting, 2016, Toki Messe Niigata Japan, September 13 (2016), 13p-P8-16.

References

Chapter-1

[1] "Magneto-Optic spatial light modulators with magnetophotonic crystals driven by PZT films", H. Takagi, J. Kim, K. H. Chung, S. Mito, H. Umezawa, and M. Inoue, J. Magn. Soc. Jpn, 33, 525 (2009).

[2] "Magnetophotonic crystal with cerium substituted yttrium iron garnet and enhanced Faraday rotation angle" T. Yoshimoto, T. Goto, R. Isogai, Y. Nakamura, H. Takagi, A. Ross, and M. Inoue, Opt Express, 24, 8746 (2016).

[3] "Improvement of diffraction efficiency of three-dimensional magneto-optic spatial light modulator with magnetophotonic crystal" K. Nakamura, H. Takagi, T. Goto, P. B. Lim, H. Horimai, H. Yoshikawa, M. Bove and M. Inoue, Appl. Phys. Lett, 108, 022404-1 (2016).

[4] "Temperature dependence of the Faraday rotation of lead and bismuth substituted gadolinium iron garnet films at 633 nm", P. Hansen, H. Heitrnann, and K. Witter, Phys. Rev. B, 23, 6085, (1981).

[5] "The effects of the sputtering conditions on bismuth doped gadolinium iron garnet films", W. Eppler and M. H. Kryder, IEEEE. T. Magn, 25, 3743, (1989).

[6] "Magneto-optical spectra of bismuth-substituted gadolinium iron garnets in vacuum ultraviolet", M. Suzuki, T. Kotani, N. Yamaguchi, T. Miura, M. Yamaoka, M. Kobayashi, and A. Misu, J. Electron. Spectrosc, 78, 291, (1996).

[7] "Gaint Faraday rotation in $Bi_xCe_{3-x}Fe_5O_{12}$ epitaxial garnet films", M. Chandra Sekhar, Mahi R. Singh, Shantanu Basu and S. Pinnepalli, Opt. Express, 20, 9624, (2012).

[8] "The Faraday effect of Bismuth Substituted Rare-earth iron garnet", H. Takeuchi, Jpn. J. Appl. Phys,. 14, 1903, (1975).

[9] "Magnetic moments in a gadolinium iron garnet studied by soft-X-ray magnetic circular dichroism", P. Rudolf, F. Sette 1, L.H. Tjeng, G. Meigs and C.T. Chen, J. Magn. Magn. Mater., 109, 109, (1992).

[10] "Mechanochemical decomposition of $Gd_3Fe_5O_{12}$ garnet phase", R. Justin Joseyphus, A. Narayanasamy, N. Sivakumar, M. Guyot, R. Krishnan, N. Ponpandian, K. Chattopadhyay, J. Magn. Magn. Mater, 272, 2257, (2004).

[11] "Mueller matrix optical and magneto-optical characterization of Bi-substituted gadolinium iron garnet for application in magnetoplasmonic structures", L. Halagacka, K. Postava, M. Vanwolleghem, F. Vaurette, J. Ben Youssef, B. Dagens, and J. Piˇstora, J. Opt. Soc. Am. A, 4, 1903, (2014).

[12] "Optical isolators using Bi-substituted rare-earth iron garnet films", H. Ishikawa, K. Nakajima, K. Machida and A. Tanii, Opt Quantum Electron., 22, 517, (1990).

[13] "Compact optical circulator based on a uniformly magnetized ring cavity", W. Smigaj, L. Magdenko, L. Magdenko, J. Romero, S. Guenneau, B. Dagens, B. Gralak and M. Vanwolleghem, Phot. Nano. Fund. Appl, 10, 83, (2012).

[14] "Magneto-optical circulator designed for operation in a uniform external magnetic field", W. Smigaj, J. Romero, B. Gralak, L. Magdenk, B. Dagens and M. Vanwolleghem: Opt. Lett, 35, 568 (2010).

[15] "Characteristics of magneo-photonic crystals based magneto-optic SLMs for spatial light phase modulators", K. H. Chung, J. Heo, K. Takahashi, S. Mito, H. Takagi, J. Kim, P.B.Lim and M.Inoue, J. Magn. Soc. Jpn, 32, 114 (2008).

[16] "Behavior of Large Faraday Rotation in Magnetophotonic Crystals with Single-Cavity Structures", H. Kato, T. Matsushita, A. Takayama, M. Egawa, H. Uchida, K. Nishimaura, M. Inoue, Trans. Magn. Soc. Jpn, 4, 289, (2004).

[17] "Study on magnetic garnet films for voltage driven magneto optic spatial light phase modulators with one dimensional magneto photonic crystal", S. Mito, K. Takahashi, F. Kawanishi, K. H. Chung, H. Takagi, J. Kim, P. B. Lim, and M. Inoue, J. Magn. Soc. Jpn., 32, 63, (2008).

[18] "Deposition of Garnet Thin Films by Metallo-organic Decomposition (MOD)", A. Azevedo, S. Bharthulwar, W. R. Eppler and M. H. Kryder, IEEE Transactions on Magnetics, 30, 4416, (1994)

[19] "MZI optical isolator with Si-wire waveguides by surface- activated direct bonding," Y. Shoji, M. Ito, Y. Shirato, and T. Mizumoto, Opt. Express 20, 18440 (2012).

[20] "Preparation of $Y_{0.5}Bi_{2.5}Fe_5O_{12}$ films on glass substrates using magnetic iron garnet buffer layers by metal-organic decomposition method," T. Ishibashi, T. Yoshida, T, Kobayashi, S. Ikehara, and T. Nishi, J. Appl. Phys 113, 926, (2013).

[21] "The Faraday effect of Bismuth Substituted Rare-earth iron garnet", H. Takeuchi, Jpn. J. Appl. Phys, 14, 1903, (1975).

Chapter-2

[1] Second edition, University of Tokyo, OXFORD SCIENCE PUBLICATIONS international series of monographs, SONSHIN CHIKAZUMI, Emeritus, "PHYSICS OF FERROMAGNETISM", on physics. 94, 1997.

[2] "Wideband magneto-optic modulation in a bismuth-substituted yttrium iron garnet waveguide", S. E. Irvine and A. Y. Elezzabi, Opt Commun, 220, 325, (2003).

[3] "Optical isolators using Bi substituted rare earth iron garnet films", H. Ishikawa, K. Nakajima, K. Machida, A. Tani, Opt. Quant. Electron, 22, 517, (1990).

[4] "Pulsed laser deposited $Y_3Fe_5O_{12}$ films: nature of magnetic anisotropy II", S. A. Manuilov and A. M. Grishin, J. Appl Phys, 108, 013902, (2010).

[5] "Compact optical circulator based on a uniformly magnetized ring cavity", W. Smigaj, L. Magdenko, J. R. Vivas, S. Guenneau, B. Dagens, B. Gralak, M. Vanwolleghem, Photonics and Nanostructures – Fundamentals and Applications, 10, 83, (2012).

[6] "Magneto-optical circulator designed for operation in a uniform external magnetic field", W. migaj, J. Romero, B. Dagens, and M. Vanwolleghem,Vivas, B. Gralak, L. Magdenko, Opt. Lett, 35, 568, (2010).

[7] "Growth and ferromagnetic resonance of yttrium iron garnet thin films on metals", Y. Y. Sun, Y.-Y. Song, and M. Wu, Applied Physics Letters, 101, 082405, (2012).

[8] K. Enke et al: LANDOLT-BORNSTEIN, vol. 12 "Magnetic and Other Properties of Oxides and Related Compounds Part a Garnets and Perovskites", Springer-Verlag Berlin, New York, (1978).

[9] http://www.uiowa.edu/~c004132/ATOMIC_ORBITALS.html

[10] "Growth by rf sputtering and characterization of magnetic garnet films", R. Marcelli, P. De Gasperis, M. C. Martucci et al., J. Magn. Magn. Mater, <u>104</u>, 436, (1992).

[11] "Pulsed laser deposition of high-quality μm thick YIG films on YAG", A. Sposito, T. C.May-Smith, G. B. G. Stenning, P. A. J. de Groot, and R. W. Eason, Opt. Mater. Exp, <u>3</u>, 624, (2013).

[12] "Magnetic properties of gadolinium oxides", K. P. BELOV, M. A. ZAITSEVA, and A. V. PED'KO, J. Exptl. Theoret. Phys. (U.S.S.R.) <u>36</u>, 1672-1679 (1959).

[13] "Ferrimagnetic resonance effects and miscellaneous in magnetic garnet", G. P Rodrigue, H. Meyer and R. V. Jones, J. Appl. Phys, <u>31</u>, 376S (1960).

[14] "Susceptibility of Gadolinium Iron Garnet below the Neel Point", W. P. WOI and R. M. BOZORTH, Phys. Rev, <u>124</u>, 449 (1961).

[15] "The Faraday effect of bismuth substituted rare-earth iron garnet", H. Takeuchi, Jpn. J. Appl. Phys, <u>14</u>, 1903, (1975).

[16] "Temperature dependence of the Faraday rotation of lead and bismuth substituted gadolinium iron garnet films at 633 nm", P. Hansen, H. Heitrnann, and K. witter, Phys. Rev. B, <u>23</u>, 6085, (1981).

[17] "Magneto-optical properties of cerium substituted yttrium iron garnet films with reduced thermal budget for monolithic photonic integrated circuits", Taichi Goto, Mehmet C. Onbaşl, and C. A. Ross, Optics Express, <u>27</u>, 28507, (2012).

[18] "Deposition of Garnet thin Films by metallo-organic decomposition MOD", A. Axevedo, S. Bharthulwar, WlR. Eppler and M. H. Kryder, IEEE. Trans on Magn, <u>30</u>, 4416, (1994).

[19] "Magnetic and magneto optic properties of lead and bismuth substituted yttrium iron garnet films", P. Hansen, K. Witter, and W. Tolksdorf, Phys. Rev. B, 27, 6608, (1983).

[20] "Magnetic and magneto optical properties of bismuth substituted gadolinium iron garnet films", P. Hansen, K. Witter, and W. Tolksdorf, Phys. Rev. B, 27, 4375, (1983).

[21] "Faraday rotation spectra of bismuth-substituted ferrite garnet films with in-plane magnetization", L. E. Helseth, R. W. Hansen, E. I. Il'yashenko, M. Baziljevich, and T. H. Johansen, PHYSICAL REVIEW B, 64, 174406, (2001)

[22] "Spectral origins of giant Faraday rotation and ellipticity in Bi-substituted magnetic garnets", Geraid F. Dionne, J. Appl. Phys, 73, 6127, (1993).

[23] "The effects of the sputtering conditions on bismuth doped gadolinium iron garnet films", W. eppler and M. H. Kryder, IEEEE. T. Magn, 25, 3743, (1989).

[24] "Magneto-optical spectra of bismuth-substituted gadolinium iron garnets in vacuum ultraviolet", M. Suzuki, T. Kotani, N. Yamaguchi, T. Miura, M. Yamaoka, M. Kobayashi, and A. Misu, J. Electron. Spectrosc, 78, 291, (1996).

[25] "Theoretical investigation of the impact of substituting bismuth ion in yttrium iron garnet on the Faraday rotation", H. Ahmad, N. Mohammad and Z. Sirus, J. World. Appl. Sci, 19, 424, (2012).

[26] "Magneto-optic spectra and the dielectric tensor elements of bismuth-substituted iron garnets at photon energies between 2.2—5.2 eV, Wittekoek", T. J. A. Poprna, J. M. Robertson, and P. F. Bongers, Phys. Rev. B, 12, 2777, (1975).

[27] "Theoretical Consideration of Faraday rotation Spectra of Bismuth Substituted Yttrium Iron Garnet Films", Koji Matsumoto, Satoshi Sasaki, Ken'ichi Haraga,

Kazuhiro Yamaguchi and Toshitaka, Fuji, IEEE TRANSACTIONS ON MAGNETICS, <u>28</u>, 2985, (1992).

[28] "Magneto-optical Properties of Bi-substituted Yttrium Iron Garnet Films by Metal-organic Decomposition Method", T. Ishibashi, T. Kosaka, M. Naganuma and T. Nomura, J. Phys: conference Series 200 (2010).

Chapter-3

[1] "Laser ablation of Bi-substituted gadolinium iron garnet films", N. Watanabe , K. Hayashida, K. Kawano, K. Higuchi, M. Ohkoshi, K. Tsushima, J. Magn. Magn. Mater, <u>140</u>**,** 2131. (1995).

[2] "Characteristics of Bi:YIG Magneto-Optic Thin Films Fabricated by Pulsed Laser Deposition Method for an Optical Current Transformer", Hiromitsu Hayashi, Souhachi Iwasa, Nilesh J. Vasa, Tsuyoshi Yoshitake, Kiyotaka Ueda, Shigeru Yokoyama and Sadao Higuchi, J. Appl. Phys, <u>41</u>, 410, (2002).

[3] "The effects of substrate temperature and oxygen pressure on pulsed laser deposited Bi-substituted Dy iron garnet films", P. Papakonstantinou, B. Teggart, R. Atkinson, J. Magn. Magn. Mater, <u>163</u>, 378, (1996).

[4] "Liquid phase epitaxy (LPE) grown Bi, Ga, Al substituted iron garnets with huge Faraday rotation for magneto-optic applications", P. Görnert, T. Aichele, A. Lorenz, R. Hergt, and J. Taubert, Phys. Stat. sol, <u>201</u>, 1398, (2004).

[5] "Preparation and Optical Properties of Single Crystal Thin Films of Bismuth Substituted Iron Garnets for Magneto-Optic Applications", J. M. Robertson, S. Wittekoek, Th. J. A. Popma, and P. F. Bongers, Appl. Phys. <u>2</u>, 219, (1973).

[6] "Effects of oxygen vacancies on the magnetic and electrical properties of Ca-substituted yttrium iron garnet", Y.J. Song, G.B. Turpin, R.E. Bomfreund, H. Aoyama, P.E. Wigen, J. Magn. Magn. Mater. <u>154</u>, 37, (1996).

[7] "Epitaxial Growth and Properties of Bi-Substituted Yttrium-Iron-Garnet Films Grown on (111) Gadolinium-Gallium-Garnet Substrates by Using rf Magnetron Sputtering", Y. H. Kim, J. S. Kim and S. I. Kim, Journal of the Korean Physical Society, <u>43</u>, 400, (2003).

[8] "Highly bismuth-substituted, record-performance magneto-optic garnet materials with low coercivity for applications in integrated optics, photonic crystals, imaging and sensing", M. Nur-E-Alam, M.Vasiliev, Viacheslav A. Kotov, and Kamal Alameh, Optical materials express, <u>1</u>, 413, (2011).

[9] "Magneto-optical properties of a sputtered Bi-substituted Dy iron garnet-ferrite/spinel-ferrite bilayer", A. Furuya, H. Yoshikawa, T. Ohkubo, M. Yamamoto, P. Tailhades, L. Bouet, C. Despax, L. Presmanes, A. Rousset, J. Magn. Magn. Mater, <u>193</u>, 143, (1999).

[10] "Preparation and magneto-optic properties of Bi-substituted yttrium iron garnet thin films by metalorganic chemical vapor deposition", Masaru Okada, Shigehisa Katayama and Koji Tominaga, J. Appl. Phys. <u>69</u>, 3566, (1991).

[11] "Structural and magneto-optical properties of Bi substituted garnet films prepared by pyrolysis from organic solution", J. Cho, M. Gomi, M. Abe, Jpn. J. Appl. Phys. <u>28</u>, 1593, (1989).

[12] "Crystal ion slicing of single-crystal magnetic garnet films", M. Levy, R. M. Osgood, Jr. A. Kumar and H. Bakhru, J. Appl. Phys. <u>83</u>, 6759, (1998).

[13] "Preparation and magnetic properties of $Y_3Fe_5O_{12}$ nanoparticles doped with the gadolinium oxide", Zhongjun Chenga, Hua Yanga, Lianxiang Yua, Yuming Cuia, Shouhua Fengb, J. Magn. Magn. Mater, <u>302</u>, 259, (2006).

[14] "Deposition of Garnet Thin Films by Metallo-organic Decomposition MOD", A. Azevedo, S. Bharthulwar, W. R. Eppler and M. H. Kryder, IEEE T. MAGN, <u>30</u>, 4416, (1994).

[15] "Magneto-optical visualization by Bi:YIG thin films prepared at low temperatures", Ogsen Galstyan, Hanju Lee, Arsen Babajanyan, Arsen Hakhoumian, Barry Friedman, and Kiejin Lee, J. Appl. Phys, <u>117</u>, 163914, (2015).

[16] "(Re,Bi)$_3$(Fe,Ga)$_5$O$_{12}$ (Re¼Y, Gd and Nd) thin films grown by MOD method", T. Ishibashi, A. Mizusawa, N. Togashi, T. Mogi, M. Houchido, K. Sato, J. Cryst. Growth, <u>275</u>, 2427, (2005).

[17] "Magneto-optical Properties of Bi-substituted Yttrium Iron Garnet Films by Metal-organic Decomposition Method", Takayuki Ishibashi, Terumasa Kosaka, Masayuki Naganuma and Tatsuo Nomura, International Conference on Magnetism (ICM 2009), Journal of Physics: Conference Series <u>200</u> (2010) 112002.

[18] "Epitaxial growth of narrow linewidth yttrium iron garnet films", R.C. Linares, J. Cryst. Growth, <u>3</u>, 443, (1968).

[19] "Growth of Bi and Ga Substituted YIG and LuIG Layers by LPE Method", B. Keszei, Z. Vértesy, G. Vértesy, Cryst. Res. Technol, <u>36</u>, 953, (2001).

[20] "Springer handbook of electronic and photonic materials", Safa. Kasap, Peter. Capper, p.1406, (2006).

[21] "Bismuth iron garnet films for magneto-optical photonic crystals", Soren Kahl, Doctoral Dissertation, Condensed Matter Physics, Laboratory of Solid State Devices, IMIT, Royal Institute of Technology, Stockholm (2004).

[22] "Optical and magnetooptical properties of bismuth and gallium substituted iron garnet films", F. Hansteen, L. E. Helseth, T. H. Johansen, O. Hunderi, A. Kirilyuk, and T.Rasing, Thin Solid Films, 455, 429, (2004).

[23] "Growth and characterization of liquid phase epitaxial Bi substituted iron garnet films for magneto optical application", T. Hibiya, Y. Morishige and J. Nakashima, Jpn. J. Appl. Phys, 24, 1316, (1985).

[24] http://www.andor.com/learning-academy

[25] "Pulsed laser ablation deposition of yttrium iron garnet and cerium-substituted YIG films", N. B. Ibrahim, C. Edwards and S. B. Palmer, J. Magn. Magn. Mater, 220, 184, (2000).

[26] "RF-sputter fabrication of magnetic garnet thin films and simulation modeling for 1-D magnetic photonic crystal waveguide devices", Haichun Yang, DISSERTATION Submitted in partial fulfillment of the requirement for the degree of DOCTOR OF PHILOSOPHY, Material Science and Engineering, MICHIGAN TECHNOLOGICAL UNIVERSITY, (2005).

[27] "The effects of the sputtering conditions on bismuth doped gadolinium iron garnet films", W. Eppler and M. H. Kryder, IEEE. T. Magn, 25, 3743, (1989).

[28] http://www.kojundo.co.jp

[29] "Preparation and characterization of $Bi_3Fe_5O_{12}$ thin films grown on glass substrate", S. Ikehara, K. Wada, T. Kobayashi, S. Goto, T. Yoshida, T. Ishibashi, and T. Nishi: J. Magn. Soc. Jpn, 36, 169, (2012).

[30] "MZI optical isolator with Si-wire waveguides by surface-activated direct bonding", Y. Shoji, M. Ito, Y. Shirato, and T. Mizumoto, Opt. Express, 20, 18440, (2012).

[31] "On-chip optical isolation in monolithically integrated non-reciprocal optical resonators", L. Bi, J. Hu, P. Jiang, D. H. Kim, G. F. Dionne, L. C. Kimerling, and C. A. Ross, Nat. Photonics, 5, 758, (2011).

[32] "Vacuum annealed cerium-substituted yttrium iron garnet films on non-garnet substrates for integrated optical circuits", T. Goto, Y. Eto, K. Kobayashi, Y. Haga, M. Inoue, and C. A. Ross, J. Appl. Phys, 113, 17A939, (2013).

[33] "Magneto optic spatial light modulators with magnetophotonic crystals driven by PZT films", H. Takagi, J. Kim, K. H. Chung, S. Mito, H. Umezawa, and M. Inoue, J. Magn. Soc. Jpn, **33**, 525, (2009).

[34] "The theoretical investigation of the impact of substituting bismuth ion in yttrium iron garnet (YIG) on the Faraday rotation" H. Ahmad, N. Mohammad, Z, Sirus, World. Appl. Sci. J., 19, 424, (2012)

[35] Modern magnetooptics and magnetooptical materials, A.K. Zvezdin and A.V. Kotov, (1997)

[36] "Magneto-optic spectra and the dielectric tensor elements of bismuth-substituted iron garnets at photon energies between 2.2—5.2 eV," S. Wittekoek, T. J. A. Poprna, J. M. Robertson, and P. F. Bongers, Phys. Rev. B, **12**, 2777, (1975).

[37] "Measurement of Magneto optical Kerr Effect using piezo birefringent modulator", Katsuaki Sato, Jpn. J. Appl. Phys., 20, 2403, (1981).

[38] http://www.jascoint.co.jp/asia/products/spectroscopy/uv/v670.

[39] "A method for determining thickness and optical constants of absorbing thin films", David Pekker, and Leonid Pekker, Thin. Solic Films, 425, 203, (2003).

[40] "Comprehensive formulations for the total normal-incidence optical reflectance and transmittance of thin films laid on thick substrates", Mousa M. Abdul-Gader Jafar, EUR. Int. J. Science & Tech, 2, 214, (2013).

[41] "Optical constants of silica glass from extreme ultraviolet to far infrared at near room temperature", R. Kitamur, L. Pilon, and M. Jonasz, Appl. Optics, 46, 8118, (2007).

[42] "Magnetization measurement by alternating gradient field magnetometer (AGFM)", Zijlstra, H., Rev. Sci. Instrum., 41, 1241, (1970).

Chapter 4

 [1] "Preparation and characterization of Bi substituted gadolinium iron garnet films by metal organic decomposition and their dependence on annealing gases", D. A. Wahid, T. Hattori, J. Sato, and H. Shimizu, J. Magn. Soc. Jpn., 39, 100, (2015).

[2] R. H. Hammond, and R. Bormann, Physica C 162- 164, 703, (2002).

[3] "Defects and the Electronic Properties of $Y_3Fe_5O_{12}$", P. K. Larsen and R. Metselaar, J. Solid. State. Chemistry, 12, 253, (1975).

[4] "Voltage-Assisted Magnetization Switching in Ultrathin $Fe_{80}Co_{20}$ Alloy Layers", Y. Shioda, T. Maruyama, T. Nozaki, T. Shinjo, M. Shiraishi, and Y. Suzuki, Appl. Phys. Express, 2, 063001, (2009).

[5] "Magnetic and other properties of oxides and related compounds", K. Enke et al: LANDOLT-BORNSTEIN, 12, Springer-Verlag Berlin, (1978).

Chapter 5

 [1] "Temperature dependence of the Faraday rotation of lead- and bismuth-substituted gadolinium iron garnet films at 633 nm", P. Hansen, H. Heitmann, and K. Witter: Phys. Rev. B. <u>23</u> (1981).

 [2] "MZI optical isolator with Si-wire waveguides by surface-activated direct bonding", Y. Shoji, M. Ito, Y. Shirato, and T. Mizumoto: Opt. Express, <u>20</u>, 18440, (2012).

[3] "On-chip optical isolation in monolithically integrated non-reciprocal optical resonators" L. Bi, J. Hu, P. Jiang, D. H. Kim, G. F. Dionne, L. C. Kimerling, and C. A. Ross: Nat. Photonics, <u>5,</u> 758, (2011).

[4] "Vacuum annealed cerium-substituted yttrium iron garnet films on non-garnet substrates for integrated optical circuits", T. Goto, Y. Eto, K. Kobayashi, Y. Haga, M. Inoue, and C. A. Ross: J. Appl. Phys, <u>113,</u> 17A939, (2013).

[5] "A nonreciprocal racetrack resonator based on vacuum-annealed magnetooptical cerium-substituted yttrium iron garnet", T. Goto, M. C. Onbasli, D. H. Kim, V. Singh, M. Inoue, L. C. Kimerling, and C. A. Ross: Opt. Express, <u>22</u>, 19047, (2014).

[6] "Magneto-optical spectra of bismuth-substituted gadolinium iron garnets in vacuum ultraviolet", M. Suzuki, T. Kotani, N. Yamaguchi, T. Miura, M. Yamaoka, M. Kobayashi, and A. Misu, J. Electron. Spectrosc, <u>78</u>, 291, (1996).

[7] "Optical and magneto-optical properties of bismuth and gallium substituted iron garnet films", Fredrik Hansteena, Lars Egil Helseth, Tom. H. Johansen, Ola Hunderi, Andrei. Kirilyuk, T. Rasing, Thin. Solid. Film., <u>455</u>, 429, (2004).

[8] "Epitaxial Growth and Properties of Bi-Substituted Yttrium-Iron-Garnet Films Grown on (111) Gadolinium-Gallium-Garnet Substrates by Using rf Magnetron Sputtering", Y. H. Kim, J. S. Kim and S. I. Kim, Journal of the Korean Physical Society, 43, 400, (2003).

[9] "Deposition of Garnet Thin Films by Metallo-organic Decomposition MOD", A. Azevedo, S. Bharthulwar, W. R. Eppler and M. H. Kryder, IEEE T. MAGN, 30, 4416, (1994).

[10] "The effects of the sputtering conditions on bismuth doped gadolinium iron garnet films", W. Eppler and M. H. Kryder, IEEEE. T. Magn, 25, 3743, (1989).

[11] "Preparation and characterization of $Bi_3Fe_5O_{12}$ thin films grown on glass substrate", S. Ikehara, K. Wada, T. Kobayashi, S. Goto, T. Yoshida, T. Ishibashi, and T. Nishi, J. Magn. Soc. Jpn, 36, 169, (2012).

[12] "Preparation of $Y_{0.5}Bi_{2.5}Fe_5O_{12}$ films on glass substrates using magnetic iron garnet buffer layers by metal-organic decomposition method", T. Ishibashi, T. Yoshida, S. Ikehara and T. Nishi, J. Appl. Phys., 113, 17A926, (2013).

[13] http://www.kojundo.co.jp/English/Guide/material/csd.html

[14] "A method for determining thickness and optical constants of absorbing thin films, David Pekker, Leonid Pekker", Thin. Solic Films, 425, 203, (2003).

[15] "Comprehensive formulations for the total normal-incidence optical reflectance and transmittance of thin films laid on thick substrates", Mousa M. Abdul-Gader Jafar, EUR. Int. J. Science & Tech, 2, 214, (2013).

[16] "Optical constants of silica glass from extreme ultraviolet to far infrared at near room temperature", R. Kitamur, L. Pilon, and M. Jonasz, Appl. Optics, 46, 8118, (2007).

[17] "M. Hosoda, J. Sato, D. A. Wahid, H. Shimizu: Proc. the 63rd. spring meeting of Japan Society of Applied Physics", 20a-S621-2, Tokyo, (2016).

[18] "Magnetic and magneto optical properties of bismuth substituted gadolinium iron garnet films", P. Hansen, K. Witter, and W. Tolksdorf, Phys. Rev. B, 27, 4375, (1983).

[19] International Center for Diffraction Data (ICDD), www.icdd.com

Chapter 6

[1] "Temperature dependence of the Faraday rotation of lead- and bismuth-substituted gadolinium iron garnet films at 633 nm", P. Hansen, H. Heitmann, and K. Witter: Phys. Rev. B. 23 (1981).

[2] "MZI optical isolator with Si-wire waveguides by surface-activated direct bonding", Y. Shoji, M. Ito, Y. Shirato, and T. Mizumoto: Opt. Express, 20, 18440, (2012).

[3] "On-chip optical isolation in monolithically integrated non-reciprocal optical resonators" L. Bi, J. Hu, P. Jiang, D. H. Kim, G. F. Dionne, L. C. Kimerling, and C. A. Ross: Nat. Photonics, 5, 758, (2011).

[4] "Vacuum annealed cerium-substituted yttrium iron garnet films on non-garnet substrates for integrated optical circuits", T. Goto, Y. Eto, K. Kobayashi, Y. Haga, M. Inoue, and C. A. Ross: J. Appl. Phys, 113, 17A939, (2013).

[5] "A nonreciprocal racetrack resonator based on vacuum-annealed magnetooptical cerium-substituted yttrium iron garnet", T. Goto, M. C. Onbasli, D. H. Kim, V. Singh, M. Inoue, L. C. Kimerling, and C. A. Ross: Opt. Express, 22, 19047, (2014).

[6] "Preparation and Characterization of Bi substituted gadolinium iron garnet Films by Metal Organic Decomposition and their Dependence on Annealing Gases", D. A. Wahid, T. Hattori, J. Sato, and H. Shimizu: J. Magn. Soc. Jpn. 39, 100, (2015).

[7] "Preparation and characterization of Bi substituted gadolinium iron garnet $Bi_xGd_{3-x}Fe_5O_{12}$ films with x=1 to 2.5 by Enhanced Metal Organic Decomposition method", D. A Wahid, J. Sato, M. Hosoda, and H. Shimizu: J. Magn. Soc. Jpn, 40, 107, (2016).

[8] "A method for determining thickness and optical constants of absorbing thin films", D. Pekker, and L. Pekker: Thin Solid Films. <u>425</u>, 203, (2003).

[9] M. M. A-G. Jafar: Euro. Intl. J. Sci. Technol, <u>2,</u> 214, (2013). (www.cekinfo.org.uk/EIJST).

[10] "Magnetic and magneto-optical properties of bismuth-substituted gadolinium iron garnet films", P. Hansen, K. Witter, and W. Tolksdorf: Phys. Rev B., <u>27</u>, 4375, (1983).